

Measurement of the Inclusive ep Scattering Cross Section at Low Q^2 and x at HERA

H1 Collaboration

Abstract

A measurement of the inclusive ep scattering cross section is presented in the region of low momentum transfers, $0.2 \text{ GeV}^2 \leq Q^2 \leq 12 \text{ GeV}^2$, and low Bjorken x , $5 \cdot 10^{-6} \lesssim x \lesssim 0.02$. The result is based on two data sets collected in dedicated runs by the H1 Collaboration at HERA at beam energies of 27.6 GeV and 920 GeV for positrons and protons, respectively. A combination with data previously published by H1 leads to a cross section measurement of a few percent accuracy. A kinematic reconstruction method exploiting radiative ep events extends the measurement to lower Q^2 and larger x . The data are compared with theoretical models which apply to the transition region from photoproduction to deep inelastic scattering.

Accepted by EPJ C

F.D. Aaron^{5,49}, C. Alexa⁵, V. Andreev²⁵, B. Antunovic¹¹, S. Aplin¹¹, A. Asmone³³,
A. Astvatsatourov⁴, S. Backovic³⁰, A. Baghdasaryan³⁸, E. Barrelet²⁹, W. Bartel¹¹,
K. Begzsuren³⁵, O. Behnke¹⁴, O. Behrendt⁸, A. Belousov²⁵, J.C. Bizot²⁷, V. Boudry²⁸,
I. Bozovic-Jelisavcic², J. Bracinik³, G. Brandt¹¹, M. Brinkmann¹¹, V. Brisson²⁷, D. Bruncko¹⁶,
A. Bunyatyan^{13,38}, G. Buschhorn²⁶, L. Bystritskaya²⁴, A.J. Campbell¹¹, K.B. Cantun Avila²²,
F. Cassol-Brunner²¹, K. Cerny³², V. Cerny^{16,47}, V. Chekelian²⁶, A. Cholewa¹¹, J.G. Contreras²²,
J.A. Coughlan⁶, G. Cozzika¹⁰, J. Cvach³¹, J.B. Dainton¹⁸, K. Daum^{37,43}, M. Deák¹¹,
Y. de Boer¹¹, B. Delcourt²⁷, M. Del Degan⁴⁰, J. Delvax⁴, A. De Roeck^{11,45}, E.A. De Wolf⁴,
C. Diaconu²¹, V. Dodonov¹³, A. Dossanov²⁶, A. Dubak^{30,46}, G. Eckerlin¹¹, D. Eckstein³⁹,
V. Efremenko²⁴, S. Egli³⁶, A. Eliseev²⁵, E. Elsen¹¹, A. Falkiewicz⁷, P.J.W. Faulkner³,
L. Favart⁴, A. Fedotov²⁴, R. Felst¹¹, J. Feltesse^{10,48}, J. Ferencei¹⁶, D.-J. Fischer¹¹,
M. Fleischer¹¹, A. Fomenko²⁵, E. Gabathuler¹⁸, J. Gayler¹¹, S. Ghazaryan³⁸, A. Glazov¹¹,
I. Glushkov³⁹, L. Goerlich⁷, N. Gogitidze²⁵, M. Gouzevitch²⁸, C. Grab⁴⁰, T. Greenshaw¹⁸,
B.R. Grell¹¹, G. Grindhammer²⁶, S. Habib^{12,50}, D. Haidt¹¹, M. Hansson²⁰, C. Helebrant¹¹,
R.C.W. Henderson¹⁷, E. Hennekemper¹⁵, H. Henschel³⁹, M. Herbst¹⁵, G. Herrera²³,
M. Hildebrandt³⁶, K.H. Hiller³⁹, D. Hoffmann²¹, R. Horisberger³⁶, T. Hreus^{4,44}, M. Jacquet²⁷,
M.E. Janssen¹¹, X. Janssen⁴, V. Jemanov¹², L. Jönsson²⁰, A.W. Jung¹⁵, H. Jung¹¹,
M. Kapichine⁹, J. Katzy¹¹, I.R. Kenyon³, C. Kiesling²⁶, M. Klein¹⁸, C. Kleinwort¹¹, T. Kluge¹⁸,
A. Knutsson¹¹, R. Kogler²⁶, V. Korbel¹¹, P. Kostka³⁹, M. Kraemer¹¹, K. Krastev¹¹,
J. Kretzschmar¹⁸, A. Kropivnitskaya²⁴, K. Krüger¹⁵, K. Kutak¹¹, M.P.J. Landon¹⁹, W. Lange³⁹,
G. Laštovička-Medin³⁰, P. Laycock¹⁸, T. Laštovička³⁹, A. Lebedev²⁵, G. Leibenguth⁴⁰,
V. Lendermann¹⁵, S. Levonian¹¹, G. Li²⁷, K. Lipka¹², A. Liptaj²⁶, B. List¹², J. List¹¹,
E. Lobodzinska³⁹, N. Loktionova²⁵, R. Lopez-Fernandez²³, V. Lubimov²⁴, L. Lytkin¹³,
A. Makankine⁹, E. Malinovski²⁵, P. Marage⁴, Ll. Martí¹¹, H.-U. Martyn¹, S.J. Maxfield¹⁸,
A. Mehta¹⁸, K. Meier¹⁵, A.B. Meyer¹¹, H. Meyer¹¹, H. Meyer³⁷, J. Meyer¹¹, V. Michels¹¹,
S. Mikocki⁷, I. Milcewicz-Mika⁷, F. Moreau²⁸, A. Morozov⁹, J.V. Morris⁶, M.U. Mozer⁴,
M. Mudrinic², K. Müller⁴¹, P. Murín^{16,44}, B. Naroska^{12,†}, Th. Naumann³⁹, P.R. Newman³,
C. Niebuhr¹¹, A. Nikiforov¹¹, G. Nowak⁷, K. Nowak⁴¹, M. Nozicka¹¹, B. Olivier²⁶,
J.E. Olsson¹¹, S. Osman²⁰, D. Ozerov²⁴, V. Palichik⁹, I. Panagoulas^{1,11,42}, M. Pandurovic²,
Th. Papadopoulou^{1,11,42}, C. Pascaud²⁷, G.D. Patel¹⁸, O. Pejchal³², E. Perez^{10,45}, A. Petrukhin²⁴,
I. Picuric³⁰, S. Piec³⁹, D. Pitzl¹¹, R. Plačákytė¹¹, R. Polifka³², B. Povh¹³, T. Preda⁵,
V. Radescu¹¹, A.J. Rahmat¹⁸, N. Raicevic³⁰, A. Raspiareza²⁶, T. Ravdandorj³⁵, P. Reimer³¹,
E. Rizvi¹⁹, P. Robmann⁴¹, B. Roland⁴, R. Roosen⁴, A. Rostovtsev²⁴, M. Rotaru⁵,
J.E. Ruiz Tabasco²², Z. Rurikova¹¹, S. Rusakov²⁵, D. Šálek³², D.P.C. Sankey⁶, M. Sauter⁴⁰,
E. Sauvan²¹, S. Schmitt¹¹, C. Schmitz⁴¹, L. Schoeffel¹⁰, A. Schöning^{11,41},
H.-C. Schultz-Coulon¹⁵, F. Sefkow¹¹, R.N. Shaw-West³, I. Sheviakov²⁵, L.N. Shtarkov²⁵,
S. Shushkevich²⁶, T. Sloan¹⁷, I. Smiljanic², Y. Soloviev²⁵, P. Sopicki⁷, D. South⁸, V. Spaskov⁹,
A. Specka²⁸, Z. Staykova¹¹, M. Steder¹¹, B. Stella³³, G. Stoicea⁵, U. Straumann⁴¹, D. Sunar⁴,
T. Sykora⁴, V. Tchoulakov⁹, G. Thompson¹⁹, P.D. Thompson³, T. Toll¹¹, F. Tomasz¹⁶,
T.H. Tran²⁷, D. Traynor¹⁹, T.N. Trinh²¹, P. Truöl⁴¹, I. Tsakov³⁴, B. Tseepeldorj^{35,51}, J. Turnau⁷,
K. Urban¹⁵, A. Valkárová³², C. Vallée²¹, P. Van Mechelen⁴, A. Vargas Trevino¹¹, Y. Vazdik²⁵,
S. Vinokurova¹¹, V. Volchinski³⁸, M. von den Driesch¹¹, D. Wegener⁸, Ch. Wissing¹¹,
E. Wunsch¹¹, J. Žáček³², J. Zálešák³¹, Z. Zhang²⁷, A. Zhokin²⁴, T. Zimmermann⁴⁰,
H. Zohrabyan³⁸, and F. Zomer²⁷

¹ *I. Physikalisches Institut der RWTH, Aachen, Germany^a*

² *Vinca Institute of Nuclear Sciences, Belgrade, Serbia*

- ³ *School of Physics and Astronomy, University of Birmingham, Birmingham, UK^b*
- ⁴ *Inter-University Institute for High Energies ULB-VUB, Brussels; Universiteit Antwerpen, Antwerpen; Belgium^c*
- ⁵ *National Institute for Physics and Nuclear Engineering (NIPNE) , Bucharest, Romania*
- ⁶ *Rutherford Appleton Laboratory, Chilton, Didcot, UK^b*
- ⁷ *Institute for Nuclear Physics, Cracow, Poland^d*
- ⁸ *Institut für Physik, TU Dortmund, Dortmund, Germany^a*
- ⁹ *Joint Institute for Nuclear Research, Dubna, Russia*
- ¹⁰ *CEA, DSM/Irfu, CE-Saclay, Gif-sur-Yvette, France*
- ¹¹ *DESY, Hamburg, Germany*
- ¹² *Institut für Experimentalphysik, Universität Hamburg, Hamburg, Germany^a*
- ¹³ *Max-Planck-Institut für Kernphysik, Heidelberg, Germany*
- ¹⁴ *Physikalisches Institut, Universität Heidelberg, Heidelberg, Germany^a*
- ¹⁵ *Kirchhoff-Institut für Physik, Universität Heidelberg, Heidelberg, Germany^a*
- ¹⁶ *Institute of Experimental Physics, Slovak Academy of Sciences, Košice, Slovak Republic^f*
- ¹⁷ *Department of Physics, University of Lancaster, Lancaster, UK^b*
- ¹⁸ *Department of Physics, University of Liverpool, Liverpool, UK^b*
- ¹⁹ *Queen Mary and Westfield College, London, UK^b*
- ²⁰ *Physics Department, University of Lund, Lund, Sweden^g*
- ²¹ *CPPM, CNRS/IN2P3 - Univ. Mediterranee, Marseille - France*
- ²² *Departamento de Fisica Aplicada, CINVESTAV, Mérida, Yucatán, México^j*
- ²³ *Departamento de Fisica, CINVESTAV, México^j*
- ²⁴ *Institute for Theoretical and Experimental Physics, Moscow, Russia^k*
- ²⁵ *Lebedev Physical Institute, Moscow, Russia^e*
- ²⁶ *Max-Planck-Institut für Physik, München, Germany*
- ²⁷ *LAL, Univ Paris-Sud, CNRS/IN2P3, Orsay, France*
- ²⁸ *LLR, Ecole Polytechnique, IN2P3-CNRS, Palaiseau, France*
- ²⁹ *LPNHE, Universités Paris VI and VII, IN2P3-CNRS, Paris, France*
- ³⁰ *Faculty of Science, University of Montenegro, Podgorica, Montenegro^e*
- ³¹ *Institute of Physics, Academy of Sciences of the Czech Republic, Praha, Czech Republic^h*
- ³² *Faculty of Mathematics and Physics, Charles University, Praha, Czech Republic^h*
- ³³ *Dipartimento di Fisica Università di Roma Tre and INFN Roma 3, Roma, Italy*
- ³⁴ *Institute for Nuclear Research and Nuclear Energy, Sofia, Bulgaria^e*
- ³⁵ *Institute of Physics and Technology of the Mongolian Academy of Sciences , Ulaanbaatar, Mongolia*
- ³⁶ *Paul Scherrer Institut, Villigen, Switzerland*
- ³⁷ *Fachbereich C, Universität Wuppertal, Wuppertal, Germany*
- ³⁸ *Yerevan Physics Institute, Yerevan, Armenia*
- ³⁹ *DESY, Zeuthen, Germany*
- ⁴⁰ *Institut für Teilchenphysik, ETH, Zürich, Switzerlandⁱ*
- ⁴¹ *Physik-Institut der Universität Zürich, Zürich, Switzerlandⁱ*
- ⁴² *Also at Physics Department, National Technical University, Zografou Campus, GR-15773 Athens, Greece*
- ⁴³ *Also at Rechenzentrum, Universität Wuppertal, Wuppertal, Germany*
- ⁴⁴ *Also at University of P.J. Šafárik, Košice, Slovak Republic*
- ⁴⁵ *Also at CERN, Geneva, Switzerland*

⁴⁶ Also at Max-Planck-Institut für Physik, München, Germany

⁴⁷ Also at Comenius University, Bratislava, Slovak Republic

⁴⁸ Also at DESY and University Hamburg, Helmholtz Humboldt Research Award

⁴⁹ Also at Faculty of Physics, University of Bucharest, Bucharest, Romania

⁵⁰ Supported by a scholarship of the World Laboratory Björn Wiik Research Project

⁵¹ Also at Ulaanbaatar University, Ulaanbaatar, Mongolia

[†] Deceased

^a Supported by the Bundesministerium für Bildung und Forschung, FRG, under contract numbers 05 H1 1GUA /1, 05 H1 1PAA /1, 05 H1 1PAB /9, 05 H1 1PEA /6, 05 H1 1VHA /7 and 05 H1 1VHB /5

^b Supported by the UK Science and Technology Facilities Council, and formerly by the UK Particle Physics and Astronomy Research Council

^c Supported by FNRS-FWO-Vlaanderen, IISN-IKW and IWT and by Interuniversity Attraction Poles Programme, Belgian Science Policy

^d Partially Supported by Polish Ministry of Science and Higher Education, grant PBS/DESY/70/2006

^e Supported by the Deutsche Forschungsgemeinschaft

^f Supported by VEGA SR grant no. 2/7062/ 27

^g Supported by the Swedish Natural Science Research Council

^h Supported by the Ministry of Education of the Czech Republic under the projects LC527, INGO-IP05LA259 and MSM0021620859

ⁱ Supported by the Swiss National Science Foundation

^j Supported by CONACYT, México, grant 48778-F

^k Russian Foundation for Basic Research (RFBR), grant no 1329.2008.2

^l Project co-funded by the European Social Fund (75%) and National Resources (25%) - (EPEAEK II) - PYTHAGORAS II

1 Introduction

Deep inelastic lepton-hadron scattering (DIS) is pivotal for the understanding of the structure of the nucleon and of the dynamics of parton interactions. Since the discovery of Bjorken scaling [1] and its violation [2] at fixed target experiments, DIS measurements have made essential contributions to in the development of the theory of strong interactions, Quantum Chromodynamics (QCD). Major progress in the exploration of strong interactions has been achieved at the electron¹-proton collider HERA, operating at the energy frontier. Measurements performed at HERA are essential for predictions of the physics at the forthcoming proton-proton collider, the Large Hadron Collider (LHC).

The high centre-of-mass energy of the ep scattering at HERA leads to a wide kinematic range extending to large values of the modulus of the four-momentum transfer squared, denoted Q^2 , and to very small values of the Bjorken x variable. At the HERA beam energies of $E_e = 27.6$ GeV for the electron and $E_p = 920$ GeV for the proton, Bjorken x values as small as 10^{-4} (10^{-6}) are accessible for Q^2 of 10 GeV^2 (0.1 GeV^2).

A salient feature of the structure function $F_2(x, Q^2)$, discovered by the H1 [3] and ZEUS [4] collaborations with the very first HERA data, is its strong rise for $x \rightarrow 0$. In terms of parton distribution functions, this can be directly interpreted as a strong rise of the sea quark density towards small x . Similarly the increase of $F_2(x, Q^2)$ with Q^2 at fixed small x reveals a strongly rising behaviour of the gluon density towards low x . This is obtained in perturbative QCD (pQCD) analyses of DIS data [5–8] using the derivative $\partial F_2 / \partial \ln Q^2$, which is related to the gluon and quark densities as prescribed by the DGLAP evolution equations [9–13].

The DGLAP approach, in which only $\alpha_s \ln Q^2$ terms are summed, may not apply at lowest x values as terms involving powers of $\alpha_s \ln(1/x)$ become large. The parton dynamics at low x may be better approximated by different evolution equations, such as BFKL [14–16], CCFM [17–20] or non-linear equations [21–28]. The non-linear effects, arising due to the large gluon density and corresponding for example to gluon-gluon recombination, could tame the rise of F_2 at low x . Further clarification of low x parton dynamics requires data of the highest precision, in a wide range of x and Q^2 .

For $Q^2 \lesssim 2 \text{ GeV}^2$, as the strong coupling constant $\alpha_s(Q^2)$ increases, the higher order corrections to the perturbative expansion become large and lead to the breakdown of the pQCD calculations. Measurements at low Q^2 and low x thus probe this transition in which quarks and gluons cease to be relevant degrees of freedom. This onset of soft hadron physics is described by phenomenological, often QCD-inspired models (see [29] for a review).

An attractive view of virtual photon-proton scattering has been developed with the colour dipole model [30]. It originated from the observation that in the proton rest frame, at low x the photon may fluctuate into a quark-antiquark pair with a lifetime $\propto 1/x$, long before the interaction with the proton [31,32]. Therefore the cross sections can be expressed as a product of the square of the wavefunction of the $q\bar{q}$ pair with a universal dipol-proton cross section. Another phenomenological model, used here, describes $F_2(x, Q^2)$ based on the idea of self-similarity of the proton substructure at small x [33].

¹Unless explicitly stated, the generic name “electron” is used throughout this paper to denote both electron and positron.

Access to the smallest x implies an extension of the measurements to high values of the inelasticity y where the cross section becomes sensitive to the longitudinal structure function $F_L(x, Q^2)$. This function completes the description of inclusive virtual photon-proton scattering, which involves transverse and longitudinal photon polarisation states. In the naive quark-parton model (QPM), F_L is zero, while in QCD it provides independent information [34] on the gluon distribution and may become correspondingly large at low x .

This paper presents new measurements of the inclusive ep cross section in the range $0.2 \leq Q^2 \leq 12 \text{ GeV}^2$ and $5 \cdot 10^{-6} \leq x \leq 0.02$. The data were collected with the H1 detector in two e^+p running periods with dedicated settings of the inclusive electron triggers. One data set (termed nominal vertex, “NVX”) was collected in the year 1999 and corresponds to an integrated luminosity of 2.1 pb^{-1} . The other was collected in the year 2000, with the interaction region shifted along the proton beam direction by 70 cm (termed shifted vertex, “SVX”), and corresponds to 505 nb^{-1} .

Shifting the interaction region allows detection of the scattered electron at larger polar angles² which otherwise cannot be accessed in the main H1 apparatus and thus provides acceptance in the region $Q^2 \lesssim 2 \text{ GeV}^2$. In comparison to the previous H1 measurement with a shifted vertex [35], an increased precision is reached using the higher luminosity of the new data and employing, in addition to the previous backward instrumentation of the H1 detector, an upgraded Backward Silicon Tracker (BST). The vertex reconstruction using the electron track in the BST allows the kinematic range to be extended at low Q^2 and low y .

The measurement region is further extended towards lower Q^2 and higher x values by exploiting events with hard photons emitted collinearly to the electron beam (Initial State Radiation or ISR). Such events are treated as ep events at an effectively reduced centre-of-mass energy. Unlike in the previous H1 ISR analysis [36], the emitted photons are not explicitly detected, but the missing momentum is determined using momentum conservation. For this method the BST charged particle validation of the scattered electron is important to reduce the physics background from photoproduction events, in which the scattered electron escapes undetected in the electron beam direction.

The measurement presented here is combined with previously published data [35,37] taken at $E_p = 820 \text{ GeV}$ in the region $Q^2 \geq 1.5 \text{ GeV}^2$ (NVX97) and in the region $Q^2 \geq 0.35 \text{ GeV}^2$ employing a shifted vertex technique (SVX95). The data sets are combined taking into account their systematic error correlations. The resulting accuracy reaches two percent precision in the bulk region of the measurement providing the most precise measurement in this kinematic domain.

Data on F_2 extending to low Q^2 were published by the ZEUS Collaboration using a detector mounted near the beam pipe [38]. For $Q^2 \gtrsim 2 \text{ GeV}^2$, ZEUS data [39] from the 820 GeV operation of HERA are also available.

The paper is organised as follows: In section 2 basic definitions are given. In section 3 models are introduced which are subsequently compared to the data. In section 4 the methods to determine the DIS event kinematics and the principle of the cross section measurement are

²In the H1 coordinate system the z axis points along the outgoing proton beam direction termed forward direction. Therefore large electron polar angles θ_e close to 180° correspond to very small angles with respect to the incoming electron direction. The coordinate system is right-handed. The x (y) axis is directed horizontally (vertically).

presented. In section 5 the H1 apparatus is described with emphasis on the components of key importance for the present measurement. Section 6 presents the event selection and reconstruction, followed by section 7 on the Monte Carlo (MC) simulation of events. In section 8 a detailed account of the analysis techniques and uncertainties of the measurement is given, and the cross sections obtained from the 1999 and 2000 data are presented. In section 9 the data averaging method and the combination of the new data with the previous H1 data taken at $E_p = 820$ GeV are presented. Section 10 is devoted to a phenomenological analysis of the x dependence of F_2 and to extractions of the longitudinal structure function F_L and in section 11 the data are compared to phenomenological models. A summary is given in section 12.

2 Definitions

In the low Q^2 kinematic range of the present measurement, contributions from Z boson exchange to neutral current deep inelastic scattering can be neglected. In the one-photon exchange approximation, the double differential cross section for neutral current DIS is given, in its reduced form σ_r , by

$$\sigma_r = \frac{Q^4 x}{2\pi\alpha^2[1 + (1 - y)^2]} \cdot \frac{d^2\sigma}{dx dQ^2} = F_2(x, Q^2) - f(y) \cdot F_L(x, Q^2) \quad (1)$$

with the fine structure constant denoted α and $f(y) = y^2/[1 + (1 - y)^2]$. The inelasticity y is related to Q^2 , x and the centre-of-mass energy squared, $s = 4E_e E_p$, by $y = Q^2/sx$. In the quark-parton model (QPM), x denotes the fraction of the proton momentum carried by the parton coupling to the exchanged boson.

The DIS cross section, equation 1, is determined by two structure functions, F_2 and F_L . These are related to the cross sections for the scattering of longitudinally and transversely polarised photons off protons, σ_L and σ_T . At low x , the relationships

$$F_L = \frac{Q^2}{4\pi^2\alpha}(1 - x) \cdot \sigma_L, \quad (2)$$

$$F_2 = \frac{Q^2}{4\pi^2\alpha}(1 - x) \cdot (\sigma_L + \sigma_T), \quad (3)$$

hold to very good approximation. Positivity of the longitudinal and transverse scattering cross sections imposes the restriction $0 \leq F_L \leq F_2$. Using the ratio $R(x, Q^2)$

$$R = \frac{\sigma_L}{\sigma_T} = \frac{F_L}{F_2 - F_L}, \quad (4)$$

the reduced cross section in equation 1 can be written as

$$\sigma_r = F_2(x, Q^2) \cdot \left[1 - f(y) \cdot \frac{R}{1 + R} \right]. \quad (5)$$

For most of the kinematic domain, the reduced DIS neutral current scattering cross section is well approximated by the F_2 structure function, since F_L leads to a sizeable effect only for large inelasticity values y .

The reduced cross section σ_r can be re-expressed as

$$\sigma_r = \frac{Q^2(1-x)}{4\pi^2\alpha} \sigma_{\gamma^*p}^{\text{eff}}, \quad (6)$$

with the effective virtual photon-proton cross section

$$\sigma_{\gamma^*p}^{\text{eff}} = \sigma_T + [1 - f(y)] \sigma_L. \quad (7)$$

The sum $\sigma_L + \sigma_T$ is referred to as the total virtual photon-proton cross section, $\sigma_{\gamma^*p}^{\text{tot}}$, which is often expressed as a function of Q^2 and of the invariant mass of the virtual photon-proton system, W . For small x , W can be calculated as $W = \sqrt{Q^2(1-x)/x}$, such that $W^2 \simeq sy$. The total and the effective virtual photon-proton cross sections differ significantly only in the region of high y .

3 Models

The low x data presented here extend to low values of Q^2 for which perturbative QCD is not applicable. The phenomenological models formulated for this transition region reproduce the W dependence of the γ^*p cross section, which is weak in the photoproduction region [40]. A steep increase towards large values of W develops in the perturbative region, which is equivalent to the rise of the proton structure function F_2 towards low x at fixed Q^2 .

In the context of the present measurement colour dipole models (*e.g.* [41–46]) are particularly interesting because F_L and $F_T = F_2 - F_L$ are both described by a single characteristic dipole scattering cross section $\hat{\sigma}$ combined with either the longitudinal or the transverse photon wavefunction. The squares of the wavefunctions of the $q\bar{q}$ fluctuations of longitudinally and transversally polarised photons are [30]

$$\begin{aligned} W_L(z, r, Q^2) &= \frac{6\alpha}{\pi^2} \sum_{i=1}^{n_f} e_i^2 Q^2 z^2 (1-z)^2 K_0(\epsilon r)^2, \\ W_T(z, r, Q^2) &= \frac{3\alpha}{2\pi^2} \sum_{i=1}^{n_f} e_i^2 [(1-2z(1-z))\epsilon^2 K_1(\epsilon r) + m_i^2 K_0(\epsilon r)], \end{aligned} \quad (8)$$

where $\epsilon^2 = m_i^2 + z(1-z)Q^2$, m_i (e_i) is the mass (charge) of quark i , $K_0(u)$ and $K_1(u) = -\partial_u K_0$ are modified Bessel functions, r is the transverse separation of the $q\bar{q}$ pair and z denotes the fractional energy sharing between q and \bar{q} . In this approach the cross sections $\sigma_{T,L}$ are obtained from integrals over the impact parameter space as

$$\sigma_{L,T}(x, Q^2) = \int d^2r \int_0^1 dz W_{L,T}(z, r, Q^2) \hat{\sigma}(x, r^2). \quad (9)$$

Colour dipole models differ by the chosen expressions for the cross section $\hat{\sigma}$. With the measurement extending into the region of high y one can confront the predictions of such models for the two structure functions with the data. As an illustration, the data are compared in this paper to two versions of the colour dipole model, the original version by Golec-Biernat and Wüsthoff

(GBW) [42] and a more recent model, based on the Colour Glass Condensate approach to the high parton density regime, by Iancu, Itakura and Munier (IIM) [45].

Two further models are used in this paper in order to parameterise $F_2(x, Q^2)$. The fractal model is based on the observation that the proton structure at low x exhibits self-similar properties for different x and Q^2 values. Two continuous, variable and correlated fractal dimensions are chosen to describe the self-similarity in x and Q^2 [33]. In a more phenomenological approach F_2 is parameterised as $x^{-\lambda(Q^2)}$. These two models are also compared with the reduced cross section, σ_r , after making assumptions on R .

4 Measurement of the DIS Cross Section

4.1 Reconstruction of Event Kinematics

In the colliding beam experiments at HERA, the DIS event kinematics can be reconstructed using the measurements of the scattered lepton, the hadronic final state, or a combination of the two. This complementarity enlarges the kinematic coverage and provides an additional control of the systematic uncertainties.

The energy of the scattered positron E'_e and its polar angle θ_e are used in the “electron method” to determine the kinematics via

$$y_e = \frac{2E_e - E'_e(1 - \cos \theta_e)}{2E_e} \equiv \frac{2E_e - \Sigma_e}{2E_e}, \quad (10)$$

$$Q_e^2 = \frac{E_e'^2 \sin^2 \theta_e}{1 - y_e}, \quad x_e = \frac{Q_e^2}{4E_p E_e y_e}. \quad (11)$$

Using energy-momentum conservation, the event kinematics can also be determined from the hadronic final state. An important quantity is the difference between the total energy and the total longitudinal momentum

$$E - P_z \equiv E'_e(1 - \cos \theta_e) + \sum_i (E_i - P_{z,i}) \equiv \Sigma_e + \Sigma_h, \quad (12)$$

where E_i ($P_{z,i}$) is the reconstructed energy (longitudinal component of the momentum) of a particle i from the hadronic final state. In the reconstruction masses are neglected for both the positron and the hadronic final state particles. The measured $E - P_z$ is insensitive to losses in the proton beam direction and is thus only weakly affected by the incomplete reconstruction of the proton remnant. For non-radiative events, the relation $E - P_z \simeq 2E_e$ holds. This allows $2E_e - \Sigma_e$ in equation 10 to be replaced by Σ_h and leads to the introduction of the y_h variable [47]

$$y_h = \frac{\Sigma_h}{2E_e}. \quad (13)$$

For events in which a photon is emitted collinearly to the incoming positron, the radiated photon is not reconstructed in the sub-detectors used to calculate $E - P_z$. In this case $(E - P_z)/2$ is equal to an “effective” incident positron beam energy, reduced relatively to the nominal beam

energy by the momentum carried by the radiated photon. This is employed in the Σ method, for which $2E_e$ in equation 13 is substituted by the measured $E - P_z$ [48]

$$y_\Sigma = \frac{\Sigma_h}{E - P_z} . \quad (14)$$

For this method, Q^2 is calculated by replacing y_e in equation 11 by y_Σ , and Bjorken x is calculated by substituting y_e , Q_e^2 and $2E_e$ by y_Σ , Q_Σ^2 and $E - P_z$, respectively³

$$Q_\Sigma^2 = \frac{E_e'^2 \sin^2 \theta_e}{1 - y_\Sigma} , \quad x_\Sigma = \frac{Q_\Sigma^2}{2 E_p y_\Sigma} \cdot \frac{1}{E - P_z} . \quad (15)$$

By using a consistent set of the variables x_Σ , y_Σ and Q_Σ^2 , the measurement also correctly reconstructs the kinematics for events with initial state QED radiation. Therefore, the method covers lower Q^2 and higher x values, which become accessible due to the reduced centre-of-mass energy for these events.

The total transverse momentum of the hadronic final state is

$$P_T^h = \left| \sum_i \mathbf{P}_{T,i} \right| \quad (16)$$

where $\mathbf{P}_{T,i}$ is the transverse momentum vector of the particle i and the sum runs over all particles. P_T^h is rather insensitive to particle losses collinear to the beam for a wide range of y . The combination of P_T^h and Σ_h defines the hadronic scattering angle

$$\tan \frac{\theta_h}{2} = \frac{\Sigma_h}{P_T^h} , \quad (17)$$

which, within the QPM, follows the direction of the struck quark.

In this analysis, both the electron and the Σ methods are used for the cross section measurement. The electron method provides the better resolution in x for large inelasticities $y > 0.1$, but the resolution degrades as $1/y$. Use of the Σ method extends the measurement down to $y \sim 0.002$. Below this y value, losses along the proton beam direction become important and are difficult to estimate. The Σ method as is used here noticeably increases the kinematic coverage towards low Q^2 and high Bjorken x due to initial state QED radiation.

4.2 Determination of the DIS Cross Section

The measurement of the double differential cross section is performed in bins of x and Q^2 , or y and Q^2 , depending on the region in the kinematic phase space, as shown in figure 1. The bin sizes and shapes as well as methods used for the kinematic reconstruction are chosen based on the following prescription:

- In Q^2 , a binning equidistant in $\log_{10} Q^2$ is chosen with eight bins per decade, as in previous H1 publications [37]. This binning reflects the good Q^2 resolution of the H1 detector.

³Note that in previous H1 publications the nominal positron beam energy was used instead of $(E - P_z)/2$ in the calculation of x_Σ . The method of x calculation used here is called the $I\Sigma$ method in [48].

- The x and Q^2 values at which the measured double differential cross section is quoted, also referred to as bin centres, are placed at an approximately logarithmic average value within the bin boundaries for the x and Q^2 binning, and at the linear average for the y binning.
- For high $y > 0.6$, the electron method has an excellent kinematic resolution. In this region, the measured cross section is sensitive to the longitudinal structure function F_L , which leads to a rapidly changing shape of the reduced cross section as a function of y . Therefore a fine binning, linear in y , is chosen for $y > 0.6$: two y bins are used for each Q^2 interval with boundaries at $y = 0.85, 0.75$ and 0.6 .
- For $y < 0.6$ the binning is defined in x . The default x binning is equidistant in $\log_{10} x$ with five bins per decade, as chosen previously [37]. The transition between the x and y binning is defined by the y value of the nominal bin centre, y_c , for the transition bins: for $y_c > 0.6$, the bin is combined with the nearest y bin and for $y_c \leq 0.6$ it is combined with the nearest x bin.

The resolution in each bin is checked using a Monte Carlo simulation. Two variables are calculated for this purpose, the purity $P = N_{\text{rec,gen}}/N_{\text{rec}}$ and the stability $S = N_{\text{rec,gen}}/N_{\text{gen}}$, where N_{rec} (N_{gen}) is the total number of reconstructed (generated) Monte Carlo events in the bin and $N_{\text{rec,gen}}$ is the number of events which are both generated and reconstructed in the same bin. The purity and stability are calculated for both the electron and the Σ methods. For the cross section measurement the method with the higher purity is used. The choices are illustrated in figure 1. The purity and stability typically exceed 50%. If either the purity or the stability is below 25% in a bin for the chosen reconstruction method, the bin is combined with an adjacent bin. Bins with larger sizes can thus be created at the acceptance edges as shown in figure 1.

The $\theta_e = 176.5^\circ$ and $\theta_e = 178^\circ$ lines in figure 1 indicate the approximate angular acceptance limits of the H1 detector for the nominal and the shifted vertex positions, respectively. In each plot measurement bins below θ_e lines are visible. The measurement in these bins becomes possible using the Σ method for events with initial state photon radiation which effectively reduces the centre-of-mass energy. These bins are further referred to as ISR bins. The Σ method cannot be used at high y , where its resolution is poor, leading to large migrations of nominal energy events into the ISR bins and thus to purities below the accepted value. This causes the gap between the ISR and electron method bins at high y .

The calculation of the reduced double differential ep cross section is performed by correcting the data using the MC simulations. The following formula is applied to each analysis bin

$$\sigma_r(x_c, Q_c^2) = \frac{N_{\text{data}} - N_{\text{bg}}}{A \epsilon \mathcal{L}_{\text{data}}} \frac{c_{\text{bc}}}{1 + \delta_{\text{rc}}} . \quad (18)$$

Here, (x_c, Q_c^2) is the bin centre, N_{data} is the number of data events, N_{bg} is the number of background events, estimated using MC simulations, A and ϵ are the detector acceptance and efficiency, $\mathcal{L}_{\text{data}}$ is the integrated luminosity, δ_{rc} are QED radiative corrections, and c_{bc} are the corrections for finite bin size effects. The radiative and bin centre corrections can be determined using the Monte Carlo simulation. In this case, equation 18 becomes

$$\sigma_r(x_c, Q_c^2) = \frac{N_{\text{data}} - N_{\text{bg}}}{N_{\text{MC}}} \frac{\mathcal{L}_{\text{MC}}}{\mathcal{L}_{\text{data}}} \sigma_r^{\text{MC}}(x_c, Q_c^2) , \quad (19)$$

where N_{MC} is the number of signal MC events and $\mathcal{L}_{\text{MC}} = N_{\text{gen}}/\sigma_{\text{gen}}$ is the Monte Carlo luminosity. Here N_{gen} denotes the total number of generated MC events and σ_{gen} is the total integrated cross section for the MC generation. The quantity $\sigma_r^{\text{MC}}(x_c, Q_c^2)$ is the reduced double differential cross section at the bin centre calculated at the Born level with the same structure functions as are used in the MC generation.

The correction for the detector acceptance using Monte Carlo modelling requires the cross section model used in the simulation to be sufficiently close to the data, such that migrations between the bins are well reproduced. The cross section model should also describe the kinematic region outside the measurement range, in particular at low y and low Q^2 , to account for radiative corrections and long range migrations. In practice, this is achieved using an iterative MC event reweighting procedure which converges after one iteration for the measurement region. First, the double differential cross section is measured following equation 19 using an initial approximation for the MC input cross section. Next, the measured double differential cross section is fitted with a new parameterisation using the fractal model and the analysis of the Monte Carlo events is repeated with an additional weight factor, equal to the ratio of the new to the initial double differential cross sections in each simulated event. For the reweighting, the event kinematics are calculated using the generated x and Q^2 variables at the hadronic vertex, such that corrections due to radiation from the lepton line are properly accounted for. This reweighting procedure is used for the measurement region. For the high $x > 0.02$ domain, which lies outside the measurement region, the ALLM parameterisation [49] is used.

5 H1 Detector

5.1 Overview

A complete description of the H1 detector is given in [50,51]. Here the components used for the present measurement are discussed. In section 5.2 the detectors for the scattered electron measurement are described in detail. A schematic view of the H1 detector is given in figure 2, in which a typical low Q^2 event is shown.

Around the interaction region a set of tracking chambers, surrounded by electromagnetic and hadronic calorimeters, operates in a solenoidal magnetic field of 1.16 T. The tracking system is subdivided into forward, central and backward tracking devices. The nominal interaction point of the electron and proton beams lies about in the middle of the Central Tracker, at the origin of the coordinate system. The interaction vertex positions have an approximately Gaussian distribution in z with $\sigma_z \approx 10$ cm. The calorimetry system consists of the Liquid Argon calorimeter (LAr) covering the central and forward directions and the lead-scintillator spaghetti calorimeter (SpaCal) [52–55] measuring particles scattered backwards.

The Central Tracker consists of four drift chambers, two multi-wire proportional chambers (MWPCs) and a silicon tracking device. The largest tracker components are the two concentric drift chambers, CJC1 and CJC2, which have sense wires strung parallel to the beam axis with the drift cells inclined at about 30° with respect to the radial direction, such that the drift direction of ionisation electrons is approximately perpendicular to the wire plane. The charge deposits are read out from both ends of each wire, providing particle identification via ionisation energy

loss and an approximate determination of the z coordinate via the charge asymmetry between the two wire end signals (“charge division”).

Tracks found in the CJC are linked to the hits found in two chambers equipped with wires strung around the beam axis, following polygonal support structures, dedicated to the precise measurement of z coordinates. The inner z chamber (CIZ) is located inside CJC1 and the outer z chamber (COZ) lies between CJC1 and CJC2. To reduce the number of acceptable combinations with the CJC, the z chambers also determine a ϕ coordinate using the charge division measurement. The tracks are further constrained by linking to hits in the central silicon tracker (CST) [56]. The CST consists of two layers of double-sided silicon strip detectors surrounding the beam pipe, covering an angular range of $30^\circ < \theta < 150^\circ$ for tracks passing through both layers.

The two cylindrical proportional chambers, the CIP mounted inside CIZ, and the COP located between the COZ and CJC2, are used together to identify tracks pointing to the interaction vertex and thus to reduce background at the trigger level. A combined CIP-COP signal is used in coincidence with the SpaCal to trigger events with low E'_e (see section 6.1).

The LAr calorimeter [57], mounted in a large cryostat, is used in this analysis for the measurement of the hadronic energy. The angular coverage of the calorimeter is $4^\circ < \theta < 154^\circ$ for an interaction vertex at $z = 0$. The calorimeter consists of an electromagnetic section with lead absorbers (20–30 radiation lengths) and a hadronic section with steel absorbers. The total depth is between 4.5 and 8 hadronic interaction lengths. The LAr calorimeter is divided along the z direction into wheels. The electromagnetic section has eight wheels while the hadronic section has seven. The calorimeter has a high degree of spatial segmentation with a total of about 45000 cells. Its hadronic energy resolution, as determined in test beam measurements [58], is $\sigma_E/E \approx 50\% / \sqrt{E/\text{GeV}} \oplus 2\%$.

Two electromagnetic crystal calorimeters, a photon tagger (PT) and an electron tagger (ET), located at $z = -103.1$ m and $z = -33$ m, respectively, are used to monitor the luminosity via the measurement of the Bethe-Heitler process $ep \rightarrow \gamma ep$. The luminosity corresponding to the main interaction region can be separated from the additional (“satellite”) interaction regions using information from the scintillator hodoscopes of the time-of-flight system (TOF) and from the HERA proton pick-up (PPU) monitor, a 34 cm long stripline device located at -3 m from the interaction point. The ET can be used to measure the scattered electron in photoproduction processes, with $Q^2 \leq 10^{-2} \text{ GeV}^2$ and $0.2 < y < 0.7$. The PT detects photons radiated collinearly to the incoming electron direction.

5.2 Backward Detectors

The measurement of the inelastic ep scattering cross section at low Q^2 relies on the identification of the scattered electron in the backward part of the H1 apparatus. The energy of the scattered electron is measured in the SpaCal calorimeter. For the low Q^2 region under study, θ_e lies outside the angular acceptance of the Central Tracker. The polar angle of the scattered electron can, however, be measured either by the Backward Silicon Tracker (BST), based solely on the electron track, or by a combination of the less precise Backward Drift Chamber (BDC) signal with the hadronic final state vertex, as reconstructed using the Central Tracker. The redundancy of the angular measurements provides additional cross checks over a large angular range, whilst the BDC extends the polar angle coverage to larger θ_e .

5.2.1 Backward Silicon Tracker

The BST in the configuration installed in 1999 [59] is schematically shown in figure 3. It consists of eight planes (disks) and 16 azimuthal sectors. The planes are mounted perpendicularly to the beam axis and are arranged in two modules, BST1 and BST2, of four planes each. A first version of the BST with four planes is described in [60].

Each BST plane is equipped with 16 wedge shaped, single sided, double metal, silicon strip sensors of $250\ \mu\text{m}$ thickness. Each sensor contains 640 sensitive p strips which are concentric around the beam axis with a pitch of $96\ \mu\text{m}$. The signals are amplified and temporarily stored by five on-detector front-end chips, called Analogue Pipeline Chips [61] (APCs), until a readout instruction is received [62]. Using these “ r sensors” (figure 4a) the track polar angle can be determined. The acceptance range of the BST for the nominal vertex position is $164^\circ < \theta_e < 176^\circ$.

In addition to the r sensors, each plane contains one single sided, single metal, silicon strip sensor, in the azimuthal sector $45^\circ < \phi < 67.5^\circ$ mounted behind the r sensor. This “ u sensor” has 640 sensitive strips parallel to the reference edge of the sensor with a pitch of $75\ \mu\text{m}$ (figure 4b). It thus measures hits in u coordinate space defined by $u = r \sin \phi_u$, where ϕ_u is the azimuthal angle with respect to the reference edge of the sensor. Combining the information from r and u sensors, it is possible to measure the transverse momentum and determine the charge of a track in the BST. This feature is used in this analysis to cross check the simulation of photoproduction background.

During data taking an online hit finding is performed. This takes into account individual pedestals of each channel, which are dynamically updated. Coherent shifts in the amplitude of groups of strips, so called “common mode”, are also corrected for. For reconstructed tracks, the most probable signal-to-noise values for the hits is about 15 for the r sensors and 30 for the u sensors. The single hit resolution is $20\ (15)\ \mu\text{m}$ for the r (u) coordinate.

5.2.2 SpaCal and BDC

The SpaCal calorimeter covers the polar angle range of $153^\circ < \theta < 177^\circ$ as measured from the nominal z vertex position. It consists of an electromagnetic section [53–55] with 1192 cells of size $4.05 \times 4.05 \times 25\ \text{cm}^3$ in front of a hadronic section with 136 cells of size $11.9 \times 11.9 \times 25\ \text{cm}^3$. The total amount of passive material traversed by particles from the interaction vertex up to the SpaCal is of the order of one radiation length. The electromagnetic section comprises 27.5 radiation lengths and provides an electromagnetic energy resolution of $\sigma_E/E = 7\% / \sqrt{E/\text{GeV}} \oplus 1\%$. The hadronic section [52] is used for a coarse hadronic energy measurement and to distinguish hadronic from electromagnetic showers. The whole calorimeter comprises 2 hadronic interaction lengths. The energy resolution for hadrons amounts to $\sigma_E/E \sim 60\% / \sqrt{E/\text{GeV}}$.

The SpaCal cells consist of lead sheets with embedded scintillating fibres. The fibres from each cell are bundled together and attached via light mixers to photomultiplier tubes (PMTs). The stability of the PMT gain can be checked using a dedicated LED system.

The backward drift chamber [63] is mounted in front of the SpaCal and has the same angular acceptance. It consists of four double layers, each of them divided azimuthally into eight sectors. A three dimensional view of a section of the BDC is given in figure 5. The sense wires are

Trigger Name	Energy Threshold	Effective r_{sp} Cut	Tracking Condition
S3	12.0 GeV	10 cm	—
S0	6.5 GeV	12 cm	—
S9	2.0 GeV	15 cm	CIP-COP track

Table 1: Overview of the main trigger conditions used for the NVX and SVX analyses. r_{sp} is the radial coordinate of the SpaCal cluster.

strung perpendicularly to the beam axis and are fixed at the sector edges leading to an octagonal geometry with almost radial drift directions. The drift cells are 1 cm wide in the inner region and 3 cm wide in the outer. At the transition from the inner to the outer region a special cell is introduced with 0.5 cm drift distance at the inner side and 1.5 cm drift distance at the outer. The cells within one double layer are shifted by half a drift cell in the radial direction to solve the inner-outer hit assignment ambiguity. The double layers are rotated by 11.25° with respect to each other to allow for reconstruction of the azimuthal coordinate. In addition, this reduces the efficiency losses at the sector edges. The radial resolution for minimum ionising particles is $400\mu\text{m}$. The resolution in the azimuthal direction is about 2 mm.

6 Data Collection and Reconstruction

The H1 detector uses a multi-level trigger system for data collection in which two hardware trigger levels are followed by a software filter farm. After improvements of the detector calibration and the reconstruction code, the data are reprocessed offline. This section describes the first analysis stages, including the online data selection and the reconstruction algorithms.

6.1 Online Event Selection

The online trigger conditions used in this analysis (table 1) are based primarily on a localised energy deposition in the electromagnetic section of the SpaCal (inclusive electron trigger). Three different energy thresholds are used. The trigger condition based on the lowest energy threshold (S9) collects events at the highest y . Since a significant background contamination is present at low energies and radii, the inner SpaCal region is excluded from S9. To maintain an acceptable trigger rate, S9 contains an extra condition requiring the pattern of hit pads in the CIP-COP proportional chambers to be consistent with at least one vertex pointing track. This condition is similar to the requirement of a reconstructed track from the hadronic final state in the Central Tracker.

6.2 Track and Vertex Reconstruction in the Central Tracker

The track reconstruction in the Central Tracker is initiated from the CJC hit measurements. Initially, candidate trajectories are found in the xy plane using a fast circle fit algorithm [64]. The z coordinate is added to the tracks based on charge division information. A linear fit in

$S - z$ space is performed where the S coordinate measures an arc length of the track in the xy projection. Next, the tracks are fitted to a common vertex in the xy plane. At this stage detailed corrections are applied for multiple scattering in the detector material and for magnetic field non-uniformity. For the tracks which are determined by the fit to originate from a common xy vertex, a combined $S - z$ fit is performed to determine an initial approximation of the vertex z position and of the track polar angles.

The vertex-fitted CJC tracks are then combined with hits found in the z chambers, employing a robust global minimisation technique [65]. This link improves the z vertex resolution from about 1 cm to 1 mm. The track θ resolution is correspondingly improved from approximately 10 mrad to 1 mrad. For the NVX sample, where the z coordinate of the interaction vertex is around zero, the CJC tracks are also combined with hits found in the CST resulting in a vertex resolution of about 0.1 mm. CST hits are not used for the SVX sample since the interaction vertex position is outside the CST acceptance.

6.3 Reconstruction of the Electron Kinematics

6.3.1 Energy Reconstruction in the SpaCal Calorimeter

The reconstruction of the scattered electron kinematics is based on the measurement of a deposition of energy, termed a cluster, found in the electromagnetic SpaCal. The clustering algorithm searches for a cell with a local maximum in energy. The cluster is then built around this seed cell by adding neighbouring cells with energies above the noise threshold. The centre-of-gravity of the cluster is determined based on all associated cells using a logarithmic energy weighting. To suppress background from hadrons and from decays of $\pi^0 \rightarrow \gamma\gamma$ with the photons reconstructed in a single cluster, a cluster radius estimator, R_{\log} , is used based on logarithmic energy weighting. The background from hadronic particles is further suppressed using a cut on the energy deposit, E_{had} , in the hadronic section of the SpaCal behind the electromagnetic cluster.

The electron candidate cluster is required to be associated to a track in one of the backward trackers, BDC or BST, in order to reduce background from backward photons and to measure the polar angle θ_e accurately. For the determination of θ_e , the trajectory of the scattered electron is assumed to be a straight line in $r - z$ coordinate space.

6.3.2 Track Reconstruction in the BDC

The BDC reconstruction of the electron scattering angle θ_e starts from the line connecting the SpaCal cluster and the Central Tracker vertex as an initial approximation. The scattered electron azimuthal angle ϕ_e is taken from the SpaCal cluster centre-of-gravity. Only the BDC hits in the octant containing ϕ_e are used for the θ_e reconstruction.

The θ_e determination follows from a minimisation procedure. A least squares track fit combines the Central Tracker vertex, the SpaCal cluster centre-of-gravity energy, and all BDC measurements in a corridor of variable size Δr around the current best estimate of the track direction. Initially, the corridor has a size of 5 cm. It is gradually reduced with improved track parameters to about five times the BDC resolution. The SpaCal cluster is considered to be linked to the BDC track segment if there are at least four hits from the eight layers remaining at the final iteration and if the radial distance between the track projected to the SpaCal z coordinate and the SpaCal cluster is less than 2.5 cm.

6.3.3 Track Reconstruction in the BST

The reconstruction of the electron track in the BST uses the azimuthal location of the SpaCal cluster. The three adjacent sectors which in azimuth are closest to ϕ_e are selected. The r coordinates of all BST hits in the selected sectors are projected along the line defined by the hit and the SpaCal cluster to the BST plane closest to the SpaCal. A clustering of the projected hits in this plane is then performed using a histogram technique. The line connecting the position corresponding to the peak in the histogram and the SpaCal cluster is used as an initial approximation for the track.

The track finding then proceeds using an iterative minimisation technique with robust rejection of outliers, similar to the BDC reconstruction. All hits in the selected sectors are included into a least squares minimisation. The contribution of each hit is weighted with an exponential suppression factor, which depends on the distance from the hit to the track, and on an additional parameter, which defines the width of an effective corridor around the track. For the first iteration, the width of the corridor is equal to the SpaCal spatial resolution. For further iterations the width is gradually reduced until it reaches five times the BST spatial resolution. The event vertex z coordinate is given by the distance of closest approach of the BST track to the beam line.

For the sector equipped with the u strip detectors, the reconstruction of the azimuthal coordinate is also performed. At least three u hits associated to linked r hits are required. If multiple u hits per plane are found, all possible track combinations are formed and the one best matching the SpaCal cluster is selected. To determine the space points, the u hits are combined with the r hits extrapolated along the r track to the z position of the u sensor. Then the transformation $(r, u) \Rightarrow (x, y)$ is performed. A circle fit including the position of the interaction vertex in (x, y) determined by the beam spot size of $150\mu\text{m}$ in x and $60\mu\text{m}$ in y , yields the curvature and therefore charge and the transverse momentum of the particle.

6.4 Reconstruction of the Hadronic Final State

The reconstruction of the hadronic final state uses information from the central tracker and the LAr and SpaCal calorimeters, excluding a cone in the SpaCal calorimeter around the electron candidate cluster. The cone axis is defined by the vertex position and the centre-of-gravity of the SpaCal cluster. The cone radius is 20 cm at the surface of the SpaCal electromagnetic section. The energy of the cells inside the cone is excluded from the hadronic final state calculation for both the electromagnetic and hadronic sections of the SpaCal.

Tracks pointing to the backward part of the H1 detector are excluded from the hadronic final state. Instead, the reconstructed SpaCal clusters outside the electron isolation cone are used. In the central region, the Central Tracker and LAr signals are linked for each particle by matching the measurements in each detector. For energies below 2 GeV, the tracker information is used while for higher energies the calorimeter information is used, as it provides the better energy resolution.

The determination of Σ_h is affected by the presence of extra activity in the calorimeters. The bias is particularly strong for small Σ_h and thus small y_h . For the SpaCal, this extra activity can be induced by the scattered electron, with some energy leaking outside the isolation cone or by

a radiated photon emitted at a large angle. The contribution of these sources of extra activity to Σ_h is proportional to Σ_e to good approximation. To reduce the influence of these effects, 10% of Σ_e is subtracted from the total SpaCal Σ_h . If the result is negative, the SpaCal contribution is set to zero. This procedure reduces the contribution of SpaCal to Σ_h to a negligible level for low y events, as is expected from the event kinematics.

Channels affected by electronic noise in the LAr are identified event by event using a dedicated topological algorithm. LAr cells with an energy below 0.4 GeV (0.8 GeV), which are separated from other cells by more than 40 cm (20 cm) in the central (forward) region of the calorimeter are classified as noise and excluded from the Σ_h and P_T^h calculations.

7 Monte Carlo Simulations

In the simulation, DIS events are generated using the DJANGO 1.4 [66] event generator which includes leading order QED radiative effects as implemented in HERACLES [67]. For the event generation, leading order parton distribution functions define F_2 while F_L is set to zero. The structure functions are subsequently reweighted to the fractal model parameterisation of F_2 and to F_L following the procedure described in section 4.2. The final state parton showers are simulated using the Colour Dipole Model [68,69] as implemented in ARIADNE 4.1 [70]. Events with a very low mass of the hadronic final state ($W < 5$ GeV) are simulated using SOPHIA [71], which includes a detailed description of low mass final states, including the resonance region. The fragmentation into hadrons is performed with JETSET 7.4 [72]. Photoproduction background is generated with the PHOJET 1.6 [73,74] program, which uses a two-component dual parton model [75] including diffractive processes and vector meson production.

The simulation of QED radiative corrections includes photon emission from the lepton. Radiation from quarks, which is estimated to be small for low x , is not simulated. The simulation of QED radiative corrections is checked using the analytical calculation package HECTOR [76]. An agreement to better than 0.5% is found in the kinematic range of this measurement.

The generated events are passed through a simulation of the H1 detector response based on the GEANT3 [77] package. Tracing of the particles in the trackers up to the calorimeters is based on a detailed description of the detector material. The response of the calorimeters to electromagnetic particles is simulated using a fast shower parameterisation technique [78], while the hadronic response is simulated using GHEISHA [79].

The level of noise and beam related background in the calorimeters is determined using events from dedicated runs with random triggers which are overlaid on the simulated events. Spurious hits in the BST are added to the simulation based on randomly triggered events.

The MC events are subjected to the same reconstruction and analysis procedure as the data. Also, for consistency of the analysis, the calibrations of the SpaCal and the LAr, as well as the BST and BDC alignments, are performed for the reconstructed MC events in the same way as for the data.

Analysis	Trigger	Description
NVX ($z_{\text{vtx}} \sim 0$ cm)		
NVX-BST	S0	Main analysis
NVX-S9	S9	Extension to lower E'_e
SVX ($z_{\text{vtx}} \sim 70$ cm)		
SVX-BST	S0	Main analysis
SVX-BDC	S0, S3	Extension to larger θ_e

Table 2: Inclusive analyses of DIS data. The trigger conditions used to collect the data sets are described in section 6.1, table 1.

8 Data Analysis

At low Q^2 the DIS cross section is large, and for the available integrated luminosity for this analysis the statistical uncertainty of the measurement becomes smaller than the systematic uncertainty. For low inelasticities, corresponding to a large fraction of the measured phase space, the scattered electron energy is large and background contributions are negligible compared to the genuine DIS signal. In this region a set of selection criteria is imposed which is sufficient to reconstruct the event kinematics in the least biased way. Whenever possible the electron trajectory is reconstructed using the BST alone and only the SpaCal is used for triggering.

Events with the scattered electron outside the BST acceptance are reconstructed using the BDC and the Central Tracker vertex. The analysis is also extended to the highest accessible y values for which the precision is limited by the uncertainty of photoproduction background. In this region several additional electron identification criteria are imposed in order to minimise the systematic uncertainty.

For the two data samples, NVX and SVX, a total of four separate analyses is performed as summarised in table 2. The analyses differ in the triggers and in the method employed for reconstructing θ_e . The main kinematic region of the NVX-BST data set, with θ_e measured in the BST, is analysed based on the trigger S0. An extension to $0.75 < y < 0.85$ is achieved using the trigger S9 (NVX-S9) and requiring signals in both tracking detectors, BDC and BST. For the SVX sample, the main region of the phase space is covered by a BST-based analysis with the trigger S0 (SVX-BST). An extension to $\theta_e = 178^\circ$ is achieved by adding data collected with the trigger S3 and including events with θ_e measured by a combination of the Central Tracker vertex and BDC information (SVX-BDC).

The measurement is verified by performing a number of cross check analyses exploiting the redundancy in the kinematic reconstruction and the large overlap of the kinematic regions of different data sets. The data reconstructed with the BST are compared with those reconstructed with the BDC. The results of the electron method are cross checked with those of the Σ method. Moreover, the measurement based on the shifted vertex sample is compared to that based on the nominal vertex sample.

In the following a detailed description of the different analyses is given. Further information can be found in [80–83].

Description	Cut
Common cuts	
Scattered electron energy	$E'_e > 7 \text{ GeV}; 4 \text{ GeV (NVX-S9)}$
Vertex z position	$ z_{\text{vtx}} - z_{\text{nom}} < 35 \text{ cm}$
SpaCal cluster radius	$R_{\text{log}} < 4 \text{ cm}$
Hadronic energy fraction	$E_{\text{had}}/E'_e < 0.15$
P_{T} balance	$P_{\text{T}}^h/P_{\text{T}}^e > 0.3$
Electron method cuts	
$E-P_z$ balance	$E-P_z > 35 \text{ GeV}$
BST analysis cuts for NVX-S9, NVX-BST and SVX-BST	
BST validation	$N_{\text{link BST}} \geq 2 \text{ (NVX)}; 3 \text{ (SVX)}$
BST-SpaCal radial match	$ \Delta r_{\text{BST-SpaCal}} < 1.5 \text{ cm}$
BST noise	$N_{\text{hit total}} < 120 \text{ (NVX)}; 200 \text{ (SVX)}$
BDC analysis cuts for SVX-BDC	
BDC validation	$N_{\text{link BDC}} \geq 4$
BDC-SpaCal radial match	$ \Delta r_{\text{BDC-SpaCal}} < 2.5 \text{ cm}$
Central Tracker vertex	$N_{\text{track}} \geq 1$ $y_{\Sigma} \geq 0.03$
Additional NVX-S9 analysis cuts	
BST-BDC radial match	$ \Delta r_{\text{BST-BDC}} < 0.75 \text{ cm}$
BST-CT z_{vtx} match	$ z_{\text{VTX,BST}} - z_{\text{VTX,CT}} /\sigma < 5.0$
Central Tracker vertex	$N_{\text{track}} \geq 2$

Table 3: Selection criteria used in the analysis.

8.1 Event Selection

8.1.1 Criteria

An overview of the selection criteria used in the different analyses is given in table 3. The background from non- ep interactions is suppressed by requiring the event vertex (z_{vtx}) to be reconstructed within a distance of $\pm 35 \text{ cm}$ from the average z position (z_{nom}). In order to be identified with the scattered electron, the highest energy cluster in the electromagnetic SpaCal section⁴ has to satisfy the following criteria: (i) the cluster centre-of-gravity lies in the region of high efficiency of the corresponding trigger; (ii) the transverse cluster radius is consistent with an electromagnetic particle, $R_{\text{log}} < 4 \text{ cm}$; (iii) the energy deposition in the hadronic SpaCal section behind the cluster is small, $E_{\text{had}}/E'_e < 0.15$; (iv) depending on the analysis, the cluster is validated by a BST or a BDC track segment. If the highest energy cluster does not satisfy one of these cuts, the next highest energy cluster is used. This procedure is repeated for up to three clusters with energies above 7 GeV, or 4 GeV (NVX-S9).

The further event selection is based on a global balance between the hadronic final state and the electron. Events for which the hadronic final state is poorly reconstructed are rejected

⁴For the S9 analysis (table 2) the cluster with the maximum transverse momentum P_{T}^e is chosen instead of the highest energy cluster.

by demanding that the total hadronic transverse momentum P_T^h be at least 30% of the electron transverse momentum P_T^e . This efficiently removes migrations from very low y , which lie outside the measurement region. Events with large initial state radiation are excluded from the electron method measurement by requiring $E - P_z > 35$ GeV. This condition is not used for the Σ method, which takes QED radiation properly into account.

The BST analyses include requirements on the minimum number of BST hits linked to the electron track ($N_{\text{link BST}}$) and on the matching of the BST track extrapolated to the z position of the SpaCal cluster, $\Delta r_{\text{BST-SpaCal}}$. Similarly, for the BDC based analyses, a minimum number of linked BDC hits ($N_{\text{link BDC}}$) and radial BDC-SpaCal matching ($\Delta r_{\text{BDC-SpaCal}}$) are required. In addition, the BST analyses require a low level of noise by cutting on the variable $N_{\text{hit total}}$, the total number of BST hits. The BDC analyses demand the presence of at least one central track (N_{track}).

The S9 analysis extends the measurement to low E'_e , corresponding to high y , where the largest uncertainty stems from the large photoproduction background. To suppress this background, both the BST and BDC track segments are required to pass the same criteria as in the other analyses. In addition, a tight matching condition is applied for the two trackers using $\Delta r_{\text{BST-BDC}}$, the radial distance between the BDC and BST tracks calculated at the BDC plane, as well as $|z_{\text{VTX,BST}} - z_{\text{VTX,CT}}|/\sigma$, the distance in z between the BST vertex and the Central Tracker vertex position divided by the uncertainty of this difference. Finally, to ensure a high trigger efficiency for the analysed sample, at least two central tracks must be reconstructed.

8.1.2 Efficiency Determination

The efficiencies of the triggers are determined using independently triggered data samples. For the SpaCal trigger conditions, most of the cells show a high ($> 99.5\%$) efficiency above the rather sharply defined threshold, see figure 6. A few cells are identified which show high thresholds. They are excluded from the analysis by applying geometrical cuts on the electron impact point reconstructed at the calorimeter surface, which is calculated using θ_e and ϕ_e . The efficiencies of the CIP-COP conditions employed in the S9 trigger (see section 6.1) are studied as functions of E'_e and the track multiplicity. Since the average reconstructed track multiplicity increases with Q^2 , the inefficiency diminishes from 3% at $Q^2 = 1$ GeV² to 2% at $Q^2 = 10$ GeV². The data are corrected for this inefficiency. The systematic uncertainty on the trigger efficiency is estimated to be 1% for S9 and 0.5% for the other triggers.

The inefficiency of the software filter farm component of the trigger is determined using a sample of the rejected events, recorded for cross checks. The primary reason for the rejection is the online reconstruction of the event vertex which occasionally wrongly classifies ep events as non- ep background. The loss corresponds to 0.7% for the NVX analysis and 0.8% (0.5%) for the SVX-BST (SVX-BDC) analysis. This loss is consistent with being uniform across the phase space and is applied as a global correction with a systematic uncertainty of size equal to the correction.

The efficiencies of the electron identification requirements (cluster shape, hadronic fraction, BDC or BST validation) for high energies of the scattered electron are evaluated using events passing all other selection cuts but the one to be investigated. This direct approach is applicable for $E'_e > 20$ GeV due to the negligible background.

For low E'_e , the electron identification efficiency is studied after the background subtraction. In addition, special background-free samples are used. One such sample comprises initial state radiation events with the radiated photon detected in the photon tagger. Background levels below 1% are achieved in this case, even for $E'_e \sim 3$ GeV, by requiring the sum of the photon tagger and scattered electron energies to be close to the electron beam energy. The efficiency of the electron identification cuts does not vary much as a function of E'_e . It is always above 90% and is well reproduced by the simulation.

The efficiency to find a central tracker vertex for the BDC analysis is determined using events with a reconstructed BST vertex. As shown in figure 7, it is larger than 50% for $y_\Sigma > 0.03$ and 93% for $y_\Sigma > 0.1$. The BDC analysis is restricted to $y_\Sigma > 0.03$. At larger values of y_Σ the efficiency decreases again, the effect being more pronounced in the data than in the simulation. The reason for this difference is a deficit of events with a large rapidity gap in the DJANGO model, as already observed in [35]. This is accounted for by applying a correction to the MC simulation. The systematic error of the cross section resulting from this correction is found to decrease with increasing Q^2 , from 10% to 2%.

A special procedure is developed to determine the BST inefficiency. Two main sources of inefficiency are distinguished which are both closely related to the readout procedure. The first is a hit finding inefficiency, which mostly depends on the performance of the front-end amplifier readout chip (APC). This efficiency is determined for each APC using BST tracks, requiring hits reconstructed in all but the BST plane under investigation. For most of the APCs the efficiency is high ($> 95\%$), but about 5% of APCs have efficiencies below 80%. A few BST regions, with an APC efficiency below 40%, are excluded from the analysis.

Correlated readout losses constitute the second source of inefficiency. In this case, signals are lost coherently in either BST1, BST2 or in both modules. The main source of coherent losses comes from timing desynchronisation at a level of about 5% with some dependence on the ϕ sector. The coherent losses are measured separately and combined for BST1 and BST2 for each ϕ sector. They are measured using a background-free DIS sample ($15 \text{ GeV} < E'_e < 32 \text{ GeV}$) with a well reconstructed CT vertex and BDC track. All sources of BST losses are incorporated into the simulation.

The efficiency of the BST track segment finder, used to reconstruct the event vertex within the nominal z range and to validate the SpaCal electron candidate, is checked globally for data and for the DJANGO simulation using events with a well reconstructed central vertex and a BDC track segment. The photoproduction background is suppressed by demanding $E'_e > 15 \text{ GeV}$. In this procedure not only is the BST efficiency examined, but the description of the BST acceptance and the imperfections of the tracking algorithm are also checked. Figure 8 and figure 9 show the global BST efficiency as a function of the electron candidate's radial position in the SpaCal for the NVX and SVX samples, respectively. Based on this comparison, the systematic uncertainty attributed to the description of the BST efficiency is taken to be 2% in both the NVX and the SVX data analyses. This value also includes uncertainties arising from inefficiencies of the other electron identification criteria described above.

The efficiency of the selection criteria based on the BDC, $N_{\text{link BDC}} \geq 4$ and $|\Delta r_{\text{BDC-SpaCal}}| < 1.5 \text{ cm}$, is determined for events with $E'_e > 20 \text{ GeV}$ for data and for the DJANGO simulation. A correction to the simulated events is applied to account for discrepancies which are largest in the narrow transition region from small to large cells in the BDC. Events in this region are

rejected from the NVX-S9 analysis. The systematic uncertainty attributed to the BDC efficiency amounts to 1.5%, also covering differences between data and the MC simulation for other electron selection criteria.

8.2 Subdetector Alignment and Calibration

8.2.1 Alignment

Alignment of the Central Tracker, BDC and SpaCal. The relative alignment of the H1 sub-detectors and the alignment of the detector with respect to the beam direction is performed in several steps. The first step is the internal alignment of the Central Tracker. The x and y coordinates are defined by the precisely known positions of the CJC wires while the z coordinate is defined by the COZ. Using cosmic muon tracks, the relative positions of the inner and the outer CJC parts, the location of the CIZ and the parameters for the z coordinate measurement in the CJC are determined. The beam axis is reconstructed by measuring the x and y coordinates of the interaction vertex as functions of its z coordinate.

The alignment of the SpaCal and of the BDC is performed using high energy electron candidates, with $E'_e > 20$ GeV, linked to a central track. The central track is required to have at least two reconstructed CIZ hits and the θ uncertainty must be smaller than 2 mrad. The x and y offsets of the BDC and the SpaCal are measured by studying the difference in the polar angle measurements for these electron candidates between the Central Tracker and the BDC, $\Delta\theta = \theta_{CT} - \theta_{BDC}$, and between the azimuthal angle measurements from the Central Tracker and the SpaCal, $\Delta\phi = \phi_{CT} - \phi_{SpaCal}$, as functions of the azimuthal angle ϕ_{SpaCal} . The two methods find a consistent alignment in the x direction. For the y direction, the alignment is found to be different by 2 mm between the $\Delta\theta$ and $\Delta\phi$ methods. The average of the two values is used to correct for the misalignment.

The z offset of the BDC is measured by studying $\Delta\theta$ versus θ_{CT} . The z offset of the SpaCal is checked by comparing the θ measurements in the BDC and in the SpaCal. The tilts of the backward detectors are studied using $\Delta\theta$ versus θ_{CT} for positive and negative x and y separately; they are found to be negligible. Figure 10 shows the comparison of the θ_e measurement in the Central Tracker and the BDC after alignment.

The SpaCal alignment with respect to the beam direction is cross-checked using quasi-elastic QED Compton (QEDC) events. These are ep scattering events of the type $ep \rightarrow e\gamma$ with a hard photon radiated from the lepton line, the proton being scattered quasi-elastically at low momentum transfer such that the outgoing electron and photon are detected in the main detector, nearly back-to-back in azimuth. The QEDC process is selected by requiring two energy deposits in the electromagnetic SpaCal section with energies above 4 GeV. The sum of both cluster energies is required to exceed 25 GeV. The back-to-back requirement is enforced by demanding $\cos \Delta\phi_{e\gamma} < -0.9$ with $\Delta\phi_{e\gamma}$ being the azimuthal angle between the electron and the photon. Elastic events are selected by demanding no tracks reconstructed in the CJC and low activity in the calorimeters apart from the selected electron and photon. This alignment agrees within 1 mm with the alignment obtained using central tracks.

The dominant uncertainty of the alignment stems from the difference in the y direction between the $\Delta\theta$ and $\Delta\phi$ methods. Since the H1 detector is nearly ϕ symmetric, biases in y

reconstruction do not lead to large shifts in the measured cross section. To cover a potential global bias of the θ_e measurement, a systematic uncertainty of 0.5 mrad is assigned for the polar angle reconstruction with the BDC and the Central Tracker.

BST alignment. In the global BST alignment, the position of the BST is determined with respect to the H1 coordinate system. In the internal BST alignment, radial offsets and rotations around the z axis of the individual wafers are determined. The global and internal alignments use the electron track reconstructed from the Central Tracker vertex and the BDC track segment as a reference and compare it to the track segment found in the BST.

During the detector assembly each sensor is fixed to its nominal position with a mechanical precision of about $100\ \mu\text{m}$. Remaining degrees of freedom are 128 radial shifts and 128 rotations of the wafers. For the r strip sensors, these parameters are determined for all detectors simultaneously using the global minimisation package Millepede [84]. The degeneracy between shifts and rotations is resolved utilising the wafer overlap regions. Typical shifts are less than $200\ \mu\text{m}$ and most rotations are less than 1 mrad. Figure 11a) shows the distribution of the number of BST linked hits as a function of ϕ_e . Figure 11b) shows the difference in the θ_e measurement between the two BST overlapping sectors in these cases, after the BST alignment. An agreement to better than 0.2 mrad is observed. Based on this study, the uncertainty on the scattered angle reconstruction by the BST is taken to be 0.2 mrad.

The alignment of the u strip detector is done in an analogous way. Here, shifts perpendicular to the u coordinate for the 8 wafers are determined simultaneously using the interaction vertex and the BDC measurement as additional external constraints. The shifts of up to about $100\ \mu\text{m}$ are included in the external alignment.

8.2.2 Electromagnetic Energy Calibration

The largest uncertainty in the electromagnetic energy calibration stems from fluctuations of the gain factors of the individual SpaCal photomultiplier tubes. During the data taking, an initial cross calibration of the SpaCal cells was performed using cosmic muons. The stability of the gains was controlled by means of a dedicated LED system. First corrections to the gain factors were applied using DIS events based on the position of the “kinematic peak” - an enhancement in the E'_e distribution close to the electron beam energy which is characteristic of DIS at low Q^2 at HERA.

At the analysis stage, a cell-by-cell gain determination is performed using the double angle (DA) calibration. The DA method is also used to perform additional non-uniformity corrections taking into account variations of the energy scale on the sub-cell size level. The SpaCal energy non-linearity, caused particularly by the energy losses in dead material in front of the calorimeter, is modelled in detail [85] using the H1 detector simulation based on the GEANT program [77]. The simulation is checked and corrected using $\pi^0 \rightarrow \gamma\gamma$ decays. Finally, the energy scale is checked using $J/\psi \rightarrow ee$ decays and QED Compton events. All calibration steps are described in the following.

Double Angle Calibration. The double angle calibration procedure makes use of kinematic peak events. Large statistics are available in this kinematic domain with negligible background contamination. For $y < 0.1$ the hadronic methods of y reconstruction (equations 13 and 14) have superior resolution. In particular, the scattered electron energy can be re-expressed in terms of the hadronic (equation 17) and electron scattering angles as

$$E_{\text{DA}} = \frac{E_e (1 - y_{\text{DA}})}{\sin^2 \frac{\theta_e}{2}}, \quad y_{\text{DA}} = \frac{\tan \frac{\theta_h}{2}}{\tan \frac{\theta_h}{2} + \tan \frac{\theta_e}{2}}. \quad (20)$$

In this method the scattered electron energy is calibrated to the electron beam energy⁵. The calibration corrects for genuine miscalibration and also energy loss in the dead material between the interaction point and the calorimeter. The same calibration procedure is applied separately to the data and the simulated events.

For the calibration, events with $E'_e > 20 \text{ GeV}$ are selected. The event vertex position and the scattered electron angle are measured using the BST. A good E_{DA} resolution is achieved by requiring $15^\circ < \theta_h < 80^\circ$. The calibration is performed by adjusting the gain factors of the individual SpaCal cells, such that the energy of the cluster agrees with the reference given by E_{DA} . This is achieved in an iterative procedure: for each selected event, a ratio $c_{\text{ev}} = E_{\text{DA}}/E'_e$ is calculated. The cluster energy is usually shared among several cells; the contribution of each cell with an energy E_i is given by $W_i = E_i/E'_e$. A W_i weighted average of c_{ev} for each calorimeter cell is then calculated based on all calibration events. This average is used to modify the gain factor at the next iteration. The calibration procedure converges after three iterations.

The cell-by-cell calibration is followed by calibrations as a function of (i) the distance between the centre-of-gravity of the cluster and the centre of the cell with highest energy to correct for biases of the clustering algorithm, (ii) $R_{\text{box}} = \max(|x_{\text{sp}}|, |y_{\text{sp}}|)$, where $x_{\text{sp}}, y_{\text{sp}}$ are the x and y cluster coordinates, in order to correct for energy losses in between SpaCal cells, and (iii) $r_{\text{sp}} = \sqrt{x_{\text{sp}}^2 + y_{\text{sp}}^2}$, to correct for losses in the dead material in front of the calorimeter. These additional corrections are applied sequentially.

The results of the double angle calibration are checked by comparing the distribution of the electron energy E'_e in the data and the simulation for the standard selection in the kinematic peak region. By comparing the widths of these distributions an additional Gaussian smearing of 1.1% (0.2%) is applied to the electron energies in the simulated events for the NVX (SVX) data set. The need for this smearing in the MC may be due to short time scale drifts of the photo-multiplier gain factors which are not simulated, to imperfections in the shower shape simulation or to a deficiency in the passive material simulation. For the NVX sample, the kinematic peak comparison is presented in Figure 12a). Figure 12b) shows the Kolmogorov-Smirnov (KS) test probability distribution as a function of the relative shift in the energy distribution between the data and the simulation. Shifts above 20 MeV are excluded, which corresponds to a relative energy scale agreement better than 0.1%. The systematic uncertainty on the relative energy scale at the kinematic peak is taken to be 0.2% to account for the uncertainties of the HERA beam energy, for uncertainties in the resolution adjustment in the simulation, deficiencies of the double angle method and a residual variation of the level of agreement in the kinematic peak between data and MC for different Q^2 bins.

⁵The influence of initial state radiation, which effectively reduces the electron beam energy, is small for this kinematic selection and is included in the simulation.

Calibration using $\pi^0 \rightarrow \gamma\gamma$. The double angle energy calibration determines the energy scale of the individual SpaCal cells and radially dependent corrections of the energy loss for scattered electron energies close to the electron beam energy. The deviations from the linearity of the SpaCal response are measured using $\pi^0 \rightarrow \gamma\gamma$ decays which probe much lower energies.

Events with two clusters in the electromagnetic SpaCal section are selected. The larger of the two cluster energies is required to be above 2.2 GeV, exceeding the trigger energy threshold, the smaller cluster energy is required to be above 0.7 GeV. The event vertex is determined from tracks reconstructed in the Central Tracker. The two clusters are assumed to be produced by two photons. The invariant mass, $M_{\gamma\gamma}$, is calculated using the reconstructed cluster energies and positions.

The simulation of $\pi^0 \rightarrow \gamma\gamma$ decays is checked using the PHOJET MC sample. A reasonable agreement of the simulation with the data is observed for the total energy of the two clusters as shown in figure 13a). The simulated π^0 energy spectrum is reweighted to that observed in the data, in order to reproduce the opening angle and individual photon energy distributions.

The two-photon mass distribution is shown in figure 13b). A prominent peak above the background is observed close to the nominal π^0 mass. The peak is shifted to lower values, around 130 MeV instead of 135 MeV. This difference is not reproduced by the MC simulation after the double angle calibration. The figure shows the distribution of simulated events after applying an additional correction of -3% to the energy scale for them. The data and the simulation are then in a good agreement. The shift of the peak is possibly caused by not fully simulated energy losses in the dead material in front of the calorimeter.

The low $\gamma\gamma$ invariant mass and the relatively high photon energy cuts in the study of $\pi^0 \rightarrow \gamma\gamma$ decays lead to a rather small separation between the photon clusters in SpaCal, with an average separation of only 13 cm. An overlap of the adjacent clusters could lead to an energy scale shift. Additional studies are performed to estimate this effect. The data sample is split into sub-samples with approximately equal statistics based on the larger or smaller cluster energy or on the cluster separation. In addition, the $M_{\gamma\gamma}$ distribution is studied as a function of the projected π^0 location in the calorimeter, the latter being calculated as an energy weighted sum of the two cluster positions. In all these studies the relative shifts of the energy scale in the data versus the simulation are consistent within 1% which is taken as a systematic uncertainty of the energy determination at $E'_e = 2$ GeV.

A check of the relative energy scale using π^0 decays is also performed for the SVX sample. The larger distance from the decay vertex to the calorimeter leads to larger separations between photon clusters, on average 18 cm. The relative shift of the $M_{\gamma\gamma}$ distribution between the data and the simulation after the double angle calibration is -2.7% in this case, consistent with the shift observed for the NVX sample.

The relative bias of the energy scale is corrected in the data assuming a linear dependence on E'_e . No correction is applied at $E'_e = 27.6$ GeV and a correction of $+3\%$ is applied at $E'_e = 2$ GeV. The systematic uncertainty of the energy scale determination is also assumed to follow a linear dependence rising from 0.2% at $E'_e = 27.6$ GeV to 1% at 2 GeV.

Tests of the SpaCal Energy Calibration. The SpaCal energy response is checked using $J/\psi \rightarrow ee$ decays and QED Compton $ep \rightarrow e\gamma$ events. The J/ψ candidates are selected

by requiring exactly two electromagnetic clusters with a total energy of less than 22 GeV. At least one of the two clusters has to be linked to either a BST or a CJC track and both clusters must be associated with a BDC track segment. Events with additional CJC tracks not associated to the electrons are rejected, thus selecting events from elastic J/ψ production. The event vertex is defined by the CJC or the BST tracks.

In this study, the SpaCal energy measurement is explicitly corrected to the absolute scale obtained from the mean ratio of the reconstructed to the generated electron energy from the DJANGO simulation. Both the double angle and π^0 calibration corrections are applied, so that the peak in the di-electron invariant mass M_{ee} distribution can be directly compared to the nominal J/ψ mass, $M_{J/\psi} = 3.096$ GeV.

The distribution of M_{ee} for the NVX data is shown in figure 14. A clear enhancement around the nominal J/ψ mass is observed. The data are fitted with a sum of a Gaussian for the signal peak and a second order polynomial to describe the background shape. The fit uses the binned maximum likelihood method. The measured Gaussian peak position agrees with $M_{J/\psi}$ within 1.3σ . Based on this agreement the deviation from the nominal energy scale is limited to be below 0.8% at 68% confidence level for energies of about 6 GeV.

QED Compton events are used to check the calorimeter energy scale in the intermediate energy region. For elastic events, the energy of the scattered electron is related [86] to the polar angles of the scattered electron θ_e and the photon θ_γ by

$$E_{\text{QEDC}}^{\text{DA}} = \frac{2E_e \sin \theta_\gamma}{\sin \theta_e + \sin \theta_\gamma - \sin(\theta_e + \theta_\gamma)}. \quad (21)$$

The comparison of the measured electron energy with $E_{\text{QEDC}}^{\text{DA}}$ tests the SpaCal energy scale linearity in the range 4 – 23 GeV.

For the QED Compton energy scale check, a bias free reconstruction of the electron and photon angles is essential. Therefore in addition to the basic QEDC event selection described in section 8.2.1, both electron and photon SpaCal clusters are required to be linked to BDC track segments. This implies that the photon converted in the detector material in front of the BDC. The electron cluster is identified by requiring a BST link. The photon cluster must have no associated signals, neither in the BST nor in the CIP.

The results of all calibration studies are summarised in figure 15. Both the J/ψ and the various QEDC energy scale determinations are inside the uncertainty band. The scattered electron energy distributions and the uncertainty bands attached to the simulated E'_e distributions in the kinematic peak region are shown in figure 16 for the NVX and the SVX analyses. The data are well described by the simulations.

8.2.3 Calibration of the Hadronic Energy Scale

The calibration of the calorimeters employed for the hadronic final state energy measurement is based on kinematic constraints relating the scattered electron to the hadronic final state. For the calibration of the LAr calorimeter, conservation of the total transverse momentum P_T is used. The SpaCal calibration makes use of the conservation of $E - P_z$.

Calibration of the LAr calorimeter. The hadronic final state in the central and forward regions of the H1 detector is reconstructed using a combination of tracks and LAr energy deposits (see section 6.4). The LAr calibration coefficients are determined for the eight calorimeter wheels, each subdivided into eight octants, separately for the hadronic and electromagnetic sections. There are thus 120 calibration constants in total⁶, corresponding to the calorimeter segmentation in rapidity, azimuthal angle, and depth. The same calibration procedure is applied to the data and the MC simulation.

To reduce the influence of the SpaCal on the calibration of the LAr, forward and central hadronic angles are selected: $13^\circ \leq \theta_h \leq 150^\circ$. The electron transverse momentum P_T^e is determined from the SpaCal energy and the θ_e measured by the BST. The photoproduction background is reduced to a negligible level by requiring $E_e' > 20$ GeV.

In the calibration procedure, a least squares minimisation of the following function is performed

$$\mathcal{L}(\alpha_j) = \sum \left(P_T^e - |\mathbf{P}_T^{\text{Tr}} + \mathbf{P}_T^{\text{Sp}} + \sum_j \alpha_j \mathbf{P}_T^j| \cdot |\cos(\phi_e - \phi_h)| \right)^2. \quad (22)$$

Here the transverse momenta \mathbf{P}_T^{Tr} and \mathbf{P}_T^{Sp} are the vector sums of the contributions from the tracks and the SpaCal, respectively, \mathbf{P}_T^j are the vector sums of the contributions from all cells of a calorimeter volume j , ϕ_h is the azimuthal direction of the hadronic final state and α_j are the calibration coefficients, which are free parameters. The outer summation is performed over all DIS events selected for the calibration.

The P_T balance between the scattered electron and the calibrated hadronic final state is studied as a function of various variables, such as P_T^e , θ_h and y_Σ . For central events, where $y_\Sigma \geq 10^{-2}$, the simulation reproduces the behaviour of the data within 2% accuracy. At lowest y , the hadronic final state is produced at small polar angles and partially escapes the LAr acceptance. In this case, simulation and data agree within 10%. The systematic uncertainty of the hadronic scale is therefore extrapolated linearly in $\log y$, from 10% at $y_\Sigma = 10^{-3}$ to 2% at $y_\Sigma = 10^{-2}$. It is then set to 2% for $y_\Sigma \geq 0.01$. Figure 17 shows the overall P_T balance for the standard analysis selection. The vertical line at $P_T^h/P_T^e = 0.3$ indicates the analysis cut value. An increase in number of events for $P_T^h/P_T^e < 0.3$ corresponds to very low $y < 0.001$. The data agree with the simulation within the hadronic energy scale uncertainty.

Hadronic Energy Calibration of the SpaCal. For large values of $y \gtrsim 0.4$, the contribution of the SpaCal to the total $E - P_z$ becomes larger than the combined contribution of the LAr calorimeter and tracks. Given the accurate knowledge of the SpaCal linearity after calibration (section 8.2.2), the study of $E - P_z$ as a function of E_e' allows a check of both the linearity and the absolute scale of the SpaCal hadronic measurement to be made.

The $E - P_z$ distribution is studied for $E_e' > 7$ GeV in E_e' intervals of 1 GeV. For each interval, a Kolmogorov-Smirnov test is performed to estimate a possible shift in the $E - P_z$ distribution between data and simulation. For the SVX analysis, the data and the simulation agree well within their statistical uncertainties, while for the NVX data sample a global shift of ~ 1 GeV is observed. This shift is applied in the NVX analysis to the simulated events. An additional systematic uncertainty, $\Delta(E - P_z)_{\text{SpaCal}} = 0.5$ GeV, is considered for both SVX and NVX analyses.

⁶The most backward LAr wheel does not have a hadronic section.

Figure 18 shows the $E-P_z$ distribution for the data and the simulation. The uncertainty band includes a ± 0.5 GeV variation of the SpaCal contribution to the total $E-P_z$.

8.2.4 Calorimeter Noise Uncertainty

For $y \lesssim 0.01$, even a small fake energy contribution in the LAr can strongly affect the determination of y_h . Therefore, a dedicated procedure is used to identify the LAr noise, as described in section 6.4. Samples of LAr electronic and beam induced noise are recorded in special runs and added to the simulation.

The uncertainty of the noise influence on the DIS cross section measurement is determined as a function of y_h by studying the ratio $y_{h,\text{noise}}/(y_h + y_{h,\text{noise}})$, where $y_{h,\text{noise}}$ is defined as $y_{h,\text{noise}} = \sum_i (E_i - P_{z,i})/2E_e$ with the sum extending over the identified noise cells only. This comparison is shown in figure 19 for the NVX and SVX data samples together with contributions to y_h from the tracks, LAr and SpaCal calorimeters. The noise fraction is described by the simulation within 10% accuracy which is taken as a systematic uncertainty. Note that at high y the noise fraction is small. More details on the LAr noise uncertainty estimation can be found in [82,83].

8.3 Background Subtraction

8.3.1 Methods

The dominant background source for this analysis arises from very low Q^2 photoproduction events in which the scattered electron escapes detection in the backward beam pipe and a particle from the hadronic final state mimics the electron. Other potential background sources arise from non- ep interactions. They are studied using non-colliding HERA bunches and are found to be negligible.

For a fraction of photoproduction events the scattered electron is detected by the electron tagger of the luminosity system. These events are used to study the photoproduction background. The acceptance of the electron tagger, which corresponds to the geometrical aperture of the detector as well as to the detection efficiency, is determined using Bethe-Heitler $ep \rightarrow e\gamma p$ events [40], in which the scattered electron and the emitted photon are detected in the electron and photon tagger, respectively, and is parametrised as a function of y . The acceptance is large in the range $0.3 < y < 0.6$.

The simulated photoproduction background (PHOJET) is normalised based on events where the scattered electron is detected by the electron tagger and all of the analysis selection criteria⁷ are satisfied. Two normalisation methods are used. In the first method the background is normalised globally and then subtracted bin-by-bin

$$N_{\gamma p}^i = N_{\text{bg MC}}^i \cdot \frac{N_{\text{tag}}}{N_{\text{bg MC, tag}}}, \quad N_{\text{DIS}}^i = N_{\text{data}}^i - N_{\gamma p}^i. \quad (23)$$

⁷For the electron method, this selection excludes the $E-P_z$ cut in order to increase the electron tagger acceptance. In addition, to reduce the influence of overlapping DIS and Bethe-Heitler events, the absence of energy deposits in the photon tagger is required, and the total $(E-P_z)_{\text{tot}} = E-P_z + 2E_{\text{tagger}}^e$, where E_{tagger}^e is the energy measured in the electron tagger, has to be less than 75 GeV.

Here, N_{DIS}^i ($N_{\gamma p}^i$) is the estimated number of DIS (photoproduction) events in the cross section measurement bin i , N_{data}^i and $N_{\text{bg MC}}^i$ are the numbers of data and PHOJET events in bin i , respectively, and $N_{\text{tag}}, N_{\text{bg MC, tag}}$ are the total numbers of events detected using the electron tagger in the data and the PHOJET simulation, respectively.

In the second method the background is normalised bin-wise using the bin-averaged tagger acceptance A_i and then subtracted in each bin

$$A_i = \frac{N_{\text{bg MC, tag}}^i}{N_{\text{bg MC}}^i}, \quad N_{\text{DIS}}^i = N_{\text{data}}^i - \frac{N_{\text{tag}}^i}{A_i}, \quad (24)$$

where N_{tag}^i and $N_{\text{bg MC, tag}}^i$ are the numbers of events detected by the electron tagger in bin i in the data and the PHOJET event sample, respectively. Both methods lead to a cancellation of global selection uncertainties, while the second method (equation 24) also allows local uncertainties to cancel at the expense of an increased statistical uncertainty.

For the NVX-S9 analysis, the global normalisation of the background (equation 23) is used, since for this sample the E'_e and θ_e distributions are well reproduced by the simulation (figure 20). Furthermore there is a direct control of the background normalisation as discussed in the next section. For the other analyses, a local bin-wise normalisation is performed. As a cross check, both normalisation methods are used for all samples, leading to cross section results consistent within statistical uncertainties.

8.3.2 Normalisation Uncertainty

The photoproduction background normalisation is checked for the NVX-S9 analysis using electron candidates associated with tracks of opposite charge to the lepton beam charge, termed “wrong charge” tracks. Assuming charge symmetry of the background tracks, the wrong charge track sample gives an estimate of the remaining background in the correct charge sample. The track charge can be measured for tracks which are reconstructed in the BST sector equipped with u strip detectors in addition to the r detectors.

In this method, any charge asymmetry creates a bias. In addition, the requirement of a u strip track in the background study could modify the normalisation compared to the standard sample. The geometrical acceptance and efficiency ϵ of the u strip track reconstruction are first determined based on a high E'_e sample in which the background can be neglected. The acceptance and efficiency are well described by the simulation. The acceptance difference between data and simulation is found to be $(2.0 \pm 1.3)\%$, while the efficiency difference is determined to be $(0.2 \pm 0.5)\%$.

All events within the u sector acceptance passing the NVX-S9 analysis cuts, N_{acc} , are classified according to $N_{\text{acc}} = N_0 + N_+ + N_-$, where N_0 denotes all events without a linked u track, N_+ is the number of all events with correct sign tracks (positive, as expected from the scattered positron) and N_- is the number of all events with wrong sign tracks. If $\kappa = N_+^{\text{bg}}/N_-^{\text{bg}}$ is the background charge asymmetry ratio, then the total number of background events in the u sector geometrical acceptance is

$$\begin{aligned} N_{\text{bg}} &= N_{\text{acc}} - N_{\text{sig}} = N_{\text{acc}} - \frac{N_+ - \kappa N_-}{\epsilon} = \\ &= N_0 + N_- \left(1 + \frac{\kappa}{\epsilon}\right) + N_+ \left(1 - \frac{1}{\epsilon}\right). \end{aligned} \quad (25)$$

Here $N_{\text{acc}}(N_{\text{sig}})$ denotes the number of accepted (genuine DIS signal) events.

The charge asymmetry of the background for the PHOJET simulation is found to be $\kappa = 0.79 \pm 0.06$. A dedicated study of the origin of this asymmetry [37] showed that the main effect is due to the difference between the proton and antiproton interaction cross sections and the visible energy which they deposit in the SpaCal. A larger value of $|E/p|$ is expected for antiprotons since they annihilate at the end of their paths. Indeed, for simulated events with $|E/p| > 2$ the deviation of κ from unity is larger: $\kappa = 0.60 \pm 0.14$. From the data with $|E/p| > 2$ a consistent value $\kappa = 0.65 \pm 0.12$ is measured⁸. The charge asymmetry is also checked using events in which the scattered electron is detected in the electron tagger. It is found to be 0.82 ± 0.17 . The PHOJET based asymmetry estimate is also consistent with the value estimated in [37] using tagged events, $\kappa = 0.91 \pm 0.04$. In order to cover the findings on the charge asymmetry explained above, a value $\kappa = 0.9 \pm 0.1$ is assumed for this analysis.

The ratio of the number of photoproduction events obtained using equation 25 to the estimated number of events based on the electron tagger, equation 23, for the E'_e range of the NVX-S9 analysis, is $r = 1.00 \pm 0.14_{\text{stat}} \pm 0.05_{\text{asym}}$. Here the first error gives the statistical uncertainty and the second error corresponds to the uncertainty in the background asymmetry determination. Figure 21 shows the distribution of E'_e for the background events, estimated using u sector tracks. The systematic uncertainty on the background normalisation is taken to be $\pm 15\%$, based on the statistical uncertainty of the u sector sample and the uncertainty in the background charge asymmetry.

8.4 Luminosity Determination

The luminosity measurement is based on Bethe-Heitler events detected using the photon detector. A precise luminosity measurement requires a good understanding of the beam optics, of the photon detector acceptance and its variation with changing beam conditions. The uncertainties related to the acceptance are similar for the NVX and the SVX data.

The time structure of the ep bunch crossings is characterised by the main proton bunch accompanied by satellite bunches. Two such bunches are at ± 4.8 ns away from the nominal bunch and lead to ep interactions at about ± 70 cm from the mean vertex position. The photon detector is sensitive in a time window of about 12 ns for Bethe-Heitler events and thus does not distinguish interactions at the nominal vertex position from satellite bunch interactions. The luminosity measurement therefore requires the fraction of satellite bunch interactions to be determined independently. This is possible in H1 using TOF and PPU systems.

For the SVX data, with the main bunch centred at $z = 70$ cm, the backward satellite is located at $z \sim 0$ cm. The backward satellite in this case gives a larger contribution to the luminosity measurement than the forward satellite at $z \sim 140$ cm. The fraction of events in the backward satellite can be determined directly from the fraction of DIS events with a reconstructed vertex around $z = 0$ cm and amounts to 2.7%. A 3% uncertainty is assigned to the luminosity measurement for the SVX data, which covers the differences observed between the methods of determining the satellite bunch fraction and also includes uncertainties related to the photon detector. The same procedure is performed to verify the contribution from the forward

⁸At low energy, the contribution of DIS electrons with $|E/p| > 2$ is negligible.

Correlated errors	
Source	Uncertainty
E'_e scale uncertainty	0.2% at 27.6 GeV to 1% at 2 GeV linear in E'_e
θ_e uncertainty	0.2 mrad (BST) 0.5 mrad (BDC-Central vertex)
LAr scale uncertainty	10% at $y = 0.001$ to 2% at $y = 0.01$ linear in $\log y$ 2% for $y > 0.01$
LAr noise contribution to $E-P_z$	10%
SpaCal hadronic scale	0.5 GeV
γp background normalisation	15%
Luminosity	3% (SVX) 1.1% (NVX)
Uncorrelated errors	
Source	Uncertainty
BST efficiency	2% (BST)
BDC efficiency	1.5% (BDC-Central vertex)
Central Tracker vertex efficiency	2 – 10% (BDC-Central vertex)
Trigger efficiency	0.9% (NVX) 1.1% (NVX-S9) 0.9% (SVX-BST) 0.7% (SVX-BDC)
Radiative corrections	0.5%

Table 4: Summary of the systematic uncertainties. For the correlated sources, the uncertainties are given in terms of the uncertainty of the corresponding source. The effect on the cross section measurement varies from bin to bin and is given in table 10-14. For the uncorrelated sources, the uncertainties are quoted in terms of the effect on the measured cross section directly and the type of analysis is given in brackets.

satellite at +70 cm of the NVX data sample. In this case the different methods are in agreement within 0.7%, leading to a total luminosity uncertainty of 1.1%.

In the course of this analysis an extended reanalysis of the 1997 data at $Q^2 \leq 12 \text{ GeV}^2$, this sample termed B in [37], was performed, which reproduced the published cross sections in shape. These, however, are to be multiplied by a factor of 1.034 as the result from an improved analysis of the satellite bunch structure and the photon detector acceptance. This corresponds to a shift of two standard deviations of the quoted luminosity measurement accuracy.

8.5 Summary of Systematic Uncertainties

The systematic uncertainties are classified into two groups, bin-to-bin correlated and uncorrelated systematic errors. For this analysis the correlated sources are the electromagnetic and hadronic energy scales, the electron scattering angle, the calorimeter noise, the background subtraction and the normalisation uncertainty. The uncorrelated errors are related to various efficiencies and radiative corrections. A summary of the correlated and uncorrelated errors for the present analysis is given in table 4.

The large overall contributions to the total error are due to the BST electron track reconstruction efficiency and the Central Tracker vertex efficiency uncertainty. The correlated error sources affect the DIS cross section measurement in a manner which depends on the kinematic domain. The most pronounced variation arises with the inelasticity y . For high y , the uncertainty is dominated by the photoproduction background (about 6% for $y = 0.8$). For intermediate $y \sim 0.1$, the E'_e scale uncertainty becomes more prominent for the electron method (about 3% cross section uncertainty). For $y < 0.01$, the dominant error source is the LAr noise (up to 10% cross section error).

8.6 Control Distributions

Data and Monte Carlo simulation distributions of important quantities for the events passing all selection criteria are compared in figures 22 - 25. Only events corresponding to analysis bins passing the stability and purity criteria are considered. The simulated distributions are normalised to the measured luminosity. The DIS MC cross section prediction is reweighted to a parameterisation using the fractal model introduced in section 11.1. A rather good (NVX) to acceptable (SVX) overall agreement is obtained in the description of the data by the simulation.

Figure 22a-d) shows basic kinematic and vertex distributions for the NVX analysis. The background from photoproduction events is very small. It is larger at lower scattered positron energies E'_e as can be seen in figures 22 e) and f), which show the E'_e and θ_e distributions for the dedicated high y analysis (NVX-S9). In figure 23 basic kinematic distributions for the SVX-BST analysis a)-c), the SVX-BDC analysis d) and the SVX-BST analysis considering events from ISR bins only e), f) are shown. The ISR distributions are very well reproduced by the simulation. The other SVX plots reveal a small normalisation difference. Figure 24 shows the x and Q^2 distributions for the two kinematic reconstruction methods, electron and Σ , in the NVX analysis. Figure 25 shows similar distributions for the SVX analysis. Events are only taken into account from bins which pass the stability and purity criteria and are covered by the chosen method. For the SVX sample the data are less well described than for the NVX sample, but consistency is observed within the total measurement uncertainty including a 3% normalisation error of the SVX data.

8.7 Cross Checks

The stability of the cross section measurement is tested with a set of dedicated cross checks which can be divided into three classes: (i) checks for a given data set and a given reconstruction method, (ii) checks of the consistency between the different reconstruction methods, and (iii) checks of the consistency between the different data sets.

The consistency of the cross section measurement for a given data set (e.g. NVX) and a given reconstruction method (e.g. the electron method with θ_e measured by the BST) is studied by splitting the data into two approximately equal sub-samples and comparing these sub-samples to each other. The data are compared as measured with the upper and the lower half of the SpaCal, for negative and positive z -vertex positions, and dividing the sample into an early and late data taking period. These tests are sensitive to local effects like efficiency variation, energy

miscalibrations and the stability of the luminosity measurement. In such studies no significant deficiencies in the data are observed.

For the comparison of the cross section measurements for a given data set but using different reconstruction methods, the test samples are strongly correlated. The uncorrelated statistical uncertainty is estimated in this case by subdividing the simulated events into a number of independent sub-samples of equal size. The measurement of the cross sections is repeated for each sub-sample and the statistical uncertainty is calculated as the luminosity rescaled RMS of the resulting variations of the cross section measurements. Employing this technique, the cross section measurements based on different triggers and different θ_e reconstruction methods (BDC and BST) are compared. In most of the cases the measurements with each of the samples agree within the uncorrelated statistical uncertainty. In a few cases the measurements agree within the total uncertainty only. A particularly interesting test is the comparison of the cross section measurement performed with the electron and sigma methods, since the two methods have different sensitivities to systematic error sources. The two methods can both be applied in many common bins where the purity and stability of the measurement are high for both methods. Figure 26 shows an example of this comparison, performed for the NVX-BST data set.

The third class of cross checks compares the cross section measurements performed with different data samples: SVX is compared to NVX and the new data are compared to the previously published results. This comparison is an integral part of the cross section averaging procedure, as discussed subsequently.

8.8 Cross Sections

The cross section data measured from the SVX and NVX data samples are given in tables 10-14 and presented in figure 27. The uncertainty of the new data is typically 3 – 4% and larger at the acceptance edges. Lowest values of Q^2 , down to 0.2 GeV^2 , are reached with the shifted vertex data. The analysis of the SVX data is mainly based on the BST but complemented by an independent analysis using the BDC at lower radii. For Q^2 between 0.5 and 3.5 GeV^2 , the NVX and SVX cross section data overlap in their kinematic coverage and are observed to be in agreement. The kinematic region of larger $Q^2 \geq 5 \text{ GeV}^2$ is covered by the nominal vertex data. The data at highest y , corresponding to smallest x , are obtained using the dedicated trigger S9 and can be seen in figure 27 to be consistent with the behaviour of σ_r towards small x .

9 Combination of H1 Cross Section Measurements

The new data cover a kinematic region which overlaps with data sets taken at 820 GeV proton beam energy in 1995 [35] and in 1997 (sample B) [37]. The combination of all these data, as described subsequently, provides a single data set in the range $0.2 \leq Q^2 \leq 12 \text{ GeV}^2$ and $5 \cdot 10^{-6} \leq x \leq 0.02$.

9.1 Procedure

The combination of the data sets is based on the prescription introduced in [87] which is applicable if the uncertainties of the measurements do not depend on the central values. This procedure is described in section 9.1.1. For the cross section measurements the estimated statistical and systematic uncertainties depend on the central values. This leads to a modification of the averaging procedure as is described in section 9.1.2.

9.1.1 Linear Averaging

The averaging procedure is based on a χ^2 minimisation. For a single data set, the χ^2 function can be defined as

$$\chi_{\text{exp}}^2(\mathbf{m}, \mathbf{a}) = \sum_i \frac{\left[m^i - \sum_j \frac{\partial \mu^i}{\partial \alpha_j} (a_j - \alpha_j) - \mu^i \right]^2}{\Delta_i^2} + \sum_j \frac{(a_j - \alpha_j)^2}{\Delta_{\alpha_j}^2}. \quad (26)$$

Here μ^i is the measured central value at a point i with combined statistical and uncorrelated systematic uncertainty $\Delta_i = (\Delta_{i,\text{stat}}^2 + \Delta_{i,\text{uncor}}^2)^{1/2}$. Further, α_j denotes the central value determined for a correlated systematic error source of type j with an uncertainty Δ_{α_j} , while $\partial \mu^i / \partial \alpha_j$ quantifies the sensitivity of the measurement μ^i at the point i to the systematic source j . The function χ_{exp}^2 depends on the set of underlying physical quantities m^i (denoted as the vector \mathbf{m}) and the set of systematic uncertainties a_j (\mathbf{a}). For the reduced cross section measurements one has $\mu^i = \sigma^i$, i denotes a (x, Q^2) interval, and the summation over j extends over all correlated systematic sources.

Introducing the variables $b_j = (a_j - \alpha_j) / \Delta_{\alpha_j}$ and $\Gamma_j^i = (\partial \mu^i / \partial \alpha_j) \Delta_{\alpha_j}$, equation 26 can be written as

$$\chi_{\text{exp}}^2(\mathbf{m}, \mathbf{b}) = \sum_i \frac{\left[m^i - \sum_j \Gamma_j^i b_j - \mu^i \right]^2}{\Delta_i^2} + \sum_j b_j^2. \quad (27)$$

If several analyses provide a number of measurements at the same (x, Q^2) values, they can be combined using the formula above, generalised for the case of multiple data sets. Then a total χ^2 function, χ_{tot}^2 , is built from the sum of the χ_{exp}^2 functions for each data set according to

$$\chi_{\text{tot}}^2(\mathbf{m}, \mathbf{b}) = \sum_e \sum_{i=1}^{N_M} \frac{\left[m^i - \sum_{j=1}^{N_S} \Gamma_{j,e}^i b_j - \mu_e^i \right]^2}{\Delta_{i,e}^2} w_{i,e} + \sum_{j=1}^{N_S} b_j^2, \quad (28)$$

where the summation over i (j) runs over all N_M measured points (all N_S systematic error sources) of all data sets considered. The symbol $w_{i,e}$ is equal to one if data set e contributes a measurement at the point i , otherwise it is zero. Similarly, the symbol $\Gamma_{j,e}^i$ equals to zero if the measurement i from the data set e is insensitive to the systematic source j . This definition of χ_{tot}^2 assumes that the data sets e are statistically uncorrelated. The systematic error sources b_j , however, may be either uncorrelated (separate sources) or correlated across data sets (different data sets sharing a common source).

Since χ_{tot}^2 is a quadratic form of \mathbf{m} and \mathbf{b} , it may be rearranged such that it takes a form similar to equation 26

$$\chi_{\text{tot}}^2(\mathbf{m}, \mathbf{a}) \equiv \chi_{\text{min}}^2 + \sum_{i=1}^{N_M} \frac{\left[m^i - \sum_j \frac{\partial \mu^{i,\text{ave}}}{\partial \alpha_j} (a_j - \alpha_{j,\text{ave}}) - \mu^{i,\text{ave}} \right]^2}{\Delta_{i,\text{ave}}^2} + \sum_{j=1}^{N_S} \sum_{k=1}^{N_S} (a_j - \alpha_{j,\text{ave}})(a_k - \alpha_{k,\text{ave}})(A'_S)_{jk}. \quad (29)$$

The data averaging procedure, described in detail in appendix A, determines the average values $\mu^{i,\text{ave}}$, the uncorrelated uncertainties $\Delta_{i,\text{ave}}$, the average systematic error source values $\alpha_{j,\text{ave}}$, the dependencies of $\mu^{i,\text{ave}}$ on α_j , $\partial \mu^{i,\text{ave}} / \partial \alpha_j$, and the matrix $(A'_S)_{jk}$. The value of χ_{min}^2 corresponds to the minimum of equation 28. The ratio $\chi_{\text{min}}^2 / n_{\text{dof}}$ is a measure of the consistency of the data sets. The number of degrees of freedom, n_{dof} , is calculated as the difference between the total number of measurements and the number of the measured points N_M . This procedure represents a method to average data sets, which allows correlations among the measurements due to systematic uncertainties to be taken into account.

The matrix $(A'_S)_{jk}$ can be diagonalised and the χ^2 function takes a form similar to equation 27

$$\chi_{\text{tot}}^2(\mathbf{m}, \mathbf{b}') = \chi_{\text{min}}^2 + \sum_{i=1}^{N_M} \frac{\left[m^i - \sum_{j=1}^{N_S} \Gamma_j^{i,\text{ave}} b'_j - \mu^{i,\text{ave}} \right]^2}{\Delta_{i,\text{ave}}^2} + \sum_{j=1}^{N_S} (b'_j)^2, \quad (30)$$

where $b'_j = \sum_k U_{jk}(b_k - \beta_{k,\text{ave}})D_{jj}$ and $\beta_{k,\text{ave}} = \alpha_{k,\text{ave}} / \Delta_{\alpha_k}$. The orthogonal matrix U connecting the systematic sources before and after averaging and the diagonal matrix D are given in appendix A.

9.1.2 Implementation for the Cross Section Averaging

The χ^2 function of equation 26 is suitable for measurements in which the uncertainties are absolute, i.e. do not depend on the central value of the measurement. However, for the H1 cross section data considered here, the correlated and uncorrelated systematic errors are to a good approximation proportional to the central values (multiplicative errors), whereas the statistical errors scale with the square roots of the expected number of events. In this case the combination of the data sets using equation 26 leads to a small bias to lower cross section values since the measurements with lower central values have smaller absolute uncertainties. To take this effect into account, the χ^2 definition is modified to

$$\chi_{\text{exp}}^2(\mathbf{m}, \mathbf{b}) = \sum_i \frac{\left[m^i - \sum_j \gamma_j^i m^i b_j - \mu^i \right]^2}{\delta_{i,\text{stat}}^2 \mu^i \left(m^i - \sum_j \gamma_j^i m^i b_j \right) + \left(\delta_{i,\text{uncor}} m^i \right)^2} + \sum_j b_j^2. \quad (31)$$

Here $\gamma_j^i = \Gamma_j^i / \mu^i$, $\delta_{i,\text{stat}} = \Delta_{i,\text{stat}} / \mu^i$ and $\delta_{i,\text{uncor}} = \Delta_{i,\text{uncor}} / \mu^i$ are relative correlated systematic, statistical and uncorrelated systematic uncertainty, respectively. This χ^2 definition is used for the averaging procedure and also for the phenomenological analysis of the data (see section 10). Equation 31 is equivalent to the one used in previous H1 analyses [37] up to modifications in the

denominator. In contrast to equation 27, the χ^2 function of equation 31 is not a simple quadratic form with respect to m^i and b_j . The average is found in an iterative procedure: first equation 27 is used to get an initial approximation for $\mu^{i,\text{ave}}$ and $\beta_{j,\text{ave}}$ which are used to recalculate the errors as $\Gamma_j^i = \gamma_j^i \mu^{i,\text{ave}}$ and $\Delta_i^2 = \delta_{i,\text{stat}}^2 (\mu^{i,\text{ave}} - \sum_j \gamma_j^i \mu^{i,\text{ave}} \beta_{j,\text{ave}}) + (\delta_{i,\text{uncor}} \mu^{i,\text{ave}})^2$. Then the determination of $\mu^{i,\text{ave}}$ is repeated. Convergence is observed after two iterations.

For measurements with multiplicative errors the geometric mean instead of the arithmetic mean can be used as an alternative, i.e. the average is performed for $\ln \sigma_r^i$. In this case the quadratic equation 27 can be used by replacing $\mu^i \rightarrow \ln \sigma_r^i$, $\Delta_i \rightarrow (\delta_{i,\text{stat}}^2 + \delta_{i,\text{uncor}}^2)^{1/2}$ and $\Gamma_j^i \rightarrow \gamma_j^i$. This logarithmic averaging procedure is used as a cross check.

For the NVX and SVX analyses, the measured cross section values σ_r^i , the statistical and uncorrelated uncertainties $\delta_{i,\text{stat}}$, $\delta_{i,\text{uncor}}$ and all correlated systematic uncertainties γ_j^i as well as the total error $\delta_{i,\text{tot}} = [\delta_{i,\text{stat}}^2 + \delta_{i,\text{uncor}}^2 + \sum_j (\gamma_j^i)^2]^{1/2}$ are given in tables 10-14. The average of the H1 data is reported in tables 15-20, where the average reduced cross sections $\sigma_r^{i,\text{ave}} = \mu^{i,\text{ave}}$, the statistical $\delta_{i,\text{ave,stat}}$, uncorrelated $\delta_{i,\text{ave,uncor}}$, correlated $\gamma_j^{i,\text{ave}}$ and total $\delta_{i,\text{ave,tot}} = [\delta_{i,\text{ave,stat}}^2 + \delta_{i,\text{ave,uncor}}^2 + \sum_j (\gamma_j^{i,\text{ave}})^2]^{1/2}$ uncertainties are given. The transformation matrix U is given in table 21. The shifts of the central values of the systematic error sources, in units of the systematic errors $\alpha_{j,\text{ave}}/\Delta_{\alpha j}$, are given in table 5.

9.2 Compatibility of SVX and NVX Data

The combination of the SVX and NVX data depends upon assumptions on the correlation between different data points, within a data set as well as across the data sets. For each data set, two types of systematic uncertainty are considered: fully correlated ones, which are treated as α_j in equation 31, and fully uncorrelated ones, which are added to the statistical uncertainties in quadrature and treated as δ_i in equation 31. Following the notation in table 4, the six sources of correlated uncertainties are E_e' scale, θ_e , LAr hadronic energy scale, LAr noise, SpaCal hadronic scale and photoproduction background. A further correlated uncertainty arises from the luminosity measurements. Concerning the relation between data sets, the systematic uncertainty of the luminosity measurement is separated into a 0.5% fully correlated theoretical uncertainty and an uncorrelated experimental part due to variations of beam and detector acceptance conditions. The other systematic uncertainties are considered to be uncorrelated.

The systematic uncertainties which are correlated between data points can be assumed as either fully correlated, uncorrelated or partially correlated between the NVX and the SVX data. The reasons for correlations between data sets are the similarity in the calibration procedure and the detector setup. Uncorrelated effects arise from variations with time, differences between the kinematic ranges of the calibration samples, the dead material, the detector illumination or the acceptance. For each source the uncorrelated part is more important and thus all sources are considered to be uncorrelated between the NVX and the SVX data.

To check the sensitivity of the averaged result to the correlation assumptions, the average of the NVX and SVX data, obtained by considering the six systematic sources to be uncorrelated, is compared to $2^6 - 1$ other possible assumptions in which each source is either fully correlated or fully uncorrelated. Most of the cases lead to numerically small variations for both the central values and the total errors of the average data. The only significant variation is observed for

the lowest y points for $Q^2 > 2 \text{ GeV}^2$, if the LAr noise is assumed to be correlated between the NVX and SVX data. Since the LAr noise, however, is a time dependent uncorrelated source, no additional systematic uncertainty is assigned to the combined measurement.

The NVX and SVX data sets are fully consistent, according to the averaging procedure, with $\chi^2_{\text{min}}/n_{\text{dof}} = 19.5/39$. The shifts of the central values of the systematic uncertainties do not exceed one standard deviation.

9.3 Global Combination of Low Q^2 H1 Data

The new data given in tables 10-14 are combined with the previously published H1 data obtained for a similar kinematic region. The comparison of the present cross section data, obtained by averaging the SVX and the NVX data, with the published cross section data, is given in figure 28. The new data are in agreement with the published NVX97 data [37] taking the +3.4% normalisation shift of the published data (section 8.4) into account. The data are also consistent with the SVX95 data [35] within their rather large uncertainties. For the combination of all data, the systematic uncertainties are considered to be uncorrelated across the data sets.

The published H1 data [35,37] were taken with a proton beam energy of $E_p = 820 \text{ GeV}$. Therefore a centre-of-mass energy (CME) correction, based on equation 1, is applied when comparing to the previously published cross section according to

$$\sigma_r^{920}(x, Q^2) = \sigma_r^{820}(x, Q^2) + F_L^{\text{th}}(x, Q^2) [f(y_{820}) - f(y_{920})]. \quad (32)$$

Here $\sigma_r^{920}(x, Q^2)$ is the reduced cross section rescaled to $E_p = 920 \text{ GeV}$; $\sigma_r^{820}(x, Q^2)$ is the measured reduced cross section for $E_p = 820 \text{ GeV}$; y_{820} and y_{920} are the inelasticities for the two proton beam energies calculated as $y = Q^2/4E_e E_p x$, and $F_L^{\text{th}}(x, Q^2)$ is calculated using the fractal model for $F_2(x, Q^2)$ and $R = 0.5$. This correction becomes large only at high y . To avoid any sizeable effect of the energy dependence of σ_r on the combination of the 820 and 920 GeV data, the combination of the points at the same (x, Q^2) is restricted to a region of $y_{820} < 0.35$. At higher y the measurements are kept separately but they are affected by the combination procedure. The residual dependence on the F_L assumption for the average points is negligible. For illustrative purposes, the CME correction is applied to all 820 GeV data points in figures 28-32.

The H1 data sets are consistent with each other. If all samples are averaged in a single step one obtains $\chi^2_{\text{tot}}/n_{\text{dof}} = 86.2/125$. Shifts of the central values of the systematic sources $\alpha_j/\Delta\alpha_j$ are given in table 5. The systematic shifts imposed by the averaging procedure are mostly within one standard deviation. The most noticeable effects are a downward shift of the normalisation of the SVX95 data and a modification of the LAr hadronic energy scale of the SVX data which corresponds to a small adjustment of the SVX data at large x .

The combination of the H1 data using the χ^2 definition of equation 31 has been compared to that using the χ^2 definition of equation 27 and also using the logarithmic averaging procedure. For the bulk of the phase space, the definition of equation 27 would lead to a change of typically -0.7% , which increases to -2.0% for the data at $Q^2 \leq 0.5 \text{ GeV}^2$. For the logarithmic average the difference compared to equation 31 is typically below 0.1% .

Systematic Source	Shift in σ			
	SVX95	NVX97	NVX	SVX
E'_e scale	0.03	1.19	-0.32	0.36
θ_e	0.20	-0.72	1.03	0.48
LAr scale	-0.09	0.06	-0.23	-1.79
LAr noise	—	-1.06	-0.20	-1.13
SpaCal hadronic scale	—	—	0.48	-1.66
γp background	0.48	-0.10	0.05	0.10
Luminosity	-1.60	0.66	0.10	0.17

Table 5: Shifts of the central values of the systematic uncertainties $\alpha_{j,\text{ave}}/\delta\alpha_j$ based on the average of the published $E_p = 820$ GeV and the new NVX-SVX data. For example, the quoted value for the luminosity shift of the SVX95 sample, -1.60 , corresponds to a $-1.60 \times 3\% = 4.80\%$ downward shift of the SVX95 cross section values.

9.4 Combined Cross Section Results

The combined low Q^2 data and the resulting uncertainties are listed in tables 15-20 and shown in figures 28-32. There are 149 data points. The total uncertainty in the central Q^2, x region of this measurement is about 2% but it becomes larger towards the edges of the covered phase space. At high y , for example, the measurement at a Q^2 value of a few GeV^2 has an uncertainty of about 5%.

Figures 29 and 30 show the combined H1 reduced ep cross section measurement and different phenomenological descriptions as introduced below. For all Q^2 bins, starting at large x the reduced cross section first increases for $x \rightarrow 0$. For $Q^2 \geq 0.6 \text{ GeV}^2$ there is a characteristic turn over of the cross section observed at the smallest x values. This region, for each Q^2 , corresponds to highest inelasticity, $y = Q^2/(sx)$, and thus the turn over at $y \approx 0.6$ can be attributed to the influence of the longitudinal structure function F_L .

For $y < 0.6$ the influence of the longitudinal structure function is small and thus one can extract the structure function F_2 with only a small residual dependence on the assumption on F_L . Using $R = 0.5$, F_2 is extracted and shown in figure 31. The structure function F_2 exhibits a steady increase as $x \rightarrow 0$ for all Q^2 bins.

Figure 32 shows the measurement of the virtual photon-proton effective cross section $\sigma_{\gamma^*p}^{\text{eff}}$ as a function of Q^2 at various values of W . The H1 data are compared to the data of ZEUS [38, 39] and to different models, as discussed below. A good agreement between the data sets is observed. The H1 data extend the HERA measurements to higher and lower W and also cover the $Q^2 \sim 1 \text{ GeV}^2$ region.

10 Cross Section Analysis

10.1 Rise of F_2 at Low x and Extraction of R

The rise of the structure function F_2 towards low x has previously been described by a power law in x , $F_2 = c(Q^2)x^{-\lambda(Q^2)}$, where the exponent λ increases approximately logarithmically with

$\ln Q^2$ for $Q^2 \gtrsim 2 \text{ GeV}^2$ [88]. This simple parametrisation has been shown to model the ep data well for $x < 0.01$.

This idea can be extended to fit the reduced cross section σ_r in order simultaneously to extract the exponent λ and to estimate the longitudinal structure function F_L . The measured ep cross section is sensitive to the longitudinal structure function F_L only for large $y \gtrsim 0.5$, a region which corresponds to a limited x range for a given Q^2 value. Gluon dominance at low x suggests that the function F_L may exhibit an x dependence similar to F_2 . In the subsequent studies using this ansatz it is assumed that F_L is proportional to F_2 and that the coefficient of proportionality depends only on Q^2 . For the extraction of F_L , the ratio of $\sigma_L/\sigma_T = R$ is used such that

$$F_L(Q^2, x) = F_2(Q^2, x) \frac{R(Q^2)}{1 + R(Q^2)}. \quad (33)$$

and

$$\sigma_r(Q^2, x) = c(Q^2) x^{-\lambda(Q^2)} \left[1 - f(y) \frac{R(Q^2)}{1 + R(Q^2)} \right]. \quad (34)$$

The combined 1995-2000 H1 low Q^2 data are fitted following equation 34 for each Q^2 bin. These fits describe the data very well, as is illustrated in figure 29. The results of these fits are shown in figures 33 and 34. The fit results for $\lambda(Q^2)$ are given in table 6. One can see in figure 33b) that the parameter λ shows an approximately linear increase as a function of $\ln Q^2$ for $Q^2 > 2 \text{ GeV}^2$ as has been observed previously [88]. For lower Q^2 the variation of λ is diminished but relatively large uncertainties prevent definite conclusions. The normalisation coefficient $c(Q^2)$ rises with increasing Q^2 for $Q^2 < 2 \text{ GeV}^2$ and is consistent with a constant behaviour in the DIS region, as in [88].

The values of the coefficient $R(Q^2)$ are consistent with no dependence on Q^2 . The mean R is 0.55 ± 0.05 with ⁹ $\chi^2/n_{\text{dof}} = 7.9/(8-1)$. While the experimental error is small there is a very strong model dependence, different parameterisations for F_2 leading to significant changes in F_L , see section 11. The value of the average R obtained in this model is consistent within about one standard deviation with $R = 0.5$ or $\sigma_L = \frac{1}{2}\sigma_T$. This value of R leads to an F_L which is higher than the first direct measurement of F_L at low x performed by the H1 collaboration [89]. The data in [89] correspond however to higher Q^2 values ($\geq 12 \text{ GeV}^2$).

10.2 Determination of F_L using the y Dependence of the Cross Section

The turn-over of the measured DIS cross section for the highest y values, apparent in figure 29, can be used for an extraction of the longitudinal structure function F_L using the so-called derivative method [37]. The derivative of the reduced cross section with respect to $\ln y$ is

$$\left. \frac{d\sigma_r}{d \ln y} \right|_{Q^2=\text{const}} = -\frac{dF_2}{d \ln x} - \frac{2y^2(2-y)}{(1+(1-y)^2)^2} F_L - \frac{y^2}{1+(1-y)^2} \frac{dF_L}{d \ln x}. \quad (35)$$

At high y for a wide variety of models the term proportional to F_L becomes numerically larger than other contributions. Therefore the extraction of the derivative provides means for determining F_L at low x and Q^2 with little phenomenological assumptions.

⁹For the determination of the mean, R values from different Q^2 bins are assumed to be uncorrelated and total errors are used.

Q^2/GeV^2	λ	$\delta_{\lambda,\text{stat}}$	$\delta_{\lambda,\text{uncor}}$	$\delta_{\lambda,\text{cor}}$	$\delta_{\lambda,\text{tot}}$
0.35	0.129	0.029	0.026	0.024	0.046
0.50	0.192	0.022	0.016	0.012	0.030
0.65	0.157	0.010	0.011	0.006	0.016
0.85	0.149	0.009	0.009	0.005	0.014
1.20	0.177	0.007	0.007	0.005	0.011
1.50	0.158	0.004	0.006	0.004	0.008
2.00	0.171	0.003	0.005	0.004	0.007
2.50	0.166	0.002	0.005	0.003	0.006
3.50	0.177	0.002	0.003	0.002	0.004
5.00	0.198	0.003	0.004	0.002	0.005
6.50	0.205	0.003	0.005	0.003	0.007
8.50	0.216	0.003	0.005	0.003	0.007

Table 6: Results of the fit (equation 34) to the combined H1 low Q^2 data on the exponent λ with the statistical $\delta_{\lambda,\text{stat}}$, uncorrelated systematic $\delta_{\lambda,\text{uncor}}$, correlated systematic $\delta_{\lambda,\text{cor}}$, and total uncertainties $\delta_{\lambda,\text{tot}}$.

Experimentally, $d\sigma_r/d\ln y$ is approximated by $y_{\text{av}}\Delta\sigma_r/\Delta y$, which is calculated for each pair of cross section measurements in neighbouring bins. Here Δy is determined using bin centre values, and y_{av} is the logarithmic average value. Only the $E_p = 920$ GeV data are used in this determination. The H1 data are illustrated in figure 35 and are compared to the fractal and dipole models discussed below in sections 11.1 and 11.2. Similar analysis using the $E_p = 820$ GeV data was presented in [37]. The systematic uncertainties are evaluated by changing the cross sections for each source of systematic uncertainty and repeating the calculation of the cross section difference. For the model predictions, $\Delta\sigma_r/\Delta y$ is calculated in an analogous way and using the same binning as for the data.

For the extraction of the structure function F_L , the fractal fit, introduced in section 11.1, is used to estimate the $dF_2/d\ln x$ contribution to $\Delta\sigma_r/\Delta y$, and also for the bin centre correction. To reduce the dependence on F_2 , only $\Delta\sigma_r/\Delta y$ value corresponding to $y = 0.735$ are used to determine F_L .

The resulting longitudinal structure function values are shown in figure 36. The derivative method is only weakly dependent on the model assumptions. There are however large experimental uncertainties, mostly due to statistics and the photoproduction background at large y . The F_L data are consistent with a constant $R = 0.5$, as introduced above, and also with smaller values on R , as obtained in the dipole models. The dependence of the measurement on the assumption made for F_2 is estimated by a comparison with results obtained when assuming F_2 to be independent of x . The difference between the extracted F_L values is shown as the band at the bottom of figure 36.

11 Model Comparisons

In the following the combined data are analysed in the context of the fractal model [33] and two versions of the colour dipole model [42,45], which unlike pQCD may be applied to describe the

Parameter	Value	Uncertainty
D_0 (GeV ⁻²)	0.75	0.03
D_1	0.052	0.002
D_3	-1.16	0.03
Q_0^2 (GeV ²)	0.093	0.010
R	0.56	0.07

Table 7: Parameters of the fractal fit and their total uncertainties. For the central fit D_2 is kept constant: $D_2 = 1.08$. If the parameter D_2 is floated, the fit gives $D_2 = 1.061 \pm 0.012$.

transition region from photoproduction to deep inelastic scattering. Fits are performed using equation 31.

11.1 Fractal Fit

In the fractal ansatz [33], the proton structure function F_2 is parameterised using five parameters Q_0 and D_0 to D_3 as

$$F_2(Q^2, x) = D_0 Q_0^2 \left(1 + \frac{Q_0^2}{Q^2}\right)^{1-D_2} \frac{x^{-D_2+1}}{1 + D_3 - D_1 \ln x} \left(x^{-D_1 \ln \left[1 + \frac{Q_0^2}{Q^2}\right]} \left(1 + \frac{Q^2}{Q_0^2}\right)^{D_3+1} - 1 \right). \quad (36)$$

The parameters of this model are determined with a fit to the cross section data, except for the parameter D_2 , which governs the structure function behaviour for the photoproduction regime and is fixed to $D_2 = 1.08$. This parameterisation is used in the Monte Carlo reweighting procedure. The fractal model [33] does not provide predictions for F_L . The same prescription is followed as for the λ parameterisation fit described in section 10.1 taking the F_L contribution to be proportional to F_2 .

The values of R are found to be consistent with the λ fit and with being independent of Q^2 . Thus for the fractal parameterisation of the reduced cross section, R is taken to be a constant, which results in the simple five parameter representation used in the present analysis. The parameters of the fit are given in table 7. The fit describes the data well with $\chi^2/n_{\text{dof}} = 155.3/(149 - 5)$. Similarly to the λ fit, the value of $R = 0.56 \pm 0.07$ is consistent within about one standard deviation with $R = 0.5$. This agreement with the λ fit may be attributed to the structure function F_2 having a power law-like x dependence.

11.2 Dipole Model Fits

In the GBW model [42] the dipole-proton cross section $\hat{\sigma}$ (see section 3) is given by

$$\hat{\sigma}(x, r) = \sigma_0 \left\{ 1 - \exp \left[-r^2 / \left(4r_0^2(x) \right) \right] \right\}, \quad (37)$$

where r corresponds to the transverse separation between the quark and the antiquark, and r_0^2 is an x dependent scale parameter, assumed to have the form

$$r_0^2(x) \sim (x/x_0)^\lambda. \quad (38)$$

Parameter	Value	Uncertainty
σ_0 (mb)	24.5	0.5
λ	0.256	0.003
x_0	0.60×10^{-4}	0.03×10^{-4}

Table 8: Parameters of the GBW dipole fit and their total uncertainties.

Parameter	Value	Uncertainty
R_{IIM} (fm)	0.605	0.008
λ	0.260	0.003
x_0	0.45×10^{-4}	0.03×10^{-4}

Table 9: Parameters of the IIM dipole fit with $N_0 = 0.7$ and their total uncertainties.

For small $r \ll r_0$, $\hat{\sigma}$ is proportional to r^2 (colour transparency, $\hat{\sigma} \sim (r/2r_0)^2$) while for $r \gg r_0$ the cross section approaches a constant value (saturation, $\hat{\sigma} \simeq \sigma_0$). The boundary in the (x, Q^2) plane which separates these regions is described by the “critical line” at the x dependent saturation scale $Q_s^2(x) = 1/r_0^2(x)$. The model provides predictions for both σ_T and σ_L in terms of only three parameters, σ_0 , x_0 and λ .

The fit to the reduced cross section with the dipole model of GBW (“GBW fit”) yields a $\chi^2/n_{\text{dof}} = 183.1/(149 - 3)$, acceptable but worse than that for the fractal model. It has been suggested that improved models of $\hat{\sigma}$ lead to a better description of the data and a variety of models has been developed. As an example, a fit using $\hat{\sigma}$ as proposed in the IIM model, with $N_0 = 0.7$ as defined in [45], has been performed. This fit also has three free parameters and gives $\chi^2/n_{\text{dof}} = 178.2/(149 - 3)$. The results of the two dipole model fits are shown in figures 30-32 and 35-36. The dipole model fit parameters are given in tables 8 and 9.

To trace the origin of the χ^2 differences between the models, predictions for the structure functions F_2 and F_L are compared individually. As an example, figure 37 shows the comparison between the three models for the bin $Q^2 = 1.2 \text{ GeV}^2$. The structure functions F_2 agree rather well for the models considered for $x > x_s = 0.18 \times 10^{-4}$, where x_s corresponds to the saturation radius of the GBW dipole model at the chosen Q^2 value. However, for $x < x_s$ the dipole models show a softer F_2 dependence on x . This holds in particular for the IIM dipole model. The main difference between the models is in the structure function F_L . As shown in figure 37, the predictions of the dipole models are nearly half of the result for F_L obtained with the fractal model analysis.

The strict correlation between F_L and F_2 predicted by the dipole models could be broken by higher twist effects [90]. To quantify the influence of the structure function F_L another fit to the reduced cross section data is performed, in which the F_L prediction of the dipole model is scaled with an additional free parameter B_L

$$F_L(x, Q^2) = F_L^{\text{dipole}}(x, Q^2) (1 + B_L) . \quad (39)$$

With B_L as a formal free parameter the GBW fit returns B_L deviating from 0 by more than 3 standard deviations, $B_L = 0.54 \pm 0.15$. The fit for the IIM model does not yield a significant change for the F_L prediction: $B_L = 0.15 \pm 0.14$.

To summarise, a steeper rise to smaller x of the structure function F_2 , together with a larger R value as obtained in the fractal model fit with constant R , gives the best description of the H1 data. However, a sufficiently softer rise of F_2 together with a smaller F_L , as predicted by the IIM model, also describes the data well. For the GBW model, the rise of F_2 is rather steep such that the fit to the data prefers a larger F_L , which is inconsistent with the prediction of the model.

12 Summary

A new measurement is performed of the inclusive double differential cross section for neutral current deep inelastic positron-proton scattering, $e^+p \rightarrow e^+X$, in the region of small Bjorken x and low absolute momentum transfers squared, Q^2 . The data were obtained with the H1 detector at the ep collider HERA in two dedicated periods of data taking at beam energies $E_e = 27.5$ GeV and $E_p = 920$ GeV. In the year 1999, events were collected with a dedicated trigger on low Q^2 DIS events at the nominal interaction vertex position, corresponding to an integrated luminosity of 2.1 pb^{-1} . In the year 2000, the interaction vertex was shifted forward by +70 cm in proton beam direction to access even smaller values of Q^2 , and data with an integrated luminosity of 0.505 pb^{-1} was taken.

The measurement is performed in a wide range of inelasticity y , from 0.0015 to 0.8, and of Bjorken x , from $5 \cdot 10^{-6}$ to 0.02. The data cover a Q^2 range from 0.2 to 12 GeV^2 , with an overlap region of the nominal and the shifted vertex data of $0.5 \leq Q^2 \leq 3.5 \text{ GeV}^2$, in which both measurements agree. At low Q^2 the data analysed here comprise the full statistics collected with the H1 experiment at 920 GeV.

The measurement obtained with the 1999 and the 2000 data is combined with data collected in the years 1995 and 1997, which were taken at 820 GeV proton beam energy in similar experimental conditions and published previously. This combination takes the correlation of systematic uncertainties into account and provides a new, single data set from the H1 experiment, which supersedes all H1 data previously released in that kinematic region. The total uncertainty of the final reduced cross section measurement is about 2% for a large part of the phase space.

The neutral current ep cross section at low Q^2 is governed by two independent proton structure functions, F_2 and F_L . For $y < 0.6$, the influence of the longitudinal structure function F_L is small, and the data in this range are also presented as a measurement of the proton structure function $F_2(x, Q^2)$. For $y = 0.735$, using a method based on the derivative of the cross section with respect to $\ln y$, the structure function $F_L(x, Q^2)$ is extracted with minimum assumptions on the behaviour of F_2 .

In each Q^2 bin a simple parameterisation of the reduced cross section in terms of a power law of $F_2(x, Q^2) \propto x^{-\lambda}$ and $R = F_L/(F_2 - F_L)$ describes the data well. The power λ increases approximately logarithmically with Q^2 at $Q^2 \gtrsim 2 \text{ GeV}^2$. The parameterisation is consistent with a constant value of $R(x, Q^2) \simeq 0.5$, which implies that $F_L(x, Q^2) \simeq F_2(x, Q^2)/3$ under the assumption of a power law rise of F_2 towards low x .

The transition region of DIS to photoproduction, $Q^2 \simeq 1 \text{ GeV}^2$, cannot be analysed within perturbative QCD. The data therefore are studied here within phenomenological models. The

structure function $F_2(x, Q^2)$ is analysed using a self similarity based ansatz within a fractal model. The fractal F_2 parameterisation, combined with a constant R , provides a good description of the measured cross section in the full range of phase space covered by the data.

The Colour Dipole Model predicts both structure functions F_2 and F_L using a single characteristic dipole scattering cross section. Two versions of the CDM, the GBW model and the IIM model, are used in this analysis and are found to generally describe the cross section data well. The description of the data in the GBW model is observed to improve when the contribution of F_L within this model is formally allowed to be enhanced. The IIM model prediction on F_L is similar to the GBW model. Owing to a softer rise of F_2 towards small x , the IIM ansatz yet is able to describe the cross section data better and no modification on the predicted F_L is suggested by the data.

For the region $Q^2 \simeq 1 \text{ GeV}^2$, in which the transition from photoproduction to DIS takes place, the data as presented in this paper are the most precise result of the H1 Collaboration.

Acknowledgements

We are grateful to the HERA machine group whose outstanding efforts have made this experiment possible. We thank the engineers and technicians for their work in constructing and maintaining the H1 detector, our funding agencies for financial support, the DESY technical staff for continual assistance and the DESY directorate for support and for the hospitality which they extend to the non DESY members of the collaboration.

A Averaging Procedure

The χ^2 function of equation 28 is to be minimised with respect to the sets m^i and b_j . This determines the averaged measurements and uncertainties, $\mu^{i,\text{ave}}$, $\Delta_{i,\text{ave}}$, $\alpha_{j,\text{ave}}$ and the matrix A'_S , used in equation 29.

The minimum χ^2_{\min} in equation 28 is found by solving a system of linear equations obtained by requiring $\partial\chi^2/\partial m^i = 0$ and $\partial\chi^2/\partial b_j = 0$ which can be written in matrix form

$$\begin{pmatrix} A_M & A_{SM} \\ (A_{SM})^T & A_S \end{pmatrix} \cdot \begin{pmatrix} M^{\text{ave}} \\ B^{\text{ave}} \end{pmatrix} = \begin{pmatrix} C_M \\ C_S \end{pmatrix}. \quad (40)$$

Here the vector M^{ave} corresponds to all measurements and the vector B^{ave} corresponds to all systematic error sources. The matrix A_M has a diagonal structure with N_M diagonal elements

$$A_M^{ii} = \sum_e \frac{w_{i,e}}{\Delta_{i,e}^2}. \quad (41)$$

The other matrices have the following elements

$$\begin{aligned} A_{SM}^{ij} &= -\sum_e \frac{\Gamma_{j,e}^i}{\Delta_{i,e}^2} w_{i,e}; \\ A_S^{ij} &= \delta_{ij} + \sum_e \sum_k^{N_M} \frac{\Gamma_{i,e}^k \Gamma_{j,e}^k}{\Delta_{k,e}^2} w_{k,e}; \\ C_M^i &= \sum_e \frac{\mu_e^i}{\Delta_{i,e}^2} w_{i,e}; \\ C_S^j &= -\sum_e \sum_k^{N_M} \frac{\mu_e^k \Gamma_{j,e}^k}{\Delta_{k,e}^2} w_{k,e}. \end{aligned} \quad (42)$$

Here δ_{ij} is the standard Kronecker symbol. Note that the matrix A_{SM} has the dimension $N_M \times N_S$ while the matrix A_S is quadratic with $N_S \times N_S$ elements.

Using the method of the Schur complement, the solution is found as

$$\begin{aligned} A'_S &= A_S - (A_{SM})^T A_M^{-1} A_{SM} \\ B^{\text{ave}} &= (A'_S)^{-1} (C_S - (A_{SM})^T A_M^{-1} C_M) \\ M^{\text{ave}} &= A_M^{-1} [C_M - A_{SM} B^{\text{ave}}]. \end{aligned} \quad (43)$$

Given the components of the vector B^{ave} , $\beta_{j,\text{ave}} = \alpha_{j,\text{ave}}/\Delta_{\alpha_j}$, the solution for $\mu^{i,\text{ave}}$ can be written in explicit form

$$\mu^{i,\text{ave}} = \frac{\sum_e \left[\left(\mu_e^i + \sum_j \Gamma_{j,e}^i \beta_{j,\text{ave}} \right) \frac{w_{i,e}}{\Delta_{i,e}^2} \right]}{\sum_e \frac{w_{i,e}}{\Delta_{i,e}^2}}. \quad (44)$$

The uncorrelated uncertainty squared is determined by the inverse of the elements of the diagonal matrix A_M

$$\Delta_{i,\text{ave}}^2 = \frac{1}{\sum_e \frac{w_{i,e}}{\Delta_{i,e}^2}}. \quad (45)$$

Similarly, the contributions from statistical and systematic uncertainties can be calculated

$$\Delta_{i,\text{ave},\text{stat}}^2 = \Delta_{i,\text{ave}}^4 \sum_e \frac{w_{i,e}}{\Delta_{i,e}^4} \Delta_{i,e,\text{stat}}^2, \quad \Delta_{i,\text{ave},\text{unc}}^2 = \Delta_{i,\text{ave}}^4 \sum_e \frac{w_{i,e}}{\Delta_{i,e}^4} \Delta_{i,e,\text{unc}}^2. \quad (46)$$

Equation 44 and equation 45 reproduce the standard formula for a statistically weighted average of several uncorrelated measurements when all shifts of the systematic error sources are set to zero.

The non-diagonal nature of the matrix A'_S expresses the fact that the original sources of the systematic uncertainties are correlated with each other after averaging. The matrix A'_S can be decomposed to re-express equation 27 in terms of diagonalised systematic error sources

$$DD = UA'_S U^{-1} \quad \Gamma_{ave} = A_S A_M^{-1} D^{-1} U^{-1}. \quad (47)$$

Here U is an orthogonal matrix composed of the eigenvectors of A'_S , D is a diagonal matrix with corresponding square roots of eigenvalues as diagonal elements and Γ_{ave} represents the sensitivity of the average result to these new sources. Its elements are the $\Gamma_j^{i,\text{ave}}$ in equation 30.

References

- [1] E. D. Bloom *et al.*, Phys. Rev. Lett. **23**, 930 (1969).
- [2] D. J. Fox *et al.*, Phys. Rev. Lett. **33**, 1504 (1974).
- [3] I. Abt *et al.* [H1 Collaboration], Nucl. Phys. B **407**, 515 (1993).
- [4] M. Derrick *et al.* [ZEUS Collaboration], Phys. Lett. B **316**, 412 (1993).
- [5] C. Adloff *et al.* [H1 Collaboration], Eur. Phys. J. C **30**, 1 (2003), [[hep-ex/0304003](#)].
- [6] S. Chekanov *et al.* [ZEUS Collaboration], Phys. Rev. D **67**, 012007 (2003), [[hep-ex/0208023](#)].
- [7] J. Pumplin *et al.*, JHEP **0207**, 012 (2002), [[hep-ph/0201195](#)].
- [8] S. Alekhin, Phys. Rev. D **68**, 014002 (2003), [[hep-ph/0211096](#)].
- [9] V. N. Gribov and L. N. Lipatov, Sov. J. Nucl. Phys. **15**, 438 (1972).
- [10] V. N. Gribov and L. N. Lipatov, Sov. J. Nucl. Phys. **15**, 675 (1972).
- [11] L. N. Lipatov, Sov. J. Nucl. Phys. **20**, 94 (1975).
- [12] Y. L. Dokshitzer, Sov. Phys. JETP **46**, 641 (1977).
- [13] G. Altarelli and G. Parisi, Nucl. Phys. B **126**, 298 (1977).
- [14] E. A. Kuraev, L. N. Lipatov, and V. S. Fadin, Sov. Phys. JETP **44**, 443 (1976).
- [15] E. A. Kuraev, L. N. Lipatov, and V. S. Fadin, Sov. Phys. JETP **45**, 199 (1977).
- [16] I. I. Balitsky and L. N. Lipatov, Sov. J. Nucl. Phys. **28**, 822 (1978).
- [17] M. Ciafaloni, Nucl. Phys. B **296**, 49 (1988).
- [18] S. Catani, F. Fiorani, and G. Marchesini, Phys. Lett. B **234**, 339 (1990).
- [19] S. Catani, F. Fiorani, and G. Marchesini, Nucl. Phys. B **336**, 18 (1990).
- [20] G. Marchesini, Nucl. Phys. B **445**, 49 (1995), [[hep-ph/9412327](#)].
- [21] L. V. Gribov, E. M. Levin, and M. G. Ryskin, Phys. Rept. **100**, 1 (1983).
- [22] A. H. Mueller and J.-W. Qiu, Nucl. Phys. B **268**, 427 (1986).
- [23] I. Balitsky, Nucl. Phys. B **463**, 99 (1996), [[hep-ph/9509348](#)].
- [24] Y. V. Kovchegov, Phys. Rev. D **60**, 034008 (1999), [[hep-ph/9901281](#)].
- [25] M. Braun, Eur. Phys. J. C **16**, 337 (2000), [[hep-ph/0001268](#)].
- [26] E. Iancu, A. Leonidov, and L. D. McLerran, Nucl. Phys. A **692**, 583 (2001), [[hep-ph/0011241](#)].

- [27] J. Bartels, L. N. Lipatov, and G. P. Vacca, Nucl. Phys. B **706**, 391 (2005), [[hep-ph/0404110](#)].
- [28] J. Bartels and K. Kutak, Eur. Phys. J. **C53**, 533 (2008), [[0710.3060](#)].
- [29] S. Donnachie, G. Dosch, O. Nachtmann, and P. Landshoff, *Pomeron physics and QCD*, vol. 19 of *Camb. Monogr. Part. Phys. Nucl. Phys. Cosmol.* (2002), ISBN 052178039X.
- [30] N. N. Nikolaev and B. G. Zakharov, Z. Phys. C **49**, 607 (1991).
- [31] B. L. Ioffe, Phys. Lett. B **30**, 123 (1969).
- [32] V. N. Gribov, Sov. Phys. JETP **30**, 709 (1970).
- [33] T. Laštovička, Eur. Phys. J. C **24**, 529 (2002), [[hep-ph/0203260](#)].
- [34] G. Altarelli and G. Martinelli, Phys. Lett. B **76**, 89 (1978).
- [35] C. Adloff *et al.* [H1 Collaboration], Nucl. Phys. B **497**, 3 (1997), [[hep-ex/9703012](#)].
- [36] T. Ahmed *et al.* [H1 Collaboration], Z. Phys. **C66**, 529 (1995).
- [37] C. Adloff *et al.* [H1 Collaboration], Eur. Phys. J. C **21**, 33 (2001), [[hep-ex/0012053](#)].
- [38] J. Breitweg *et al.* [ZEUS Collaboration], Phys. Lett. B **487**, 53 (2000), [[hep-ex/0005018](#)].
- [39] S. Chekanov *et al.* [ZEUS Collaboration], Eur. Phys. J. C **21**, 443 (2001), [[hep-ex/0105090](#)].
- [40] S. Aid *et al.* [H1], Z. Phys. **C69**, 27 (1995), [[hep-ex/9509001](#)].
- [41] E. Gotsman, E. M. Levin, and U. Maor, Eur. Phys. J. C **5**, 303 (1998), [[hep-ph/9708275](#)].
- [42] K. Golec-Biernat and M. Wüsthoff, Phys. Rev. D **59**, 014017 (1999), [[hep-ph/9807513](#)].
- [43] J. R. Forshaw, G. Kerley, and G. Shaw, Phys. Rev. D **60**, 074012 (1999), [[hep-ph/9903341](#)].
- [44] J. Bartels, K. Golec-Biernat, and H. Kowalski, Phys. Rev. D **66**, 014001 (2002), [[hep-ph/0203258](#)].
- [45] E. Iancu, K. Itakura, and S. Munier, Phys. Lett. **B590**, 199 (2004), [[hep-ph/0310338](#)].
- [46] H. Kowalski, L. Motyka, and G. Watt, Phys. Rev. D **74**, 074016 (2006), [[hep-ph/0606272](#)].
- [47] A. Blondel and F. Jacquet, in *Proc. ep Facility for Europe, Amsterdam 1979* (DESY 79/48, 1979).
- [48] U. Bassler and G. Bernardi, Nucl. Instr. and Meth. A **361**, 197 (1995), [[hep-ex/9412004](#)].
- [49] H. Abramowicz and A. Levy (1997), [[hep-ph/9712415](#)].
- [50] I. Abt *et al.* [H1 Collaboration], Nucl. Instr. and Meth. A **386**, 310 (1997).

- [51] I. Abt *et al.* [H1 Collaboration], Nucl. Instr. and Meth. A **386**, 348 (1997).
- [52] R. D. Appuhn *et al.*, *H1 backward upgrade with a SPACAL calorimeter: The Hadronic section*, DESY (1996), [[96-013](#)].
- [53] T. Nicholls *et al.* [H1 SpaCal Group], Nucl. Instr. and Meth. A **374**, 149 (1996).
- [54] R. D. Appuhn *et al.* [H1 SpaCal Group], Nucl. Instr. and Meth. A **382**, 395 (1996).
- [55] R. D. Appuhn *et al.* [H1 SpaCal Group], Nucl. Instr. and Meth. A **386**, 397 (1997).
- [56] D. Pitzl *et al.*, Nucl. Instr. and Meth. A **454**, 334 (2000), [[hep-ex/0002044](#)].
- [57] B. Andrieu *et al.* [H1 Calorimeter Group], Nucl. Instr. and Meth. A **336**, 460 (1993).
- [58] B. Andrieu *et al.* [H1 Calorimeter Group], Nucl. Instr. and Meth. A **336**, 499 (1993).
- [59] H. Henschel and R. Lahmann, Nucl. Instrum. Meth. **A453**, 93 (2000).
- [60] W. Eick *et al.*, Nucl. Instr. and Meth. A **386**, 81 (1997).
- [61] R. Horisberger and D. Pitzl, Nucl. Instrum. Meth. **A326**, 92 (1993).
- [62] W. J. Haynes *et al.*, Nucl. Instr. and Meth. A **403**, 313 (1998).
- [63] B. Schwab, Doctoral thesis, Ruprecht-Karls-Universität Heidelberg (1996), [<http://www-h1.desy.de/psfiles/theses/h1th-236.ps>].
- [64] V. Karimaki, Helsinki University (1991), [[HU-SEFT-1991-10](#)].
- [65] S. Glazov, Doctoral thesis, Humboldt-Universität zu Berlin (1998), [[DESY-THESIS-1998-005](#)].
- [66] G. A. Schuler and H. Spiesberger, in *Proc. of the Workshop on HERA Physics*, edited by W. Buchmuller and G. Ingelman (DESY, Hamburg, 1992), vol. 3, p. 1419, DJANGO 1.4.
- [67] A. Kwiatkowski, H. Spiesberger, and H.-J. Moehring, Comp. Phys. Comm. **69**, 155 (1992).
- [68] G. Gustafson and U. Petterson, Nucl. Phys. B **306**, 746 (1988).
- [69] B. Andersson *et al.*, Z. Phys. C **43**, 625 (1989).
- [70] L. Lönnblad, Comp. Phys. Comm. **71**, 15 (1992), ARIADNE 4.1.
- [71] A. Mücke *et al.*, Comp. Phys. Comm. **124**, 290 (2000), [[astro-ph/9903478](#)].
- [72] T. Sjostrand, Comput. Phys. Commun. **82**, 74 (1994), JETSET 7.4.
- [73] R. Engel, Z. Phys. C **66**, 203 (1995).
- [74] R. Engel and J. Ranft, Phys. Rev. D **54**, 4244 (1996), PHOJET 1.6, [[hep-ph/9509373](#)].
- [75] A. Capella *et al.*, Phys. Rep. **236**, 227 (1994).

- [76] A. Arbuzov *et al.*, Comp. Phys. Comm. **94**, 128 (1996), HECTOR 1.0, [[hep-ph/9511434](#)].
- [77] R. Brun *et al.*, *GEANT3 User's Guide*, CERN (1987), [[CERN-DD/EE 84-01](#)].
- [78] G. Grindhammer, M. Rudowicz, and S. Peters, Nucl. Instr. and Meth. A **290**, 469 (1990).
- [79] H. Fesefeld, *The Simulation of Hadronic Showers—Physics and Applications*, RWTH Aachen (1985), [[PITHA 85/02](#)].
- [80] D. Eckstein, Doctoral thesis, Humboldt-Universität zu Berlin (2002), [[DESY-THESIS-2002-008](#)].
- [81] T. Laštovička, Doctoral thesis, Humboldt-Universität zu Berlin (2004), [[DESY-THESIS-2004-016](#)].
- [82] A. Vargas, Doctoral thesis, Universität Dortmund (2006), [<http://www-h1.desy.de/psfiles/theses/h1th-453.pdf>].
- [83] O. Behrendt, Doctoral thesis, Universität Dortmund (2006), [<http://www-h1.desy.de/psfiles/theses/h1th-452.pdf>].
- [84] V. Blobel and C. Kleinwort, *A new method for the high precision alignment of track detectors* (2002), [[hep-ex/0208021](#)].
- [85] V. Lendermann, Doctoral thesis, Universität Dortmund (2001), [[DESY-THESIS-2002-004](#)].
- [86] A. Aktas *et al.* [H1 Collaboration], Phys. Lett. B **598**, 159 (2004).
- [87] A. Glazov, AIP Conf. Proc. **792**, 237 (2005).
- [88] C. Adloff *et al.* [H1 Collaboration], Physics Letters B **520**, 183 (2001), [[hep-ex/0108035](#)].
- [89] F. D. Aaron *et al.* [H1 Collaboration], Phys. Lett. **B665**, 139 (2008), [[0805.2809](#)].
- [90] J. Bartels, K. Golec-Biernat, and K. Peters, Eur. Phys. J. C **17**, 121 (2000), [[hep-ph/0003042](#)].

Q^2 GeV ²	x	y	σ_r	δ_{tot} %	δ_{stat} %	δ_{uncor} %	$\gamma_{E'_e}$ %	γ_{θ_e} %	$\gamma_{E_{\text{had}}}$ %	γ_{noise} %	$\gamma_{E_{\text{SpaCal}}^h}$ %	$\gamma_{\gamma p}$ %
0.20	3.980×10^{-5}	4.948×10^{-2}	0.249	20.3	13.8	12.0	0.58	-1.74	5.70	-0.34	-1.37	-6.44
0.20	2.510×10^{-4}	7.845×10^{-3}	0.162	16.7	14.2	6.19	1.38	-0.78	-1.65	-3.64	-4.21	-1.68
0.25	3.980×10^{-5}	6.184×10^{-2}	0.302	17.5	9.80	11.3	0.49	-2.22	3.10	-1.48	-2.62	-7.69
0.25	2.510×10^{-4}	9.806×10^{-3}	0.163	14.1	10.8	4.71	-1.93	0.70	0.01	-4.47	-5.71	-1.42
0.25	1.580×10^{-3}	1.558×10^{-3}	0.182	13.2	11.5	5.29	0.57	0.46	-1.73	-1.93	-2.61	-0.30
0.35	5.120×10^{-6}	6.726×10^{-1}	0.458	25.2	21.6	12.8	-0.61	-0.51	0.34	-0.03	0.59	-2.45
0.35	3.200×10^{-5}	1.077×10^{-1}	0.361	22.2	9.72	11.1	-2.17	-0.08	-1.61	0.54	-6.88	-14.78
0.35	1.300×10^{-4}	2.651×10^{-2}	0.265	11.6	9.61	4.38	-0.38	0.27	2.55	-2.99	-0.51	-2.46
0.35	5.000×10^{-4}	6.892×10^{-3}	0.216	11.1	9.22	4.19	-0.91	-0.81	-0.47	-3.51	-2.48	-0.53
0.35	2.510×10^{-3}	1.373×10^{-3}	0.193	11.6	10.2	4.55	-1.19	-0.25	-0.04	-2.49	-1.47	-0.08
0.50	7.320×10^{-6}	6.726×10^{-1}	0.483	10.0	5.23	5.74	0.18	1.96	2.31	-0.18	2.75	-4.84
0.50	1.580×10^{-5}	3.116×10^{-1}	0.477	21.6	18.6	9.84	-3.86	-2.83	0.27	0.03	0.47	-0.19
0.50	3.980×10^{-5}	1.237×10^{-1}	0.431	17.7	10.7	6.07	-2.11	0.82	-1.48	-0.10	-4.88	-11.49
0.50	1.000×10^{-4}	4.923×10^{-2}	0.388	11.0	9.10	4.87	-0.30	0.57	-0.02	0.52	-3.39	-1.75
0.50	2.510×10^{-4}	1.961×10^{-2}	0.262	12.8	10.6	4.45	0.01	-1.43	0.66	-4.32	-3.28	-1.27
0.50	8.000×10^{-4}	6.154×10^{-3}	0.275	9.51	7.92	3.86	-0.40	-0.43	0.04	-3.41	-0.90	-0.22
0.65	9.520×10^{-6}	6.726×10^{-1}	0.502	6.22	3.87	2.90	-1.15	0.68	1.11	-0.18	1.85	-2.98
0.65	1.580×10^{-5}	4.050×10^{-1}	0.474	6.68	3.06	5.44	-0.63	-2.05	0.24	-0.09	0.34	-0.92
0.65	3.980×10^{-5}	1.608×10^{-1}	0.681	21.7	17.4	11.2	-6.22	2.19	-0.04	0.04	-0.15	0.00
0.65	1.000×10^{-4}	6.400×10^{-2}	0.424	13.2	5.59	5.85	-1.89	-2.22	-1.17	0.52	-9.22	-3.52
0.65	2.510×10^{-4}	2.550×10^{-2}	0.353	10.6	8.94	4.04	-0.78	-1.00	-0.48	0.49	-3.39	-1.53
0.65	8.000×10^{-4}	8.000×10^{-3}	0.283	10.5	7.57	3.61	-1.74	0.53	1.06	-5.94	-0.75	-0.15
0.65	3.200×10^{-3}	2.000×10^{-3}	0.246	10.1	8.92	4.05	-1.83	0.36	-0.68	1.63	-0.36	-0.09
0.85	1.244×10^{-5}	6.726×10^{-1}	0.594	5.01	2.48	2.52	-1.16	-0.22	1.23	-0.17	1.77	-2.55
0.85	2.000×10^{-5}	4.184×10^{-1}	0.623	6.24	1.94	5.36	-0.98	-2.27	0.16	-0.03	0.34	-0.45
0.85	3.980×10^{-5}	2.103×10^{-1}	0.564	6.24	2.03	5.37	-0.98	-2.23	0.01	-0.08	0.00	-0.05
0.85	1.000×10^{-4}	8.369×10^{-2}	0.493	7.75	4.98	5.78	-0.38	-0.81	0.16	-0.77	0.63	0.00
0.85	2.510×10^{-4}	3.334×10^{-2}	0.353	11.3	8.06	3.75	0.57	-1.86	-1.56	0.17	-6.37	-1.05
0.85	8.000×10^{-4}	1.046×10^{-2}	0.325	8.86	6.77	3.41	-0.19	-0.32	1.16	-4.25	-1.20	-0.26
0.85	3.200×10^{-3}	2.615×10^{-3}	0.318	8.65	7.27	3.78	0.55	-1.91	1.43	-1.05	-0.73	-0.04
1.20	1.757×10^{-5}	6.726×10^{-1}	0.652	5.82	2.66	2.51	-1.08	-0.35	1.33	-0.26	2.16	-3.57
1.20	2.000×10^{-5}	5.907×10^{-1}	0.686	3.95	2.59	2.51	-0.73	-0.46	0.40	-0.04	0.91	-0.93
1.20	3.200×10^{-5}	3.692×10^{-1}	0.697	3.78	1.66	2.73	-0.81	-1.73	0.22	-0.10	0.09	-0.59
1.20	6.310×10^{-5}	1.872×10^{-1}	0.653	4.12	1.37	2.71	-1.17	-2.50	0.07	-0.22	0.22	-0.02
1.20	1.580×10^{-4}	7.478×10^{-2}	0.498	4.40	2.06	2.78	0.69	-2.07	0.70	-1.43	0.35	0.00
1.20	3.980×10^{-4}	2.969×10^{-2}	0.471	7.52	5.21	3.16	-2.04	0.11	-1.35	-0.02	-3.65	-0.10
1.20	1.300×10^{-3}	9.088×10^{-3}	0.378	6.85	5.08	3.09	-2.10	-0.39	1.38	-2.00	-1.05	-0.03
1.20	5.000×10^{-3}	2.363×10^{-3}	0.322	8.23	6.55	3.54	-1.54	-1.25	2.10	1.84	-0.71	0.00

Table 10: Reduced cross section σ_r , as measured with the SVX data sample for $0.2 \leq Q^2 \leq 1.2$ GeV². The uncertainties are quoted in % relative to σ_r . δ_{tot} is the total uncertainty determined as the quadratic sum of systematic and statistical uncertainties. δ_{stat} is the statistical uncertainty. δ_{uncor} represents the uncorrelated systematic uncertainty. $\gamma_{E'_e}$, γ_{θ_e} , $\gamma_{E_{\text{had}}}$, γ_{noise} , $\gamma_{E_{\text{SpaCal}}^h}$ and $\gamma_{\gamma p}$ are the bin-to-bin correlated systematic uncertainties in the cross section measurement due to uncertainties in the SpaCal electromagnetic energy scale, electron scattering angle, LAr calorimeter hadronic energy scale, LAr calorimeter noise, SpaCal hadronic energy scale and the photoproduction background, respectively. The luminosity uncertainty of 3% for the SVX data is not included in δ_{tot} .

Q^2 GeV ²	x	y	σ_r	δ_{tot} %	δ_{stat} %	δ_{uncor} %	$\gamma_{E'_e}$ %	γ_{θ_e} %	$\gamma_{E_{\text{had}}}$ %	γ_{noise} %	$\gamma_{E_{\text{SpaCal}}^h}$ %	$\gamma_{\gamma p}$ %
1.50	2.196×10^{-5}	6.726×10^{-1}	0.722	4.43	2.45	2.47	-1.08	-0.58	0.81	-0.20	1.37	-1.86
1.50	3.200×10^{-5}	4.615×10^{-1}	0.774	3.28	1.78	2.36	-0.63	-0.76	0.39	-0.10	0.65	-0.68
1.50	5.000×10^{-5}	2.954×10^{-1}	0.773	3.80	1.46	2.71	-0.93	-2.02	0.01	-0.09	-0.04	-0.13
1.50	8.000×10^{-5}	1.846×10^{-1}	0.727	3.92	1.57	2.73	-0.84	-2.17	0.04	-0.18	0.16	-0.02
1.50	1.300×10^{-4}	1.136×10^{-1}	0.654	4.31	1.77	2.75	-0.94	-2.57	0.18	-0.54	0.28	-0.01
1.50	2.000×10^{-4}	7.384×10^{-2}	0.628	5.58	3.57	2.77	-3.21	-0.43	0.45	-0.15	0.00	0.00
1.50	3.200×10^{-4}	4.615×10^{-2}	0.564	4.78	1.90	2.76	-0.45	-2.40	-1.13	0.11	-2.08	-0.14
1.50	8.000×10^{-4}	1.846×10^{-2}	0.483	4.32	2.38	2.47	-1.61	-0.99	0.33	-1.23	-1.30	-0.02
1.50	3.200×10^{-3}	4.615×10^{-3}	0.424	5.02	2.69	2.56	-1.41	-0.56	2.17	-2.06	-0.31	0.00
1.50	1.300×10^{-2}	1.136×10^{-3}	0.384	14.1	4.49	3.05	-1.71	-0.37	1.16	12.8	-0.33	0.00
2.00	2.928×10^{-5}	6.726×10^{-1}	0.822	4.28	2.19	2.39	-0.61	-0.93	1.07	-0.18	1.51	-1.75
2.00	5.000×10^{-5}	3.938×10^{-1}	0.837	3.10	1.62	2.33	-0.84	-0.76	0.27	-0.22	0.20	-0.30
2.00	8.000×10^{-5}	2.461×10^{-1}	0.791	3.03	1.63	2.34	-0.94	-0.32	0.29	-0.15	0.00	-0.05
2.00	1.300×10^{-4}	1.515×10^{-1}	0.731	3.28	1.81	2.36	-1.33	-0.07	0.37	-0.12	0.00	-0.01
2.00	2.000×10^{-4}	9.846×10^{-2}	0.700	3.58	1.97	2.39	-1.73	-0.28	0.46	-0.11	0.00	-0.01
2.00	3.200×10^{-4}	6.154×10^{-2}	0.578	4.39	2.14	2.40	-0.73	-0.65	-0.78	-0.16	-2.71	-0.03
2.00	5.000×10^{-4}	3.938×10^{-2}	0.528	3.95	2.41	2.43	-1.46	-0.07	-0.61	-0.28	-1.16	-0.01
2.00	1.000×10^{-3}	1.969×10^{-2}	0.490	3.79	1.86	2.36	-1.38	-0.11	0.67	-1.62	-0.61	-0.01
2.00	3.200×10^{-3}	6.154×10^{-3}	0.424	4.65	1.63	2.34	-1.35	-0.07	2.41	-2.41	-0.25	0.00
2.00	1.300×10^{-2}	1.515×10^{-3}	0.404	10.5	2.46	2.48	-1.12	-0.52	0.95	9.81	-0.25	0.00
2.50	5.000×10^{-5}	4.923×10^{-1}	0.881	3.68	2.28	2.40	-0.96	-0.47	0.65	-0.18	0.68	-0.75
2.50	8.000×10^{-5}	3.077×10^{-1}	0.869	3.08	1.66	2.34	-0.80	-0.74	0.30	0.03	0.04	-0.14
2.50	1.300×10^{-4}	1.893×10^{-1}	0.800	3.04	1.63	2.34	-0.85	-0.53	0.33	-0.03	0.00	-0.01
2.50	2.000×10^{-4}	1.231×10^{-1}	0.777	3.25	1.63	2.34	-1.44	-0.47	0.36	-0.16	0.00	-0.01
2.50	3.200×10^{-4}	7.692×10^{-2}	0.683	4.03	1.71	2.35	-2.69	-0.52	0.48	-0.15	0.00	-0.01
2.50	5.000×10^{-4}	4.923×10^{-2}	0.601	3.45	1.90	2.36	0.15	-0.85	-0.10	-0.81	-1.14	-0.01
2.50	8.000×10^{-4}	3.077×10^{-2}	0.574	3.31	1.96	2.38	-0.23	-0.41	0.35	-0.95	-0.49	0.00
2.50	1.580×10^{-3}	1.558×10^{-2}	0.527	3.99	1.44	2.32	-0.20	-0.42	1.17	-2.60	-0.27	0.00
2.50	5.000×10^{-3}	4.923×10^{-3}	0.448	4.10	1.29	2.31	-0.19	-0.58	2.66	-1.53	-0.21	0.00
2.50	2.000×10^{-2}	1.231×10^{-3}	0.409	16.8	2.30	2.44	-0.14	-0.63	0.73	16.4	-0.18	0.00
3.50	8.000×10^{-5}	4.307×10^{-1}	0.971	3.75	2.35	2.42	-1.09	-1.15	0.32	-0.14	0.22	-0.25
3.50	1.300×10^{-4}	2.651×10^{-1}	0.925	3.21	1.81	2.36	-0.50	-1.04	0.34	-0.05	0.00	-0.05
3.50	2.000×10^{-4}	1.723×10^{-1}	0.852	3.20	1.78	2.35	-1.02	-0.64	0.35	-0.08	0.00	-0.02
3.50	3.200×10^{-4}	1.077×10^{-1}	0.779	3.44	1.80	2.36	-1.53	-0.71	0.40	-0.14	0.00	-0.01
3.50	5.000×10^{-4}	6.892×10^{-2}	0.716	3.49	1.96	2.38	0.39	-0.73	0.02	-0.88	-1.11	-0.01
3.50	8.000×10^{-4}	4.307×10^{-2}	0.651	3.59	2.02	2.38	0.36	-0.66	0.45	-1.45	-0.56	0.00
3.50	1.300×10^{-3}	2.651×10^{-2}	0.588	3.65	2.09	2.39	0.36	-0.88	0.37	-1.46	-0.30	0.00
3.50	2.510×10^{-3}	1.373×10^{-2}	0.566	4.57	1.48	2.33	0.23	-0.63	1.87	-3.04	-0.22	0.00
3.50	8.000×10^{-3}	4.307×10^{-3}	0.481	3.76	1.38	2.32	0.30	-0.73	2.48	0.20	-0.17	0.00

Table 11: Reduced cross section σ_r , as measured with the SVX data sample for $1.5 \leq Q^2 \leq 3.5$ GeV². The uncertainties are quoted in % relative to σ_r . δ_{tot} is the total uncertainty determined as the quadratic sum of systematic and statistical uncertainties. δ_{stat} is the statistical uncertainty. δ_{uncor} represents the uncorrelated systematic uncertainty. $\gamma_{E'_e}$, γ_{θ_e} , $\gamma_{E_{\text{had}}}$, γ_{noise} , $\gamma_{E_{\text{SpaCal}}^h}$ and $\gamma_{\gamma p}$ are the bin-to-bin correlated systematic uncertainties in the cross section measurement due to uncertainties in the SpaCal electromagnetic energy scale, electron scattering angle, LAr calorimeter hadronic energy scale, LAr calorimeter noise, SpaCal hadronic energy scale and the photoproduction background, respectively. The luminosity uncertainty of 3% for the SVX data is not included in δ_{tot} .

Q^2 GeV ²	x	y	σ_r	δ_{tot} %	δ_{stat} %	δ_{uncor} %	$\gamma_{E'_e}$ %	γ_{θ_e} %	$\gamma_{E_{\text{had}}}$ %	γ_{noise} %	$\gamma_{E_{\text{SpaCal}}^h}$ %	$\gamma_{\gamma p}$ %
0.50	2.510×10^{-4}	1.968×10^{-2}	0.334	19.6	14.4	10.0	1.91	-1.41	1.76	0.43	-6.60	-4.90
0.50	8.000×10^{-4}	6.176×10^{-3}	0.266	11.7	9.14	6.46	-0.46	-0.75	-1.13	-2.77	-0.84	-1.10
0.50	3.200×10^{-3}	1.544×10^{-3}	0.184	13.5	11.3	6.39	-0.76	0.65	-0.94	0.61	-3.15	-0.59
0.65	2.510×10^{-4}	2.559×10^{-2}	0.385	14.2	10.8	6.38	-0.77	0.64	0.25	-2.71	-5.02	-3.39
0.65	8.000×10^{-4}	8.029×10^{-3}	0.315	8.75	6.62	4.88	0.06	0.57	-1.69	-1.78	-1.52	-0.46
0.65	3.200×10^{-3}	2.007×10^{-3}	0.209	9.47	7.68	4.59	-0.03	0.68	-0.76	-2.43	-1.64	-0.14
0.85	1.000×10^{-4}	8.399×10^{-2}	0.523	20.5	14.2	5.30	-1.12	-0.62	-0.92	-1.13	-4.02	-13.04
0.85	2.510×10^{-4}	3.346×10^{-2}	0.428	11.9	9.45	4.93	-0.63	0.71	0.07	-1.49	-3.32	-3.71
0.85	8.000×10^{-4}	1.050×10^{-2}	0.359	8.15	6.42	4.13	-0.51	0.22	-0.98	-1.97	-0.54	-1.63
0.85	3.200×10^{-3}	2.625×10^{-3}	0.302	7.22	5.82	3.98	-0.36	0.27	-0.90	-0.10	-1.17	-0.11
1.20	1.757×10^{-5}	6.750×10^{-1}	0.563	10.1	6.54	3.79	-1.95	1.82	-0.15	-0.16	1.00	-6.00
1.20	1.580×10^{-4}	7.505×10^{-2}	0.542	15.8	10.2	4.06	-0.24	0.26	-0.90	-0.93	-7.76	-8.15
1.20	3.980×10^{-4}	2.979×10^{-2}	0.501	8.02	6.08	4.14	0.00	0.38	0.18	-0.94	-2.70	-1.37
1.20	1.300×10^{-3}	9.121×10^{-3}	0.364	7.27	4.98	4.45	0.07	-0.11	-1.48	-2.36	-0.50	-0.50
1.20	5.000×10^{-3}	2.372×10^{-3}	0.295	7.64	6.03	3.75	1.51	-0.06	-1.63	0.84	-1.51	-0.25
1.50	2.196×10^{-5}	6.750×10^{-1}	0.703	5.78	3.08	2.53	-0.95	0.49	-0.10	-0.11	0.90	-3.94
1.50	3.200×10^{-5}	4.632×10^{-1}	0.706	8.41	6.46	4.21	-0.66	2.58	-0.07	-0.09	0.67	-1.95
1.50	3.200×10^{-4}	4.632×10^{-2}	0.565	10.7	7.50	3.18	-1.08	0.09	-0.14	-0.68	-5.64	-3.71
1.50	1.000×10^{-3}	1.482×10^{-2}	0.459	6.94	5.24	3.74	-1.41	0.73	-0.93	-1.45	-1.04	-0.44
1.50	3.200×10^{-3}	4.632×10^{-3}	0.390	6.13	4.43	3.29	-0.53	0.04	-2.05	-1.51	-0.63	0.00
1.50	1.300×10^{-2}	1.140×10^{-3}	0.331	11.5	6.93	4.32	1.21	-0.49	-1.26	7.65	-1.98	0.00
2.00	2.928×10^{-5}	6.750×10^{-1}	0.788	4.45	2.00	2.28	-1.08	0.19	-0.13	-0.11	1.10	-2.85
2.00	5.000×10^{-5}	3.953×10^{-1}	0.792	5.31	4.25	2.58	-0.91	1.42	-0.16	-0.08	0.29	-0.73
2.00	3.200×10^{-4}	6.176×10^{-2}	0.645	12.2	3.48	2.70	-2.66	1.50	0.91	0.92	-10.8	-1.58
2.00	1.000×10^{-3}	1.976×10^{-2}	0.527	5.93	4.55	3.36	0.77	-0.05	-0.20	-0.41	-1.43	-0.52
2.00	3.200×10^{-3}	6.176×10^{-3}	0.426	5.80	3.93	3.06	-0.63	0.51	-2.41	-1.00	-1.16	-0.05
2.00	1.300×10^{-2}	1.520×10^{-3}	0.372	9.24	5.78	3.79	-0.68	0.63	-0.80	5.80	-1.55	0.00
2.50	3.660×10^{-5}	6.750×10^{-1}	0.857	4.42	2.29	2.29	-0.70	-0.32	-0.21	-0.12	0.96	-2.73
2.50	5.000×10^{-5}	4.941×10^{-1}	0.856	3.39	1.99	2.26	-1.01	0.00	-0.19	-0.10	0.52	-1.05
2.50	8.000×10^{-5}	3.088×10^{-1}	0.839	3.01	1.63	2.29	-0.76	0.66	-0.27	-0.05	0.12	-0.23
2.50	1.300×10^{-4}	1.900×10^{-1}	0.759	4.67	2.73	2.62	-1.39	2.32	-0.31	0.00	0.00	-0.05
2.50	2.000×10^{-4}	1.235×10^{-1}	0.756	7.06	4.84	3.65	-1.19	3.38	-0.38	0.00	0.00	-0.10
2.50	5.000×10^{-4}	4.941×10^{-2}	0.651	8.65	1.99	2.36	-2.61	1.76	0.86	1.25	-7.27	-0.55
2.50	1.580×10^{-3}	1.564×10^{-2}	0.511	5.86	3.52	2.92	-2.34	2.37	-0.16	0.61	-1.40	-0.10
2.50	5.000×10^{-3}	4.941×10^{-3}	0.451	5.91	3.27	2.82	-1.43	2.21	-2.87	-0.75	-0.79	0.00
3.50	5.124×10^{-5}	6.750×10^{-1}	0.935	4.27	2.17	2.25	-0.87	-0.14	-0.16	-0.11	1.03	-2.57
3.50	8.000×10^{-5}	4.323×10^{-1}	0.947	2.89	1.49	2.20	-0.85	-0.20	-0.20	-0.09	0.38	-0.57
3.50	1.300×10^{-4}	2.660×10^{-1}	0.908	2.63	1.21	2.21	-0.67	0.00	-0.35	-0.01	0.00	-0.07
3.50	2.000×10^{-4}	1.729×10^{-1}	0.879	2.83	1.42	2.26	-0.83	0.35	-0.30	0.00	0.00	-0.03
3.50	3.200×10^{-4}	1.081×10^{-1}	0.775	3.60	1.75	2.32	-1.70	1.21	-0.45	0.00	0.00	0.00
3.50	8.000×10^{-4}	4.323×10^{-2}	0.651	4.34	1.08	2.20	-1.44	0.67	0.30	0.38	-3.17	-0.12
3.50	2.510×10^{-3}	1.378×10^{-2}	0.533	3.64	1.66	2.31	-1.54	1.14	-0.80	-0.19	-0.89	-0.01
3.50	8.000×10^{-3}	4.323×10^{-3}	0.433	4.44	1.68	2.31	-1.56	1.20	-2.71	0.46	-0.36	-0.01

Table 12: Reduced cross section σ_r , as measured with the NVX-BST data sample for $0.5 \leq Q^2 \leq 3.5$ GeV². The uncertainties are quoted in % relative to σ_r . δ_{tot} is the total uncertainty determined as the quadratic sum of systematic and statistical uncertainties. δ_{stat} is the statistical uncertainty. δ_{uncor} represents the uncorrelated systematic uncertainty. $\gamma_{E'_e}$, γ_{θ_e} , $\gamma_{E_{\text{had}}}$, γ_{noise} , $\gamma_{E_{\text{SpaCal}}^h}$ and $\gamma_{\gamma p}$ are the bin-to-bin correlated systematic uncertainties in the cross section measurement due to uncertainties in the SpaCal electromagnetic energy scale, electron scattering angle, LAr calorimeter hadronic energy scale, LAr calorimeter noise, SpaCal hadronic energy scale and the photoproduction background, respectively. The luminosity uncertainty of 1.1% for the NVX data is not included in δ_{tot} .

Q^2 GeV ²	x	y	σ_r	δ_{tot} %	δ_{stat} %	δ_{uncor} %	$\gamma_{E'_e}$ %	γ_{θ_e} %	$\gamma_{E_{\text{had}}}$ %	γ_{noise} %	$\gamma_{E_{\text{SpaCal}}^h}$ %	$\gamma_{\gamma p}$ %
5.00	7.320×10^{-5}	6.750×10^{-1}	1.052	3.26	1.60	2.21	-0.75	-0.31	-0.22	-0.12	0.84	-1.33
5.00	1.300×10^{-4}	3.801×10^{-1}	1.066	2.72	1.33	2.20	-0.79	-0.32	-0.26	-0.07	0.09	-0.14
5.00	2.000×10^{-4}	2.470×10^{-1}	1.009	2.62	1.13	2.20	-0.75	-0.22	-0.40	0.00	0.00	-0.03
5.00	3.200×10^{-4}	1.544×10^{-1}	0.911	2.79	1.20	2.21	-1.15	-0.17	-0.32	0.00	0.00	-0.01
5.00	5.000×10^{-4}	9.881×10^{-2}	0.838	3.11	1.27	2.22	-1.72	-0.04	-0.40	0.00	0.00	0.00
5.00	8.000×10^{-4}	6.176×10^{-2}	0.775	3.50	1.29	2.23	-0.27	-0.09	0.17	-0.40	-2.32	-0.02
5.00	1.300×10^{-3}	3.801×10^{-2}	0.686	2.91	1.39	2.24	-0.46	0.07	-0.18	-0.53	-0.99	-0.04
5.00	2.000×10^{-3}	2.470×10^{-2}	0.636	2.84	1.45	2.26	-0.69	0.26	-0.24	-0.06	-0.53	-0.01
5.00	3.980×10^{-3}	1.241×10^{-2}	0.569	3.18	1.08	2.20	-0.50	-0.04	-1.73	-0.86	-0.33	-0.01
5.00	1.300×10^{-2}	3.801×10^{-3}	0.440	3.90	1.13	2.20	-0.43	0.05	-2.50	1.62	-0.26	0.00
6.50	9.515×10^{-5}	6.750×10^{-1}	1.050	4.71	2.96	2.31	-0.65	-0.19	-0.20	-0.14	0.82	-2.63
6.50	1.300×10^{-4}	4.941×10^{-1}	1.122	2.98	1.67	2.22	-0.80	-0.45	-0.23	-0.11	0.37	-0.31
6.50	2.000×10^{-4}	3.211×10^{-1}	1.122	2.70	1.25	2.20	-0.84	-0.24	-0.31	-0.03	0.02	-0.06
6.50	3.200×10^{-4}	2.007×10^{-1}	1.024	2.70	1.19	2.20	-0.85	-0.40	-0.39	0.00	0.00	-0.01
6.50	5.000×10^{-4}	1.285×10^{-1}	0.937	2.79	1.22	2.21	-1.08	-0.41	-0.31	0.00	0.00	-0.01
6.50	8.000×10^{-4}	8.029×10^{-2}	0.865	3.50	1.25	2.22	-2.31	-0.51	-0.39	0.00	0.00	0.00
6.50	1.300×10^{-3}	4.941×10^{-2}	0.780	3.06	1.32	2.23	0.19	-0.22	-0.41	-0.96	-1.20	-0.03
6.50	2.000×10^{-3}	3.211×10^{-2}	0.691	2.80	1.36	2.24	0.48	-0.55	-0.03	-0.33	-0.59	0.00
6.50	3.980×10^{-3}	1.614×10^{-2}	0.618	2.79	1.00	2.19	0.07	-0.22	-1.09	-0.82	-0.28	0.00
6.50	1.300×10^{-2}	4.941×10^{-3}	0.497	3.52	0.98	2.18	0.03	-0.24	-2.39	0.89	-0.24	0.00
8.50	1.244×10^{-4}	6.750×10^{-1}	1.207	3.60	2.26	2.28	-0.65	-0.33	-0.21	-0.12	0.88	-1.15
8.50	2.000×10^{-4}	4.200×10^{-1}	1.176	2.87	1.52	2.22	-0.90	-0.27	-0.22	-0.09	0.20	-0.14
8.50	3.200×10^{-4}	2.625×10^{-1}	1.097	2.76	1.29	2.21	-0.94	-0.31	-0.30	0.00	0.00	-0.01
8.50	5.000×10^{-4}	1.680×10^{-1}	1.036	2.71	1.30	2.22	-0.71	-0.39	-0.28	0.00	0.00	0.00
8.50	8.000×10^{-4}	1.050×10^{-1}	0.959	3.05	1.32	2.23	-1.53	-0.30	-0.38	0.00	0.00	0.00
8.50	1.300×10^{-3}	6.461×10^{-2}	0.837	3.13	1.41	2.24	0.43	-0.55	-0.26	-0.97	-1.14	0.00
8.50	2.000×10^{-3}	4.200×10^{-2}	0.784	2.89	1.43	2.25	0.47	-0.47	-0.20	-0.53	-0.68	0.00
8.50	3.200×10^{-3}	2.625×10^{-2}	0.679	2.91	1.49	2.26	0.37	-0.44	-0.45	-0.66	-0.42	0.00
8.50	6.310×10^{-3}	1.331×10^{-2}	0.621	3.09	1.08	2.20	0.16	-0.34	-1.59	-0.89	-0.29	0.00
8.50	2.000×10^{-2}	4.200×10^{-3}	0.464	3.99	1.20	2.21	0.41	-0.50	-1.77	2.45	-0.27	0.00
12.00	8.000×10^{-4}	1.482×10^{-1}	1.067	3.05	1.45	2.25	-1.40	-0.34	-0.24	0.00	0.00	0.00
12.00	1.300×10^{-3}	9.121×10^{-2}	0.938	3.31	1.54	2.26	0.48	-0.36	-0.29	-0.80	-1.54	-0.01
12.00	2.000×10^{-3}	5.929×10^{-2}	0.850	3.00	1.58	2.27	0.47	-0.42	-0.08	-0.67	-0.67	0.00
12.00	3.200×10^{-3}	3.706×10^{-2}	0.752	2.98	1.63	2.29	0.44	-0.39	-0.40	-0.55	-0.40	0.00
12.00	6.310×10^{-3}	1.879×10^{-2}	0.650	2.89	1.21	2.22	0.46	-0.47	-0.91	-0.77	-0.31	0.00
12.00	2.000×10^{-2}	5.929×10^{-3}	0.494	3.45	1.25	2.22	0.54	-0.56	-1.75	1.32	-0.26	0.00

Table 13: Reduced cross section σ_r , as measured with the NVX-BST data sample for $5 \leq Q^2 \leq 12$ GeV². The uncertainties are quoted in % relative to σ_r . δ_{tot} is the total uncertainty determined as the quadratic sum of systematic and statistical uncertainties. δ_{stat} is the statistical uncertainty. δ_{uncor} represents the uncorrelated systematic uncertainty. $\gamma_{E'_e}$, γ_{θ_e} , $\gamma_{E_{\text{had}}}$, γ_{noise} , $\gamma_{E_{\text{SpaCal}}^h}$ and $\gamma_{\gamma p}$ are the bin-to-bin correlated systematic uncertainties in the cross section measurement due to uncertainties in the SpaCal electromagnetic energy scale, electron scattering angle, LAr calorimeter hadronic energy scale, LAr calorimeter noise, SpaCal hadronic energy scale and the photoproduction background, respectively. The luminosity uncertainty of 1.1% for the NVX data is not included in δ_{tot} .

Q^2 GeV ²	x	y	σ_r	δ_{tot} %	δ_{stat} %	δ_{uncor} %	$\gamma_{E'_e}$ %	γ_{θ_e} %	$\gamma_{E_{\text{had}}}$ %	γ_{noise} %	$\gamma_{E_{\text{SpaCal}}^h}$ %	$\gamma_{\gamma p}$ %
1.50	1.853×10^{-5}	8.000×10^{-1}	0.605	12.0	3.18	3.48	0.49	0.81	-0.02	0.20	1.19	-10.97
2.00	2.470×10^{-5}	8.000×10^{-1}	0.756	9.23	2.35	2.70	-1.47	1.36	-0.03	0.12	2.15	-7.98
2.50	3.088×10^{-5}	8.000×10^{-1}	0.837	7.11	2.46	2.67	-1.17	-0.44	-0.05	0.21	0.12	-5.98
3.50	4.323×10^{-5}	8.000×10^{-1}	0.871	7.99	3.10	2.83	-0.86	-0.56	0.62	-0.04	2.32	-6.28
5.00	6.176×10^{-5}	8.000×10^{-1}	0.993	7.70	3.12	2.78	-1.70	-0.72	-0.72	0.14	0.50	-6.13
6.50	8.029×10^{-5}	8.000×10^{-1}	1.080	6.42	3.11	2.64	-0.55	0.91	0.00	-0.46	-1.62	-4.54
8.50	1.050×10^{-4}	8.000×10^{-1}	1.174	6.22	3.73	2.80	-0.28	1.06	-0.89	0.00	-1.12	-3.71

Table 14: Reduced cross section σ_r , as measured with the NVX-S9 data sample. The uncertainties are quoted in % relative to σ_r . δ_{tot} is the total uncertainty determined as the quadratic sum of systematic and statistical uncertainties. δ_{stat} is the statistical uncertainty. δ_{uncor} represents the uncorrelated systematic uncertainty. $\gamma_{E'_e}$, γ_{θ_e} , $\gamma_{E_{\text{had}}}$, γ_{noise} , $\gamma_{E_{\text{SpaCal}}^h}$ and $\gamma_{\gamma p}$ are the bin-to-bin correlated systematic uncertainties in the cross section measurement due to uncertainties in the SpaCal electromagnetic energy scale, electron scattering angle, LAr calorimeter hadronic energy scale, LAr calorimeter noise, SpaCal hadronic energy scale and the photoproduction background, respectively. The luminosity uncertainty of 1.1% for the NVX data is not included in δ_{tot} .

#	Q^2 GeV ²	x	y	F_L^{th}	σ_r^{ave}	F_2	$\delta_{\text{ave,stat}}$ %	$\delta_{\text{ave,uncor}}$ %	$\delta_{\text{ave,tot}}$ %	CME GeV
1	0.2	0.398×10^{-4}	0.050	0.08	0.230	0.230	14.3	12.0	19.98	319
2	0.2	0.251×10^{-3}	0.008	0.06	0.190	0.190	13.1	6.18	15.03	319
3	0.25	0.398×10^{-4}	0.062	0.09	0.300	0.300	9.84	11.3	16.82	319
4	0.25	0.251×10^{-3}	0.010	0.07	0.191	0.191	10.00	4.70	12.05	319
5	0.25	0.158×10^{-2}	0.002	0.06	0.203	0.203	10.8	5.29	12.37	301
6	0.35	0.512×10^{-5}	0.675	—	0.450	—	21.7	12.8	25.34	319
7	0.35	0.610×10^{-5}	0.634	—	0.357	—	5.74	11.0	13.50	301
8	0.35	0.320×10^{-4}	0.108	0.12	0.410	0.411	9.12	11.1	20.36	319
9	0.35	0.130×10^{-3}	0.027	0.10	0.264	0.264	9.62	4.38	10.99	319
10	0.35	0.500×10^{-3}	0.007	0.08	0.237	0.237	8.81	4.19	10.08	319
11	0.35	0.251×10^{-2}	0.001	0.07	0.204	0.204	9.93	4.55	11.08	319
12	0.5	0.732×10^{-5}	0.675	—	0.449	—	5.42	5.74	9.44	319
13	0.5	0.860×10^{-5}	0.642	—	0.442	—	3.75	9.17	10.69	301
14	0.5	0.158×10^{-4}	0.313	0.16	0.461	0.472	19.0	9.84	21.61	319
15	0.5	0.398×10^{-4}	0.124	0.15	0.478	0.480	10.1	6.07	16.25	319
16	0.5	0.100×10^{-3}	0.049	0.13	0.411	0.411	8.85	4.87	10.57	319
17	0.5	0.251×10^{-3}	0.020	0.11	0.296	0.296	8.37	4.20	9.74	319
18	0.5	0.800×10^{-3}	0.006	0.10	0.280	0.280	5.92	3.44	7.07	319
19	0.5	0.320×10^{-2}	0.002	0.08	0.183	0.183	11.4	6.39	13.12	301
20	0.65	0.952×10^{-5}	0.675	—	0.479	—	3.96	2.90	5.85	319
21	0.65	0.112×10^{-4}	0.641	—	0.504	—	3.74	8.21	9.89	301
22	0.65	0.158×10^{-4}	0.407	0.20	0.466	0.490	3.09	5.44	6.51	319
23	0.65	0.164×10^{-4}	0.438	0.19	0.510	0.538	3.02	7.28	8.33	301
24	0.65	0.398×10^{-4}	0.161	0.17	0.678	0.681	17.5	11.2	21.16	319
25	0.65	0.100×10^{-3}	0.064	0.15	0.500	0.500	5.14	5.84	10.70	319
26	0.65	0.251×10^{-3}	0.026	0.13	0.376	0.376	6.79	3.46	7.98	319
27	0.65	0.800×10^{-3}	0.008	0.11	0.308	0.308	4.94	3.02	6.17	319
28	0.65	0.320×10^{-2}	0.002	0.09	0.225	0.225	5.81	3.15	6.76	319
29	0.85	0.124×10^{-4}	0.675	—	0.565	—	2.54	2.52	4.50	319
30	0.85	0.138×10^{-4}	0.675	—	0.614	—	5.20	9.45	12.17	301
31	0.85	0.200×10^{-4}	0.420	0.22	0.612	0.641	1.96	5.36	5.99	319
32	0.85	0.200×10^{-4}	0.469	0.22	0.596	0.634	2.65	4.98	6.27	301
33	0.85	0.398×10^{-4}	0.211	0.20	0.567	0.573	1.65	3.39	4.13	319
34	0.85	0.500×10^{-4}	0.168	0.20	0.546	0.549	2.92	4.52	5.97	319
35	0.85	0.100×10^{-3}	0.084	0.18	0.499	0.500	2.78	3.59	5.98	319
36	0.85	0.251×10^{-3}	0.033	0.15	0.414	0.414	5.88	2.98	7.31	319
37	0.85	0.800×10^{-3}	0.010	0.13	0.350	0.350	4.61	2.66	5.60	319
38	0.85	0.320×10^{-2}	0.003	0.11	0.307	0.307	4.56	2.81	5.49	301
39	1.2	0.176×10^{-4}	0.675	—	0.608	—	2.54	2.14	4.65	319
40	1.2	0.200×10^{-4}	0.593	—	0.671	—	2.62	2.51	3.94	319
41	1.2	0.200×10^{-4}	0.663	—	0.741	—	3.60	8.36	9.98	301
42	1.2	0.320×10^{-4}	0.371	0.26	0.689	0.714	1.67	2.73	3.55	319
43	1.2	0.320×10^{-4}	0.414	0.26	0.705	0.738	2.68	4.55	5.83	301
44	1.2	0.631×10^{-4}	0.188	0.23	0.647	0.652	1.18	2.25	3.09	319
45	1.2	0.800×10^{-4}	0.148	0.22	0.594	0.597	2.18	4.02	5.24	319
46	1.2	0.130×10^{-3}	0.091	0.21	0.543	0.544	2.43	4.97	5.78	319
47	1.2	0.158×10^{-3}	0.075	0.20	0.503	0.504	1.67	2.30	3.24	319
48	1.2	0.398×10^{-3}	0.030	0.17	0.502	0.502	2.88	2.67	4.26	319
49	1.2	0.130×10^{-2}	0.009	0.14	0.374	0.374	3.58	2.62	4.74	319
50	1.2	0.500×10^{-2}	0.002	0.12	0.298	0.298	4.51	2.60	5.47	319
51	1.5	0.185×10^{-4}	0.800	—	0.610	—	3.17	3.48	7.93	319
52	1.5	0.220×10^{-4}	0.675	—	0.702	—	1.94	1.78	3.31	319
53	1.5	0.320×10^{-4}	0.463	0.29	0.756	0.804	1.77	2.12	3.08	319
54	1.5	0.320×10^{-4}	0.518	0.29	0.801	0.864	1.20	3.20	4.47	301
55	1.5	0.500×10^{-4}	0.296	0.27	0.759	0.775	1.06	1.97	2.62	319
56	1.5	0.800×10^{-4}	0.185	0.25	0.699	0.705	1.26	2.15	2.95	319
57	1.5	0.130×10^{-3}	0.114	0.23	0.643	0.644	1.49	2.42	3.32	319
58	1.5	0.200×10^{-3}	0.074	0.22	0.615	0.616	2.40	2.59	3.97	319
59	1.5	0.320×10^{-3}	0.046	0.20	0.584	0.584	1.60	2.18	3.30	319
60	1.5	0.500×10^{-3}	0.030	0.19	0.548	0.548	2.51	7.05	7.74	319
61	1.5	0.800×10^{-3}	0.019	0.17	0.495	0.495	2.35	2.47	3.80	319
62	1.5	0.100×10^{-2}	0.015	0.17	0.463	0.463	5.22	3.74	6.61	319
63	1.5	0.320×10^{-2}	0.005	0.14	0.409	0.409	2.32	2.03	3.51	301
64	1.5	0.130×10^{-1}	0.001	0.11	0.327	0.327	3.99	2.49	7.00	319

Table 15: Combined H1 reduced cross section σ_r^{ave} for $0.2 \leq Q^2 \leq 1.5 \text{ GeV}^2$. The uncertainties are quoted in % relative to σ_r^{ave} . F_L^{th} represents the structure function F_L used for the CME correction (equation 32) and to calculate the structure function F_2 . $\delta_{\text{ave,stat}}$ ($\delta_{\text{ave,uncor}}$) represents the statistical (uncorrelated systematic) uncertainty. $\delta_{\text{ave,tot}}$ is the total uncertainty calculated as a sum of uncorrelated uncertainty and all correlated sources in quadrature. A global normalisation uncertainty of 0.5% is not included in $\delta_{\text{ave,tot}}$. CME stands for the centre-of-mass energy of the measurement.

#	γ_1^{ave} ‰	γ_2^{ave} ‰	γ_3^{ave} ‰	γ_4^{ave} ‰	γ_5^{ave} ‰	γ_6^{ave} ‰	γ_7^{ave} ‰	γ_8^{ave} ‰	γ_9^{ave} ‰	γ_{10}^{ave} ‰	γ_{11}^{ave} ‰	γ_{12}^{ave} ‰	γ_{13}^{ave} ‰	γ_{14}^{ave} ‰	γ_{15}^{ave} ‰	γ_{16}^{ave} ‰	γ_{17}^{ave} ‰	γ_{18}^{ave} ‰	γ_{19}^{ave} ‰	γ_{20}^{ave} ‰	γ_{21}^{ave} ‰	γ_{22}^{ave} ‰	γ_{23}^{ave} ‰	γ_{24}^{ave} ‰	γ_{25}^{ave} ‰	γ_{26}^{ave} ‰
1	-8.47	4.05	13.89	-47.47	28.59	-29.31	8.41	9.60	11.37	0.70	2.45	10.13	4.13	4.53	-7.00	16.08	5.55	-2.12	5.17	-4.79	-1.39	0.57	3.25	-0.76	-1.67	6.96
2	-8.44	0.03	2.05	-16.70	4.06	3.02	8.85	4.87	-8.92	4.13	7.94	1.45	17.70	1.42	-13.72	-13.88	-0.90	1.39	-7.65	2.47	-9.60	-0.56	1.05	-1.06	-1.12	5.38
3	-8.46	5.18	15.49	-60.99	27.90	-21.88	11.74	5.01	3.26	2.87	4.43	8.68	9.12	2.88	-10.26	4.44	1.89	-3.94	2.73	-2.79	-3.82	0.68	2.74	-0.82	-1.69	7.03
4	-8.45	-1.19	1.31	-12.83	11.91	-7.49	20.51	8.35	-7.96	-2.77	22.68	-11.42	11.97	-7.76	-6.84	-12.41	0.96	2.99	-8.42	3.25	-10.50	-1.33	2.29	-1.41	-1.41	6.91
5	-8.46	-1.54	-0.42	-4.36	-2.37	8.37	2.08	9.28	-6.33	2.73	6.68	-1.39	10.58	-1.36	-7.56	-11.91	0.62	1.23	-5.17	1.79	-4.26	-0.14	0.76	-0.69	-0.87	4.36
6	-8.45	1.47	4.81	-19.08	3.08	1.98	-1.34	3.89	0.63	4.12	-1.29	2.26	-4.14	-1.06	-1.34	-0.65	1.81	-2.91	2.88	-1.95	1.69	0.89	1.76	-0.02	-1.03	4.82
7	-8.66	19.34	9.32	4.74	8.68	7.41	-10.14	-4.02	-0.07	0.70	26.17	10.09	-11.30	25.55	5.77	-5.90	1.03	-1.40	-1.20	1.14	0.98	6.38	7.17	-15.10	2.23	-1.74
8	-8.42	7.01	28.05	-123.68	41.80	-15.78	17.04	18.13	-7.89	-1.98	22.54	-2.54	22.13	-12.02	-7.29	-21.45	-2.31	-11.93	4.21	0.70	4.74	2.76	0.80	-0.93	-1.77	6.19
9	-8.46	0.28	4.59	-17.69	9.30	-6.18	5.69	10.17	0.15	1.78	6.25	0.08	-4.02	-1.68	-5.16	7.06	1.47	0.40	0.05	-2.06	-7.68	-1.15	3.32	-0.83	-1.23	6.19
10	-8.46	0.26	0.04	-5.57	2.86	0.54	11.44	-1.48	-6.32	3.04	8.08	-3.79	4.03	-2.11	-6.41	-8.73	0.29	1.19	-5.28	1.42	-8.00	-0.65	2.12	-0.71	-1.22	6.19
11	-8.47	-0.34	-0.56	-0.84	0.85	1.46	7.59	1.31	-3.73	2.29	6.72	-4.19	-0.09	-2.91	-3.31	-5.60	1.41	1.01	-3.33	0.59	-5.04	-0.41	2.10	-0.52	-1.12	5.73
12	-8.44	0.29	9.73	-35.80	6.26	3.70	-10.82	23.30	2.89	2.91	-0.79	4.32	-13.10	-3.38	-0.91	13.08	0.79	-4.09	7.84	-5.04	0.10	-0.19	2.90	-0.32	-0.84	4.16
13	-8.66	21.09	3.43	2.40	0.05	1.81	-4.02	-3.78	0.51	0.33	20.31	9.38	-7.66	15.14	2.38	-7.80	4.12	-1.96	-0.15	-6.68	1.36	-7.56	1.17	-8.39	1.49	-1.27
14	-8.48	3.46	0.47	-0.95	2.62	-4.76	11.15	-19.63	1.55	3.96	-0.89	-4.72	-11.40	-3.11	5.69	-5.85	3.61	-2.83	1.84	-0.76	4.21	1.70	2.20	0.56	-1.39	6.60
15	-8.43	4.57	21.52	-96.02	29.98	-7.24	11.43	18.94	-7.85	-1.25	19.35	-4.28	13.28	-11.98	-4.93	-16.82	-2.15	-9.41	3.50	0.34	2.78	1.81	1.20	-0.81	-1.49	5.64
16	-8.47	-0.86	3.21	-14.11	7.55	-4.49	3.90	13.42	1.00	-1.32	9.85	-1.87	13.02	-2.64	-3.47	-8.49	4.41	0.24	-1.94	0.79	2.78	1.05	0.52	-0.60	-1.05	4.50
17	-8.47	0.90	1.81	-10.87	6.19	-4.16	10.70	-1.34	-3.16	2.24	4.90	-0.34	7.40	1.23	-4.87	-5.96	-0.04	7.70	-5.29	-1.76	-8.17	-0.62	5.40	0.89	0.46	4.72
18	-8.46	-0.12	-0.41	-1.73	0.12	2.30	6.67	0.72	-6.06	6.10	4.41	-0.39	-2.26	-0.93	-6.12	-0.98	-0.77	4.02	-2.33	-0.09	-3.58	-0.06	0.94	0.06	0.31	3.43
19	-8.48	-0.13	0.14	1.36	1.68	-3.36	1.87	2.48	2.66	2.81	0.02	0.58	-0.46	0.58	-1.66	-4.41	1.11	0.75	2.51	-0.03	-0.55	-0.28	5.49	3.61	4.55	-0.73
20	-8.45	0.84	5.86	-22.11	3.12	3.62	-4.22	10.18	1.17	3.16	-0.05	0.34	-11.86	-4.00	1.27	4.83	1.37	-3.47	5.19	-3.16	1.36	0.38	2.47	-0.04	-0.96	4.73
21	-8.65	20.32	3.93	2.78	2.24	3.05	-5.19	-3.74	0.38	0.55	20.73	9.06	-8.13	16.77	2.97	-7.18	3.44	-1.80	-0.34	-4.92	1.25	-4.46	2.44	-9.73	1.63	-1.36
22	-8.47	2.20	1.96	-7.04	1.11	-0.54	2.14	-6.90	1.55	5.53	-4.53	3.52	-2.39	2.13	-1.85	-2.62	2.79	-1.88	1.19	-1.35	1.67	1.22	1.57	0.16	-1.13	5.29
23	-8.60	17.09	-8.57	-1.73	-3.98	-1.64	0.24	-1.41	1.38	2.84	5.70	2.20	-3.48	4.08	-0.37	-3.64	3.89	-0.68	0.22	-2.30	0.72	0.31	4.07	-11.34	1.74	-1.56
24	-8.47	-1.45	-0.74	1.62	0.81	2.74	8.57	5.51	-1.63	-4.27	16.47	-20.04	-17.65	-17.26	13.57	-7.04	3.48	-1.72	2.01	0.29	5.31	0.52	2.48	0.08	-1.08	5.62
25	-8.47	2.45	6.38	-31.57	23.73	-22.45	25.69	-2.50	-1.25	-4.12	20.69	-6.10	33.65	-3.25	-6.44	-26.34	5.80	-0.20	-7.40	4.79	4.15	2.58	-0.51	-0.84	-1.72	6.54
26	-8.47	0.69	1.95	-10.69	5.12	-2.52	8.31	1.20	-2.17	2.61	5.27	-1.29	6.70	0.25	-4.87	-7.55	3.59	4.91	-3.17	-0.93	3.90	1.35	3.44	1.90	1.61	2.75
27	-8.47	-0.53	-0.73	0.23	1.70	0.53	9.59	2.56	-4.82	2.94	6.83	-4.26	-7.21	-2.28	-7.14	-0.15	-1.88	3.65	-1.02	0.16	-6.45	-0.93	2.24	0.34	0.86	3.38
28	-8.47	-0.35	-0.56	0.36	-0.63	2.74	4.23	1.95	-1.82	0.93	3.68	-2.31	-2.55	-1.35	-4.59	-2.15	0.31	1.73	1.17	-0.82	5.09	1.38	0.84	1.12	1.28	1.51
29	-8.45	1.53	5.16	-18.70	3.31	1.29	-2.22	4.47	1.99	3.96	-1.96	1.47	-11.17	-2.20	0.92	4.49	1.87	-3.25	4.75	-3.07	1.44	0.59	2.45	0.05	-1.04	5.06
30	-8.70	23.84	10.36	5.53	6.16	5.84	-9.16	-5.70	0.01	-1.55	30.75	15.38	-12.02	23.47	4.49	-9.88	3.79	-2.20	-0.78	-6.07	1.57	-6.03	2.46	-10.56	1.81	-1.45
31	-8.47	2.26	1.04	-3.27	0.34	-0.80	3.24	-9.51	1.66	5.48	-4.58	2.61	-3.13	1.92	-0.93	-3.44	3.08	-1.71	0.93	-1.14	2.10	1.32	1.56	0.24	-1.15	5.42
32	-8.61	18.05	-7.99	-1.01	-1.26	-0.16	-0.97	-1.35	0.94	2.93	7.86	1.83	-3.62	7.39	0.73	-3.78	3.22	-1.06	0.16	-2.86	0.79	-1.16	3.13	-9.74	1.53	-1.36
33	-8.48	4.42	-1.99	-0.46	-0.97	-0.59	2.40	-5.61	1.56	3.93	-1.05	1.99	-2.33	0.01	-1.63	-3.62	4.04	-0.48	0.25	-0.76	1.14	2.56	3.85	-7.64	0.64	1.30
34	-8.47	-0.30	2.10	0.44	-3.54	-1.65	3.26	-4.98	2.41	1.35	-0.36	6.63	-3.37	-9.21	-5.03	-4.90	7.60	0.55	0.67	-3.16	0.67	0.65	5.53	-15.11	2.29	-2.13
35	-8.47	0.31	4.11	-5.19	-6.12	1.27	1.30	5.71	-0.09	12.30	-5.40	-16.02	-0.58	17.29	6.25	5.63	-3.93	3.08	-2.00	9.65	-0.45	16.99	7.93	-6.56	1.04	1.00
36	-8.47	0.70	1.64	-10.06	6.23	-4.71	9.66	0.29	-1.57	1.96	5.60	0.03	16.26	2.56	-7.16	-13.29	4.58	5.94	-6.66	1.56	2.20	1.15	1.81	1.22	1.08	2.73
37	-8.47	-0.07	0.12	-2.35	1.87	-0.19	7.08	1.88	-3.63	4.38	4.05	-0.74	-3.24	0.11	-6.71	0.99	0.65	4.88	-3.20	0.43	-4.44	-0.60	1.12	0.15	0.54	3.08
38	-8.47	0.36	0.10	1.05	1.75	-3.55	2.87	-0.56	2.01	2.88	-0.51	2.68	0.72	2.00	-3.79	-0.34	1.29	0.86	0.55	0.04	-0.93	0.21	1.36	0.75	0.95	2.14
39	-8.45	2.26	6.77	-24.90	4.39	1.50	-2.50	3.92	2.41	4.89	-3.89	1.71	-12.77	-0.87	0.71	4.36	4.00	-0.73	1.74	-1.45	1.19	-0.02	1.97	0.46	-0.33	3.85
40	-8.46	0.65	1.86	-6.42	-0.75	3.25	-1.89	2.34	1.30	4.00	-2.04	1.28	-5.72	-0.73	-0.22	-0.07	2.54	-1.65	2.11	-1.76	1.69	0.75	1.74	0.05	-0.96	4.72
41	-8.65	19.02	3.66	3.59	5.94	4.61	-6.00	-4.30	0.16	0.33	20.90	9.48	-8.11	16.48	2.88	-7.48	3.63	-1.84	-0.29	-5.55	1.28	-5.67	1.86	-8.97	1.54	-1.29
42	-8.47	1.68	1.25	-4.31	0.72	-0.48	2.54	-5.52	1.46	4.70	-2.90	2.12	-2.03	1.26	-1.32	-3.13	3.06	-1.39	0.71	-1.06	1.71	1.13	1.53	0.11	-1.11	5.25
43	-8.58	13.51	-6.83	-1.18	-1.40	-0.20	-0.45	-1.46	1.28	3.32	4.69	1.21	-3.48	4.63	-0.05	-2.66	3.21	-0.40	0.09	-0.24	0.55	3.91	5.50	-12.79	1.88	-1.66
44	-8.47	2.22	0.22	0.06	-1.15	-1.11	4.10	-9.48	1.56	4.51	-3.05	2.71	-3.06	-0.46	-1.70	-4.29	4.16	-0.91	0.41	-1.56	1.40	0.86	2.51	-3.84	-0.21	3.32
45	-8.47	-1.72	1.85	0.72	1.37	1.19	0.80	-3.89	1.92	2.81	-0.58	3.26	-3.55	-3.91	-2.92	-2.39	5.00	0.80	0.22	1.74	0.32	8.73	8.37	-17.40	2.47	-2.21
46	-8.47	-0.17	1.27	-0.73	-1.94	-0.14	4.34	0.00	0.50	6.35	-2.71	-8.02	2.23	3.73	0.48	-0.47	1.76	-1.37	0.86	-3.27	0.54	-3.55	0.52	-4.62	0.76	-0.79
47	-8.47	0.91	0.45	-0.64	-0.55	0.22	2.09	-3.37	0.86	6.94	-5.11	2.27	-0.47	4.82	-3.90	-0.38	2.49	1.82	-0.81	-1.70	-1.85	0.01	2.70	-1.26	0.15	3.21
48	-8.47	-0.39	-0.73	-1.57	3.31	1																				

#	Q^2 GeV ²	x	y	F_L^{th}	σ_r^{ave}	F_2	$\delta_{\text{ave,stat}}$ %	$\delta_{\text{ave,uncor}}$ %	$\delta_{\text{ave,tot}}$ %	CME GeV
65	2.0	0.247×10^{-4}	0.800	—	0.775	—	2.32	2.70	6.03	319
66	2.0	0.293×10^{-4}	0.675	—	0.792	—	1.49	1.65	2.86	319
67	2.0	0.327×10^{-4}	0.675	—	0.839	—	1.82	5.21	6.34	301
68	2.0	0.500×10^{-4}	0.395	0.32	0.825	0.861	1.61	1.86	2.71	319
69	2.0	0.500×10^{-4}	0.442	0.32	0.856	0.903	0.92	2.45	3.00	301
70	2.0	0.800×10^{-4}	0.247	0.29	0.768	0.780	0.91	1.64	2.19	319
71	2.0	0.130×10^{-3}	0.152	0.27	0.726	0.730	1.05	1.69	2.32	319
72	2.0	0.200×10^{-3}	0.099	0.25	0.679	0.680	1.09	1.78	2.51	319
73	2.0	0.320×10^{-3}	0.062	0.23	0.634	0.635	1.15	1.55	2.49	319
74	2.0	0.500×10^{-3}	0.040	0.21	0.578	0.578	1.33	1.94	2.83	319
75	2.0	0.100×10^{-2}	0.020	0.19	0.510	0.510	1.15	1.69	2.42	319
76	2.0	0.320×10^{-2}	0.006	0.15	0.424	0.424	1.26	1.78	2.77	319
77	2.0	0.130×10^{-1}	0.002	0.12	0.361	0.361	2.40	2.11	5.34	301
78	2.5	0.309×10^{-4}	0.800	—	0.835	—	2.46	2.67	5.06	319
79	2.5	0.366×10^{-4}	0.675	—	0.860	—	2.29	2.29	3.74	319
80	2.5	0.409×10^{-4}	0.675	—	0.920	—	1.56	6.21	6.98	301
81	2.5	0.500×10^{-4}	0.494	0.35	0.861	0.930	1.51	1.65	2.51	319
82	2.5	0.500×10^{-4}	0.552	0.35	0.895	0.984	1.20	2.09	3.13	301
83	2.5	0.800×10^{-4}	0.309	0.32	0.856	0.877	0.69	1.17	1.72	319
84	2.5	0.130×10^{-3}	0.190	0.30	0.795	0.801	0.73	1.14	1.73	319
85	2.5	0.200×10^{-3}	0.124	0.27	0.758	0.760	0.92	1.53	2.09	319
86	2.5	0.320×10^{-3}	0.077	0.25	0.671	0.672	0.92	1.68	2.28	319
87	2.5	0.500×10^{-3}	0.049	0.23	0.630	0.631	0.90	1.39	2.09	319
88	2.5	0.800×10^{-3}	0.031	0.21	0.578	0.578	1.02	1.77	2.30	319
89	2.5	0.158×10^{-2}	0.016	0.19	0.534	0.534	0.87	1.54	2.13	319
90	2.5	0.500×10^{-2}	0.005	0.16	0.439	0.439	1.01	1.69	2.59	319
91	2.5	0.200×10^{-1}	0.001	0.12	0.342	0.342	2.52	2.45	8.69	319
92	3.5	0.432×10^{-4}	0.800	—	0.877	—	3.09	2.83	5.75	319
93	3.5	0.512×10^{-4}	0.675	—	0.940	—	2.16	2.25	3.61	319
94	3.5	0.573×10^{-4}	0.675	—	0.931	—	2.00	6.18	6.94	301
95	3.5	0.800×10^{-4}	0.432	0.38	0.954	1.007	1.29	1.64	2.33	319
96	3.5	0.800×10^{-4}	0.483	0.38	0.950	1.020	1.00	1.75	2.67	301
97	3.5	0.130×10^{-3}	0.266	0.35	0.918	0.934	0.66	1.06	1.60	319
98	3.5	0.200×10^{-3}	0.173	0.32	0.859	0.865	0.69	1.07	1.64	319
99	3.5	0.320×10^{-3}	0.108	0.29	0.800	0.802	0.74	1.12	1.70	319
100	3.5	0.500×10^{-3}	0.069	0.27	0.759	0.760	0.83	1.31	1.91	319
101	3.5	0.800×10^{-3}	0.043	0.25	0.661	0.662	0.69	1.15	1.71	319
102	3.5	0.130×10^{-2}	0.027	0.22	0.626	0.626	0.89	1.36	1.98	319
103	3.5	0.251×10^{-2}	0.014	0.20	0.556	0.556	0.64	1.11	1.69	319
104	3.5	0.800×10^{-2}	0.004	0.16	0.448	0.448	0.84	1.48	2.32	319
105	5.0	0.618×10^{-4}	0.800	—	0.990	—	3.13	2.78	5.61	319
106	5.0	0.732×10^{-4}	0.675	—	1.056	—	1.60	2.21	3.02	319
107	5.0	0.818×10^{-4}	0.675	—	1.047	—	2.08	4.85	6.07	301
108	5.0	0.130×10^{-3}	0.380	0.41	1.066	1.108	1.33	2.20	2.76	319
109	5.0	0.130×10^{-3}	0.425	0.41	1.053	1.108	1.02	1.68	2.28	301
110	5.0	0.200×10^{-3}	0.247	0.37	1.011	1.025	0.74	1.19	1.75	319
111	5.0	0.320×10^{-3}	0.154	0.34	0.931	0.936	0.80	1.28	1.81	319
112	5.0	0.500×10^{-3}	0.099	0.31	0.839	0.841	0.80	1.28	1.83	319
113	5.0	0.800×10^{-3}	0.062	0.28	0.753	0.754	0.82	1.29	1.84	319
114	5.0	0.130×10^{-2}	0.038	0.25	0.696	0.696	0.85	1.31	1.93	319
115	5.0	0.200×10^{-2}	0.025	0.23	0.639	0.639	0.88	1.31	1.89	319
116	5.0	0.398×10^{-2}	0.012	0.20	0.569	0.569	0.67	1.22	1.81	319
117	5.0	0.130×10^{-1}	0.004	0.16	0.438	0.438	0.80	1.82	2.60	319

Table 17: Combined H1 reduced cross section σ_r^{ave} for $2 \leq Q^2 \leq 5$ GeV². The uncertainties are quoted in % relative to σ_r^{ave} . F_L^{th} represents the structure function F_L used for the CME correction (equation 32) and to calculate the structure function F_2 . $\delta_{\text{ave,stat}}$ ($\delta_{\text{ave,uncor}}$) represents the statistical (uncorrelated systematic) uncertainty. $\delta_{\text{ave,tot}}$ is the total uncertainty calculated as a sum of uncorrelated uncertainty and all correlated sources in quadrature. A global normalisation uncertainty of 0.5% is not included in $\delta_{\text{ave,tot}}$. CME stands for the centre-of-mass energy of the measurement.

#	γ_1^{ave} ‰	γ_2^{ave} ‰	γ_3^{ave} ‰	γ_4^{ave} ‰	γ_5^{ave} ‰	γ_6^{ave} ‰	γ_7^{ave} ‰	γ_8^{ave} ‰	γ_9^{ave} ‰	γ_{10}^{ave} ‰	γ_{11}^{ave} ‰	γ_{12}^{ave} ‰	γ_{13}^{ave} ‰	γ_{14}^{ave} ‰	γ_{15}^{ave} ‰	γ_{16}^{ave} ‰	γ_{17}^{ave} ‰	γ_{18}^{ave} ‰	γ_{19}^{ave} ‰	γ_{20}^{ave} ‰	γ_{21}^{ave} ‰	γ_{22}^{ave} ‰	γ_{23}^{ave} ‰	γ_{24}^{ave} ‰	γ_{25}^{ave} ‰	γ_{26}^{ave} ‰
65	-8.45	2.93	7.08	-22.67	2.14	2.65	-4.10	1.48	7.64	6.42	-10.74	-2.44	-15.86	4.69	6.62	-1.76	17.36	20.72	-18.15	8.18	0.83	-3.09	-2.60	1.13	1.51	-1.28
66	-8.46	1.33	3.06	-10.30	1.08	0.83	-1.52	0.18	2.05	4.65	-3.35	1.92	-6.78	0.40	1.43	2.12	4.52	2.63	-2.21	0.96	0.72	-0.23	-0.17	0.24	0.12	2.09
67	-8.65	16.65	17.02	5.22	2.96	3.20	-6.82	-4.37	-1.78	2.03	10.40	-1.38	-1.14	5.29	-1.14	-2.75	6.23	0.05	2.70	-4.25	-1.60	-1.02	-0.99	0.12	-1.15	-1.24
68	-8.47	0.51	0.65	-1.95	-0.57	1.64	0.76	-0.14	1.56	2.16	-0.82	0.04	-3.32	-0.02	-1.30	-1.36	3.29	-0.85	-0.36	0.05	1.04	0.38	1.06	0.21	-0.38	3.60
69	-8.55	7.89	3.89	1.58	0.45	0.84	-0.63	-1.59	1.39	3.68	2.72	-1.41	-0.21	-1.15	-2.14	-1.17	3.86	0.10	1.32	-1.87	-1.05	1.15	0.79	-0.67	-1.62	-1.44
70	-8.47	0.29	0.06	0.20	-0.62	1.17	0.34	-0.02	1.94	3.44	1.87	-1.11	-1.63	-0.91	-1.12	-1.82	3.91	-0.22	0.77	-1.59	-0.14	1.76	1.19	-0.93	-1.17	1.18
71	-8.48	-0.25	0.08	0.44	-0.88	0.85	0.73	0.05	2.18	2.91	2.36	-0.77	-2.56	-2.39	-0.97	-2.05	4.09	-0.10	0.73	-1.40	0.21	1.81	1.80	-1.99	-0.98	1.24
72	-8.47	0.16	-0.51	0.96	1.08	2.02	5.83	1.96	2.61	2.94	1.53	-1.69	-3.07	-0.72	1.12	-2.69	4.57	-1.37	0.22	-3.61	-0.41	1.60	-0.30	0.52	-1.16	1.44
73	-8.48	-0.37	-0.63	0.31	1.69	-0.33	5.39	1.71	0.26	2.97	3.01	-1.17	4.00	-0.09	-1.66	-6.90	4.42	-0.49	-1.35	-3.44	-0.12	0.98	3.73	2.24	1.41	0.82
74	-8.47	-0.47	-0.32	-0.37	-1.67	2.06	5.90	2.25	-3.24	0.19	2.24	-2.87	-0.09	-0.49	0.66	-5.59	7.25	-0.63	1.17	-3.24	-1.27	2.32	-1.16	0.51	-0.81	1.66
75	-8.47	-0.29	-0.14	0.98	1.20	-1.16	4.49	2.88	-0.96	0.63	1.95	-1.65	-3.14	-0.88	-0.38	-2.68	2.98	-0.12	-1.16	-2.96	-2.42	2.35	0.26	0.50	-0.61	2.04
76	-8.47	-0.33	0.09	2.89	3.92	-6.03	5.98	4.75	0.86	1.99	2.92	-1.63	-6.35	-1.01	-2.15	1.35	2.32	0.15	-1.26	-2.56	-3.68	1.33	0.86	0.25	-0.08	3.28
77	-8.48	0.07	2.19	3.47	2.59	-10.31	-12.26	7.77	19.82	-3.09	-6.44	4.04	7.82	1.01	12.15	-5.37	12.20	-4.28	7.70	-0.94	21.83	3.98	-0.54	1.37	-0.07	1.41
78	-8.46	1.84	4.77	-15.40	1.73	0.03	-3.07	1.02	2.68	10.09	-6.20	0.94	-8.09	1.38	9.33	-2.03	10.32	17.91	-11.40	3.73	0.30	-1.69	0.22	1.89	2.49	-0.99
79	-8.46	0.95	2.36	-7.68	0.57	0.27	-1.35	-0.25	1.32	4.95	-2.34	1.21	-4.60	-0.10	4.38	0.60	4.61	8.20	-5.85	3.24	0.20	-0.77	-2.25	0.22	0.96	-0.36
80	-8.64	17.04	12.77	4.46	2.83	2.62	-3.61	-2.45	-0.89	2.96	1.25	-5.00	1.58	-4.23	-3.60	-0.61	7.65	0.83	3.12	-3.02	-3.04	4.20	-0.90	1.61	-1.91	-1.54
81	-8.46	0.48	1.22	-3.92	0.06	0.76	-0.26	0.52	0.84	3.33	-0.36	0.94	-3.77	-0.95	0.89	0.99	2.95	0.39	-0.97	0.77	0.69	0.06	0.01	0.21	0.23	2.09
82	-8.59	9.90	7.63	2.40	0.93	3.54	-1.07	-2.87	5.04	5.59	4.95	-1.84	0.45	-2.31	-3.08	-0.81	4.43	0.41	1.82	-2.15	-1.60	1.44	0.32	1.12	-2.45	-1.66
83	-8.46	1.55	1.07	0.01	-0.14	0.78	0.21	-0.91	2.11	2.91	1.61	-0.53	-1.10	-0.54	-1.58	-0.79	3.08	-0.38	0.43	-0.47	-0.19	1.07	0.56	0.28	-0.99	0.23
84	-8.47	-0.12	0.15	0.11	-0.34	0.21	0.21	-0.49	1.38	2.00	1.57	-0.86	-1.82	-0.22	-2.04	-1.37	4.35	-0.87	0.42	-0.98	-0.58	2.08	0.71	-0.10	-0.99	0.06
85	-8.47	0.22	0.25	0.70	0.06	0.52	2.87	0.28	1.95	1.95	0.76	-0.14	-2.89	-1.40	-1.25	-1.72	2.67	-0.90	-0.17	-0.19	0.78	0.55	1.90	-1.12	-1.00	1.13
86	-8.47	0.08	-0.51	0.77	1.19	0.58	4.35	-1.09	1.71	2.94	2.50	-2.13	-3.54	-1.85	1.27	-1.74	2.13	-0.52	0.71	-0.37	1.17	0.11	1.77	-0.05	-1.71	1.65
87	-8.47	-0.19	-0.38	0.57	-0.28	0.05	2.86	0.85	-0.35	2.72	0.87	0.35	2.83	0.70	-2.13	-3.04	3.35	-1.30	-0.27	-1.59	-0.38	-0.84	5.00	2.56	1.34	0.57
88	-8.47	-0.25	-0.28	0.51	-0.51	0.91	3.21	1.90	0.29	2.93	0.93	0.63	-0.17	-0.01	-1.66	-1.53	2.45	0.04	-0.07	-0.97	-0.78	-0.27	1.07	0.25	-1.62	1.44
89	-8.47	-0.17	-0.31	0.79	0.53	0.32	4.24	2.12	0.33	2.35	1.30	0.74	-2.17	0.31	-2.83	0.26	2.68	-0.80	-1.18	-0.20	-2.92	0.03	1.96	0.63	-0.88	1.66
90	-8.48	-0.14	0.31	2.92	3.92	-6.34	4.30	4.82	4.73	3.28	0.90	1.01	-4.45	1.01	-4.64	2.25	2.39	-0.56	-1.40	-1.27	-2.03	0.64	1.12	0.38	-0.23	2.73
91	-8.51	-0.05	3.62	5.10	2.44	-14.55	-24.91	14.68	31.99	-5.24	-13.43	11.07	19.11	5.27	16.83	-5.88	20.59	-5.17	13.72	-3.40	48.22	9.22	-4.88	1.94	-0.51	-0.65
92	-8.45	2.27	5.42	-18.65	0.50	2.91	-4.76	-1.17	2.95	7.20	-7.19	0.58	-9.04	1.19	11.18	0.99	11.06	18.82	-14.80	5.01	0.50	-1.84	-3.66	-0.12	0.20	-0.68
93	-8.46	0.93	2.28	-7.45	0.45	0.50	-1.29	-0.36	1.29	4.59	-2.14	1.08	-4.62	-0.09	3.83	0.97	5.05	7.01	-6.05	3.52	0.23	-0.83	-2.28	0.22	0.97	-0.36
94	-8.62	14.45	11.11	3.86	2.27	0.47	-5.96	-3.19	-2.03	2.80	1.24	-4.45	1.66	-4.05	-3.88	0.08	5.06	1.25	2.79	-1.03	-1.71	2.13	0.34	1.27	-2.15	-1.33
95	-8.46	0.51	0.54	-1.60	-0.16	0.11	0.72	-1.61	0.40	3.28	-0.06	1.21	-2.02	-0.87	0.90	0.10	2.20	0.12	-0.90	0.94	0.65	0.23	-0.26	0.20	0.31	1.87
96	-8.55	8.15	6.46	2.97	2.19	-1.33	-1.15	0.34	-6.57	-0.64	-0.53	-1.98	-0.43	-0.30	-1.02	-1.50	5.67	0.01	1.92	-2.44	-1.93	2.64	-0.58	0.68	-1.32	-1.14
97	-8.46	0.45	0.45	0.25	-0.21	-0.25	0.26	-0.89	1.48	3.17	1.40	0.21	-0.75	-0.57	-1.26	-0.85	2.42	-0.34	0.36	-0.74	-0.34	0.85	0.38	0.41	-1.01	0.02
98	-8.47	-0.38	-0.20	0.03	-0.35	-0.01	0.35	-0.85	1.88	2.98	1.95	-0.16	-1.34	-0.72	-1.28	-0.90	2.75	-0.51	0.31	-0.49	-0.32	1.42	0.76	-0.01	-0.98	0.01
99	-8.47	0.04	0.10	0.80	0.60	-0.57	2.40	0.24	1.00	2.66	0.64	1.12	-2.14	-1.13	-1.21	-0.37	0.66	-1.14	-0.75	1.72	1.15	-0.39	2.18	-0.46	-1.08	0.26
100	-8.47	-0.18	-0.33	0.41	0.06	0.24	1.86	0.51	1.55	4.08	1.34	1.52	1.16	-0.32	-2.45	-1.01	-0.25	0.37	-0.48	0.96	0.46	-1.75	2.10	0.32	-2.32	0.35
101	-8.47	-0.29	-0.52	0.32	-0.40	0.43	1.67	-0.08	-2.43	1.47	1.20	0.91	1.19	0.55	-1.52	-0.51	2.95	-0.05	1.24	0.03	-0.74	-0.26	2.94	1.35	-0.03	0.12
102	-8.47	-0.03	-0.43	0.67	0.14	1.08	3.36	0.94	1.64	4.21	0.60	2.20	-0.18	0.05	-2.05	-0.41	-0.26	0.14	-0.52	0.70	-0.20	-1.09	2.18	0.31	-2.32	0.42
103	-8.47	-0.18	-0.37	0.72	0.48	-0.45	3.39	0.87	-0.43	2.59	1.47	1.43	-1.28	0.33	-2.77	1.08	1.78	0.08	0.34	1.03	-1.51	-0.62	1.96	0.68	-1.20	0.44
104	-8.48	-0.12	0.68	2.99	3.46	-7.43	0.68	5.19	4.35	3.65	-0.92	2.05	-3.06	1.30	-3.22	0.14	3.08	-1.61	0.05	0.10	-0.13	0.73	0.11	0.59	0.44	1.53
105	-8.46	1.80	4.92	-14.97	2.59	-1.94	-2.92	2.30	1.72	14.68	-5.70	1.97	-9.50	0.82	9.43	-2.10	11.20	17.94	-11.17	5.22	0.25	-1.82	-1.08	1.70	2.67	-0.99
106	-8.46	0.50	1.24	-4.03	0.10	0.05	-0.67	-0.67	0.33	3.67	-0.41	1.63	-2.41	-0.96	2.76	1.49	2.55	3.52	-3.39	2.73	0.06	-0.40	-2.26	0.00	0.83	-0.17
107	-8.66	19.06	14.15	5.00	3.27	3.75	-3.04	-2.46	0.80	3.95	1.40	-5.04	1.88	-5.00	-3.91	-0.38	7.23	0.85	2.97	-2.86	-2.95	4.10	-0.70	1.67	-2.10	-1.62
108	-8.46	0.04	0.14	-0.41	-0.13	-0.54	0.28	-0.74	-0.67	2.96	1.41	2.03	-0.01	-1.63	1.27	1.54	0.48	-0.21	-0.63	1.62	-0.07	-0.01	-1.03	0.39	1.29	-0.09
109	-8.51	2.68	2.06	0.99	0.37	-0.45	-0.48	-0.85	0.05	2.70	1.99	-0.99	-0.54	-1.07	-1.83	-1.01	3.54	0.06	1.14	-1.47	-1.32	1.98	0.36	1.11	-2.17	-1.38
110	-8.46	-0.04	0.00	0.10	-0.23	-0.48	0.02	-0.94	1.92	3.66	2.58	0.32	-0.60	-1.15	-1.10	-0.31	1.76	-0.26	0.36	-0.29	-0.74	1.08	0.20	0.90	-1.19	-1.02
111	-8.46	-0.05	-0.01	0.61	0.35	-1.54	0.83	0.12	-1.36	2.69	0.93	1.92	-0.43	-1.04	-0.39	0.65	-0.41	-0.39	-0.19	2.04	0.67	-1.07	1.36	0.55	-1.14	-0.75
112	-8.47	-0.17	-0.13	0.42	0.10	-1.25	0.56	-0.32	-0.92	3.65	1.67															

#	Q^2 GeV ²	x	y	F_L^{th}	σ_r^{ave}	F_2	$\delta_{\text{ave,stat}}$ %	$\delta_{\text{ave,uncor}}$ %	$\delta_{\text{ave,tot}}$ %	CME GeV
118	6.5	0.803×10^{-4}	0.800	—	1.083	—	3.11	2.64	4.85	319
119	6.5	0.951×10^{-4}	0.675	—	1.053	—	2.95	2.31	4.16	319
120	6.5	0.130×10^{-3}	0.494	0.45	1.123	1.211	1.67	2.22	2.97	319
121	6.5	0.130×10^{-3}	0.552	0.45	1.124	1.239	1.53	1.73	3.03	301
122	6.5	0.200×10^{-3}	0.321	0.41	1.123	1.152	1.25	2.20	2.72	319
123	6.5	0.200×10^{-3}	0.359	0.41	1.117	1.155	1.09	1.62	2.24	301
124	6.5	0.320×10^{-3}	0.201	0.37	1.006	1.015	0.84	1.16	1.75	319
125	6.5	0.500×10^{-3}	0.128	0.34	0.936	0.939	0.86	1.26	1.86	319
126	6.5	0.800×10^{-3}	0.080	0.31	0.854	0.855	0.87	1.26	1.91	319
127	6.5	0.130×10^{-2}	0.049	0.28	0.758	0.758	0.90	1.28	1.87	319
128	6.5	0.200×10^{-2}	0.032	0.26	0.694	0.694	0.92	1.29	1.89	319
129	6.5	0.398×10^{-2}	0.016	0.22	0.616	0.617	0.69	1.19	1.76	319
130	6.5	0.130×10^{-1}	0.005	0.18	0.482	0.482	0.73	1.80	2.44	319
131	8.5	0.105×10^{-3}	0.800	—	1.178	—	3.72	2.80	5.20	319
132	8.5	0.124×10^{-3}	0.675	—	1.211	—	2.26	2.28	3.44	319
133	8.5	0.139×10^{-3}	0.675	—	1.136	—	2.07	1.82	4.54	301
134	8.5	0.200×10^{-3}	0.420	0.46	1.178	1.239	1.52	2.22	2.88	319
135	8.5	0.200×10^{-3}	0.469	0.46	1.182	1.261	1.38	1.64	2.59	301
136	8.5	0.320×10^{-3}	0.262	0.41	1.112	1.131	0.91	1.25	1.86	319
137	8.5	0.500×10^{-3}	0.168	0.37	1.033	1.039	0.95	1.18	1.81	319
138	8.5	0.800×10^{-3}	0.105	0.34	0.950	0.953	0.95	1.28	1.90	319
139	8.5	0.130×10^{-2}	0.065	0.30	0.842	0.842	0.99	1.30	1.94	319
140	8.5	0.200×10^{-2}	0.042	0.28	0.773	0.773	1.00	1.30	1.93	319
141	8.5	0.320×10^{-2}	0.026	0.25	0.663	0.663	1.04	1.32	1.99	319
142	8.5	0.631×10^{-2}	0.013	0.22	0.604	0.604	0.79	1.24	1.83	319
143	8.5	0.200×10^{-1}	0.004	0.17	0.456	0.456	0.88	1.82	2.67	319
144	12.0	0.800×10^{-3}	0.148	0.38	1.053	1.058	1.07	1.30	1.99	319
145	12.0	0.130×10^{-2}	0.091	0.34	0.923	0.924	1.10	1.30	1.97	319
146	12.0	0.200×10^{-2}	0.059	0.31	0.861	0.861	1.11	1.33	2.00	319
147	12.0	0.320×10^{-2}	0.037	0.28	0.757	0.757	1.14	1.34	2.02	319
148	12.0	0.631×10^{-2}	0.019	0.24	0.646	0.646	0.88	1.24	1.86	319
149	12.0	0.200×10^{-1}	0.006	0.19	0.490	0.490	0.93	1.83	2.51	319

Table 19: Combined H1 reduced cross section σ_r^{ave} for $6.5 \leq Q^2 \leq 12 \text{ GeV}^2$. The uncertainties are quoted in % relative to σ_r^{ave} . F_L^{th} represents the structure function F_L used for the CME correction (equation 32) and to calculate the structure function F_2 . $\delta_{\text{ave,stat}}$ ($\delta_{\text{ave,uncor}}$) represents the statistical (uncorrelated systematic) uncertainty. $\delta_{\text{ave,tot}}$ is the total uncertainty calculated as a sum of uncorrelated uncertainty and all correlated sources in quadrature. A global normalisation uncertainty of 0.5% is not included in $\delta_{\text{ave,tot}}$. CME stands for the centre-of-mass energy of the measurement.

#	γ_1^{ave} ‰	γ_2^{ave} ‰	γ_3^{ave} ‰	γ_4^{ave} ‰	γ_5^{ave} ‰	γ_6^{ave} ‰	γ_7^{ave} ‰	γ_8^{ave} ‰	γ_9^{ave} ‰	γ_{10}^{ave} ‰	γ_{11}^{ave} ‰	γ_{12}^{ave} ‰	γ_{13}^{ave} ‰	γ_{14}^{ave} ‰	γ_{15}^{ave} ‰	γ_{16}^{ave} ‰	γ_{17}^{ave} ‰	γ_{18}^{ave} ‰	γ_{19}^{ave} ‰	γ_{20}^{ave} ‰	γ_{21}^{ave} ‰	γ_{22}^{ave} ‰	γ_{23}^{ave} ‰	γ_{24}^{ave} ‰	γ_{25}^{ave} ‰	γ_{26}^{ave} ‰
118	-8.46	1.37	3.17	-11.27	1.39	1.70	1.22	0.86	2.94	3.14	-4.40	-1.73	-7.26	3.19	0.65	-2.69	7.29	14.18	-7.90	1.22	1.47	-1.01	3.45	3.17	3.62	-1.11
119	-8.46	0.93	2.26	-7.40	0.54	0.40	-1.09	-0.24	1.49	4.29	-2.28	0.96	-4.56	0.08	3.74	0.48	4.45	7.88	-5.60	3.07	0.26	-0.74	-1.96	0.33	1.05	-0.37
120	-8.46	0.11	0.30	-1.03	-0.17	-0.41	0.00	-0.89	-0.86	3.43	1.27	2.20	-0.25	-1.76	1.91	1.85	0.70	0.43	-1.18	1.85	-0.04	-0.04	-1.59	0.15	1.05	-0.06
121	-8.59	10.47	7.68	2.70	1.52	2.48	-1.22	-1.95	1.85	4.01	2.36	-2.94	0.75	-3.10	-2.97	-0.64	5.55	0.49	2.18	-2.22	-2.23	3.14	-0.14	1.46	-2.26	-1.59
122	-8.46	0.01	0.08	-0.12	-0.06	-0.69	0.35	-0.60	-0.53	2.91	1.46	1.98	-0.03	-1.59	0.96	1.40	0.56	-0.69	-0.43	1.71	-0.11	-0.03	-0.89	0.47	1.39	-0.11
123	-8.50	1.34	1.04	0.58	0.03	-0.48	-0.36	-1.00	0.99	3.18	2.42	-0.64	-0.63	-0.98	-1.87	-0.91	2.88	0.06	0.93	-1.14	-1.05	1.60	0.65	1.07	-2.30	-1.39
124	-8.46	-0.45	-0.22	0.18	-0.13	-1.32	-0.10	-0.54	-0.01	2.96	2.05	0.49	-0.69	-0.83	-0.57	-0.43	2.06	-0.36	0.38	-0.49	-0.84	1.24	-0.05	0.83	-0.97	-0.93
125	-8.47	0.42	0.34	0.90	0.62	-1.60	0.89	0.28	-0.78	3.33	0.85	2.24	-0.29	-1.48	-0.21	0.78	-1.42	-0.30	-0.55	2.22	0.93	-1.36	1.57	0.48	-1.24	-0.72
126	-8.47	-0.16	-0.12	0.55	0.12	-1.64	0.40	-0.31	-2.32	4.68	1.84	2.28	-0.07	-1.54	-0.07	1.30	0.68	-0.91	-0.21	2.51	0.64	-1.14	1.36	0.68	-0.96	-0.79
127	-8.47	-0.15	-0.39	0.67	0.16	-0.34	2.57	-0.18	-1.07	1.93	1.56	1.46	-0.25	-0.56	-1.76	0.28	-1.50	1.45	1.07	0.88	0.99	-0.63	1.90	0.81	-1.09	-0.82
128	-8.47	-0.20	-0.55	-0.10	-0.69	0.95	2.17	-1.19	-2.02	0.46	1.55	1.40	0.82	-0.21	-0.21	0.48	0.35	1.92	2.57	1.03	0.19	-0.46	1.43	0.64	-1.41	-0.79
129	-8.47	-0.03	-0.42	0.92	0.64	0.12	4.65	1.14	-0.15	2.55	1.11	2.21	-1.06	-0.39	-1.29	-0.07	-0.97	0.94	1.13	1.29	0.67	-0.46	1.06	0.59	-1.42	-0.89
130	-8.48	-0.19	0.52	2.59	2.43	-6.37	-0.78	3.29	4.07	4.47	-0.50	1.58	-2.72	-0.82	-0.58	-3.79	-2.07	0.11	2.60	1.96	-1.09	-0.17	-0.54	0.50	0.44	-0.44
131	-8.47	1.14	2.93	-8.35	2.27	-0.86	0.79	2.55	5.45	2.64	-4.75	-1.59	-7.97	3.23	-0.57	-4.39	5.86	11.44	-4.64	2.62	0.47	-1.14	1.96	2.49	3.18	-0.93
132	-8.46	0.46	1.11	-3.62	0.02	0.09	-0.64	-0.79	0.37	3.16	-0.27	1.63	-2.11	-1.03	2.63	1.55	2.05	3.14	-2.99	2.60	0.02	-0.33	-2.38	-0.12	0.69	-0.12
133	-8.70	24.85	18.62	7.45	5.55	2.79	-3.21	-0.87	-2.55	2.64	-1.56	-4.85	2.24	-6.11	-3.80	0.10	5.30	0.87	2.28	-1.70	-2.06	2.95	-0.09	1.41	-2.01	-1.37
134	-8.46	0.06	0.15	-0.56	-0.20	-0.36	0.25	-0.85	-0.81	3.03	1.48	2.02	-0.12	-1.67	1.20	1.85	0.85	-0.55	-0.99	1.84	-0.02	-0.05	-1.19	0.34	1.25	-0.09
135	-8.54	6.02	4.54	1.91	1.12	0.06	-0.36	-0.51	-2.38	1.40	1.01	-1.83	-0.24	-1.17	-1.65	-1.24	5.60	0.13	1.95	-2.34	-2.10	3.03	-0.41	1.22	-1.85	-1.37
136	-8.46	-0.08	0.01	0.06	-0.27	-0.79	-0.14	-0.85	0.14	2.98	2.32	0.20	-0.56	-0.89	-0.58	-0.36	2.91	-0.49	0.52	-0.78	-1.14	1.65	-0.36	0.92	-0.76	-0.94
137	-8.47	-0.47	-0.26	0.05	-0.28	-0.98	-0.11	-0.77	0.43	2.90	2.22	0.42	-0.56	-0.87	-0.56	-0.38	2.06	-0.29	0.42	-0.59	-0.89	1.31	-0.08	0.84	-0.97	-0.93
138	-8.46	-0.09	-0.04	0.61	0.28	-1.64	0.72	0.02	-2.19	3.17	1.14	2.06	-0.30	-1.12	-0.16	0.86	0.21	-0.56	-0.04	2.19	0.58	-1.02	1.23	0.59	-0.96	-0.73
139	-8.47	-0.16	-0.30	0.73	0.15	-0.91	1.43	-0.57	-0.57	2.31	1.71	1.45	0.02	-1.04	-1.69	0.45	-2.85	1.74	0.66	0.83	1.28	-0.87	2.05	0.69	-1.16	-0.74
140	-8.47	-0.10	-0.33	0.45	-0.04	-0.10	1.94	-0.55	-0.27	1.66	1.39	1.69	0.22	-0.81	-0.93	0.46	-2.07	1.61	1.11	1.30	0.95	-1.02	1.87	0.56	-1.41	-0.75
141	-8.47	-0.19	-0.48	0.09	-0.50	0.27	2.12	-0.96	-3.53	0.28	1.36	1.30	0.36	0.03	-0.81	0.56	0.41	2.14	2.91	1.43	0.40	-0.58	1.13	0.54	-1.24	-0.71
142	-8.47	-0.12	-0.25	1.19	0.84	-1.51	2.91	1.00	-0.60	3.00	1.19	1.75	-1.40	-0.52	-1.95	-0.36	-1.55	1.29	1.41	1.41	0.74	-0.50	0.81	0.52	-1.18	-0.78
143	-8.48	-0.09	1.02	2.43	2.38	-7.17	-3.89	3.29	7.94	2.93	-2.21	1.91	-1.14	-1.44	3.37	-5.15	-2.86	-1.06	1.68	1.42	-2.33	-0.45	0.29	0.43	0.06	-0.41
144	-8.46	-0.12	0.11	0.51	0.13	-2.48	-0.89	-0.51	-3.53	2.40	0.95	1.63	-0.08	-1.08	-0.17	1.00	0.17	-0.34	0.07	2.24	0.63	-1.15	1.23	0.50	-0.84	-0.62
145	-8.47	-0.16	-0.21	0.95	0.40	-1.56	1.84	0.28	-2.89	0.39	0.73	1.01	-0.30	-0.15	-1.20	-0.50	-1.04	1.44	1.17	-0.44	0.46	0.25	1.48	0.89	-0.56	-0.71
146	-8.47	-0.04	-0.23	0.55	0.12	-0.47	2.03	-0.24	-1.47	0.84	0.92	1.60	0.03	-0.60	-0.86	0.41	-1.98	1.51	0.82	0.89	0.94	-0.74	1.61	0.53	-1.19	-0.68
147	-8.47	-0.16	-0.29	0.28	-0.23	-0.51	1.12	-0.89	-1.95	0.84	1.27	1.24	0.15	-0.43	-1.08	0.47	-1.05	1.87	1.91	1.49	0.71	-0.89	1.38	0.47	-1.28	-0.67
148	-8.47	-0.01	-0.31	0.96	0.65	-0.42	3.82	0.95	-0.55	2.02	0.85	2.12	-0.83	-0.48	-1.05	-0.10	-1.80	1.38	1.15	1.14	0.77	-0.54	1.05	0.47	-1.35	-0.77
149	-8.48	-0.07	0.66	2.34	2.22	-5.85	-1.40	3.01	5.28	2.94	-1.32	1.93	-1.56	-1.16	1.53	-3.92	-3.41	0.24	1.78	1.08	-1.30	-0.21	-0.08	0.33	0.03	-0.38

Table 20: Correlated systematic uncertainties given in per mill relative to the cross section measurement reported in table 19. The coefficients $\gamma_1^{\text{ave}}, \gamma_{26}^{\text{ave}}$ represent diagonalised correlated systematic uncertainties (see section 9.1).

	NVX							SVX							NVX-97							SVX-95						
	$b_{E'_e}$	b_{θ_e}	$b_{E_{\text{had}}}$	b_{noise}	$b_{E_{\text{SpaCal}}^{eh}}$	$b_{\gamma p}$	$b_{\mathcal{L}}$	$b_{E'_e}$	b_{θ_e}	$b_{E_{\text{had}}}$	b_{noise}	$b_{E_{\text{SpaCal}}^{eh}}$	$b_{\gamma p}$	$b_{\mathcal{L}}$	$b_{E'_e}$	b_{θ_e}	$b_{E_{\text{had}}}$	b_{noise}	$b_{\gamma p}$	$b_{\mathcal{L}}$	$b_{E'_e}$	b_{θ_e}	$b_{E_{\text{had}}}$	$b_{\gamma p}$	b_{dif}	$b_{\mathcal{L}}$		
δ_1	0.0	0.0	0.0	0.0	0.0	0.0	-77.0	0.0	0.0	0.0	0.0	0.0	0.0	-28.2	0.1	0.1	-0.1	0.1	0.6	-49.8	0.0	0.0	0.0	0.1	-0.4	-28.2		
δ_2	0.5	1.3	-1.1	0.5	1.3	-3.2	0.9	-2.6	-10.8	-0.5	0.0	1.9	-5.7	-2.3	3.0	2.4	-3.8	1.8	-69.0	-1.5	1.9	1.8	0.2	-0.6	70.8	0.0		
δ_3	0.6	1.7	0.7	4.3	2.7	-8.3	1.1	0.7	-1.2	2.4	2.2	0.4	-20.6	-0.3	3.2	4.8	0.8	-5.7	-52.5	1.2	-2.6	-8.5	-26.1	-54.5	-53.7	-5.2		
δ_4	-1.1	-4.5	14.6	1.2	-7.6	27.0	-5.4	-0.7	2.7	10.6	2.5	2.2	87.9	2.6	6.3	6.8	-8.3	-4.0	-21.3	6.8	-0.9	-0.7	13.2	-9.4	-12.2	-0.3		
δ_5	-0.3	0.6	14.5	1.9	-1.9	-3.9	-4.9	-9.1	-8.4	26.1	1.8	-21.6	-24.4	-10.7	7.3	8.2	-12.3	-5.2	-17.7	5.4	-0.8	20.1	76.7	10.3	-22.0	14.5		
δ_6	4.4	10.2	-29.0	-13.9	4.0	-1.2	6.2	10.7	22.1	-48.5	-9.6	28.9	5.2	17.2	-11.6	-25.1	-15.2	36.0	-15.4	-24.4	-0.8	11.5	32.6	-2.9	-13.4	9.1		
δ_7	-0.2	6.7	8.0	-27.6	-8.2	4.6	2.3	-27.8	-21.3	10.7	-16.7	-26.1	-0.6	-11.0	1.5	-3.2	-58.2	47.7	2.0	-2.2	4.2	-7.8	-26.1	7.1	-5.5	9.2		
δ_8	-1.1	3.0	25.2	6.8	-3.7	-4.2	-13.8	27.2	72.9	12.5	8.5	-8.7	-11.1	24.8	9.9	17.2	-34.5	3.3	-2.0	7.2	3.8	10.3	-12.1	4.4	7.7	0.2		
δ_9	22.9	24.9	9.6	35.1	5.5	-7.7	14.7	3.3	-4.9	27.5	21.8	-0.8	5.1	3.8	-8.5	-65.6	-23.1	-18.2	1.0	-25.1	-2.0	-4.6	-4.0	1.3	1.2	0.0		
δ_{10}	-45.6	-44.5	36.1	-10.8	-5.8	-14.4	-20.2	10.0	-16.1	-11.4	-6.7	14.4	-2.4	14.2	-1.8	-38.8	-4.8	-13.0	-4.4	6.3	3.9	12.2	-9.1	5.1	-3.7	29.7		
δ_{11}	-15.0	-12.7	-1.5	-22.9	-5.5	18.8	5.7	-26.6	33.1	7.4	-10.9	-35.9	-3.1	-2.4	-16.0	-32.6	17.0	-1.0	14.4	-0.9	-3.0	-2.6	16.1	-51.4	22.6	-12.0		
δ_{12}	-12.5	-25.6	3.8	5.1	0.2	4.3	11.3	43.0	-23.5	5.9	8.2	11.7	-8.1	6.6	14.3	1.6	-25.5	18.9	13.6	4.7	-15.5	-37.2	24.6	-21.2	9.9	-45.3		
δ_{13}	0.0	-25.9	-29.4	13.0	-12.3	23.3	4.1	42.7	-7.1	-8.2	17.5	-61.3	1.0	0.3	-1.1	-7.4	13.8	12.5	-12.8	-13.5	9.8	8.5	-11.1	17.5	-9.0	12.2		
δ_{14}	11.8	22.2	4.3	-1.7	-2.0	-9.5	-10.3	33.6	-27.6	8.1	3.8	2.2	6.2	0.4	-4.4	14.1	-2.1	12.5	25.3	-0.5	8.6	46.0	-0.9	-52.3	19.0	28.8		
δ_{15}	-4.7	-51.0	-25.6	49.9	7.0	-17.9	7.0	-37.7	9.3	3.3	18.7	11.7	6.2	-10.8	2.1	14.4	-18.4	16.1	9.1	-8.5	4.3	19.8	-1.4	-14.6	5.2	6.7		
δ_{16}	-21.6	-7.1	-31.2	-29.5	15.8	12.2	13.0	16.2	11.5	64.6	-5.7	32.4	-1.8	-13.8	7.7	-8.1	11.5	10.9	-6.9	-12.3	1.1	19.7	-9.9	11.9	-5.6	0.2		
δ_{17}	-42.7	26.2	-7.8	14.5	9.2	-29.3	-16.2	-1.6	-1.8	18.8	19.5	-10.3	10.8	20.0	-50.2	9.1	15.6	30.1	-4.1	10.1	-4.1	-25.9	5.8	4.5	-1.2	6.5		
δ_{18}	43.2	-28.0	10.2	-27.1	-8.3	-68.0	6.8	8.2	6.9	12.4	-6.8	-12.4	19.6	-0.2	-0.6	-4.8	21.3	15.3	-4.1	-4.7	-5.2	-3.5	2.1	5.2	-2.0	-10.0		
δ_{19}	28.2	-13.7	44.6	10.9	-19.1	38.3	0.0	-7.1	1.8	8.9	18.4	25.5	-17.5	0.1	-20.1	-1.5	32.6	45.8	-4.4	-3.4	2.1	-2.2	-1.4	3.6	-2.2	5.8		
δ_{20}	-28.0	20.4	30.4	17.2	31.3	-8.7	17.2	-4.5	0.4	-14.8	-3.8	-17.4	7.3	-8.0	39.4	-8.6	24.0	30.5	-1.4	-7.6	-23.6	32.9	-6.4	5.8	-3.0	-25.5		
δ_{21}	-4.1	5.8	-6.0	-40.2	-3.3	-3.4	-4.3	-18.8	-3.0	-8.1	81.0	1.7	-0.8	12.4	32.2	-2.2	1.6	-1.3	3.4	-2.9	1.2	-2.8	0.8	-3.1	1.3	4.6		
δ_{22}	6.1	-9.3	-1.9	-14.5	-4.7	7.9	2.4	-2.4	-8.7	-4.6	15.6	-1.6	-2.2	6.3	-46.5	5.7	-17.8	-15.2	-5.2	10.3	-56.2	44.2	-9.9	10.4	-4.0	-31.1		
δ_{23}	-4.0	13.9	-26.0	18.5	-66.4	-6.0	-19.3	-7.5	0.1	11.0	-13.2	6.9	-2.9	13.7	33.0	-16.4	10.0	11.6	0.3	19.9	-36.7	3.1	-2.1	0.0	1.3	3.9		
δ_{24}	-13.7	10.0	-0.1	1.6	-35.7	-9.8	9.1	-3.2	-4.9	-3.2	5.1	5.4	0.7	-1.8	-10.9	-8.0	-1.7	1.1	-3.8	16.0	64.7	28.9	0.5	5.9	-6.3	-51.0		
δ_{25}	-28.4	7.5	18.0	-3.2	-45.0	-9.8	39.7	3.5	4.8	-3.4	1.5	2.7	1.8	-14.6	-8.8	27.6	-1.4	-15.2	2.1	-59.0	-10.5	-7.2	0.5	-1.9	1.6	10.7		
δ_{26}	5.8	-7.2	-1.2	-0.3	7.5	8.5	-2.0	-19.7	-20.0	16.0	-18.6	-7.1	-3.6	80.1	8.8	14.4	6.1	-5.0	1.5	-35.3	9.5	8.4	0.3	0.2	-0.9	-12.3		

Table 21: Orthogonal transition matrix U_{jk} from the original ($b_{E'_e}$, etc) to the diagonalised (b_1^{ave} , b_{26}^{ave}) systematic sources for the averaged H1 data. The matrix elements are given in %.

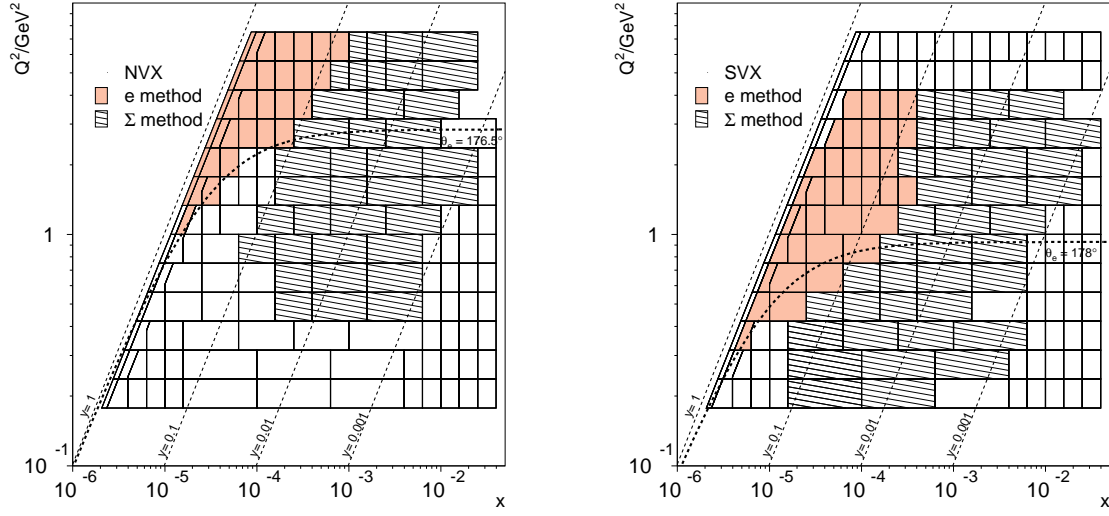


Figure 1: Illustration of the bins used for the cross section measurement in the NVX (left) and SVX (right) analyses. Dashed lines of constant θ_e indicate approximate angular acceptance for both measurements. The dark (light) shaded area corresponds to the bins where the electron (Σ) method is used for the measurement of the cross section. The measurement in the bins outside the angular acceptance range employ the Σ method for ISR events.

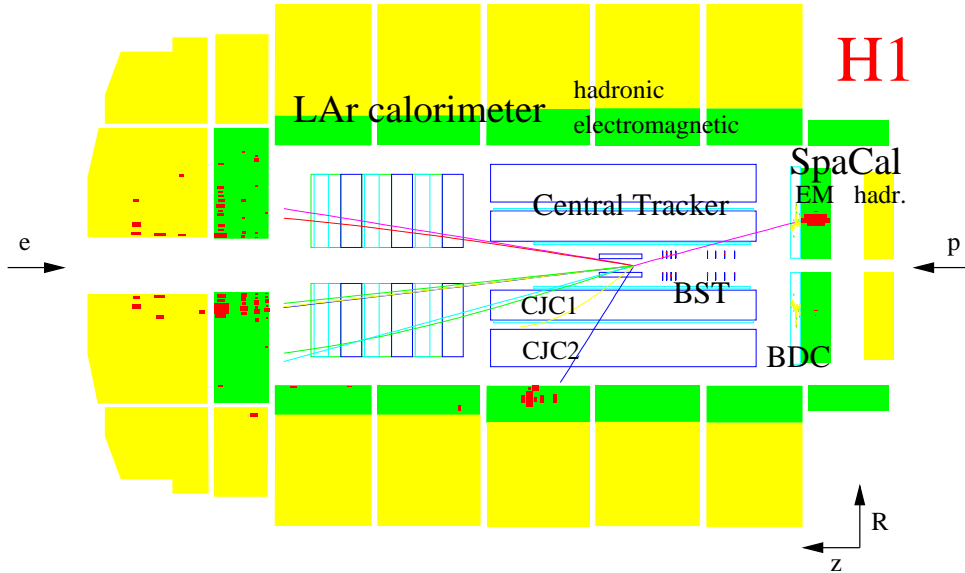


Figure 2: A low Q^2 event as reconstructed in the H1 detector. The electron is scattered into the backward region. The electron trajectory is reconstructed in the Backward Silicon Tracker (BST) and in the Backward Drift Chamber (BDC). The electron energy is determined using the SpaCal calorimeter. The hadronic final state is detected in the central and forward tracking detectors, and in the LAr calorimeter.

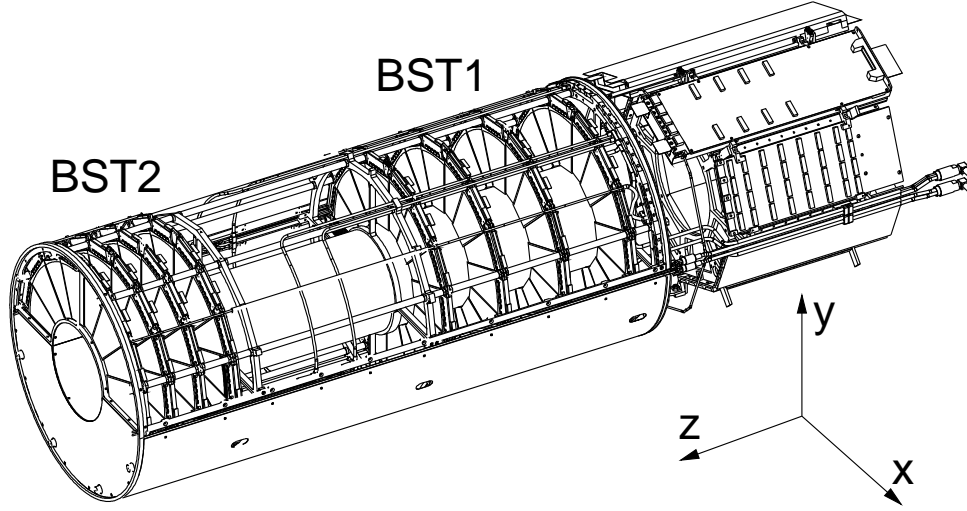


Figure 3: Schematic layout of the H1 Backward Silicon Tracker (BST). The active area is composed of eight wheels subdivided into two modules, BST1 and BST2, of four wheels each. One wheel is made of 16 r sensors and one u sensor (mounted on the back side, not shown here). Eight consecutive sensors in $1/16$ of azimuth build a BST sector. In z the module BST1 extends from -73.2 to -95.7 cm, BST2 from -35.9 to -46.9 cm. Readout boards are placed in the rear section. Also indicated are the electric shielding and the water cooling pipes.

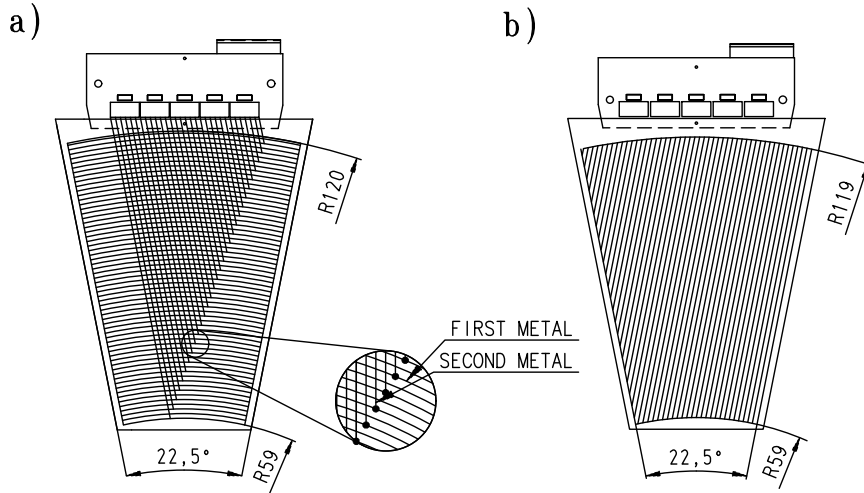


Figure 4: The two types of silicon sensors used in the BST: a) r sensor, b) u sensor, each with 640 readout strips. The r sensor has a double metal structure for the readout lines to reach the top (outer radius) part where the five amplifiers are mounted on the hybrid, as sketched.

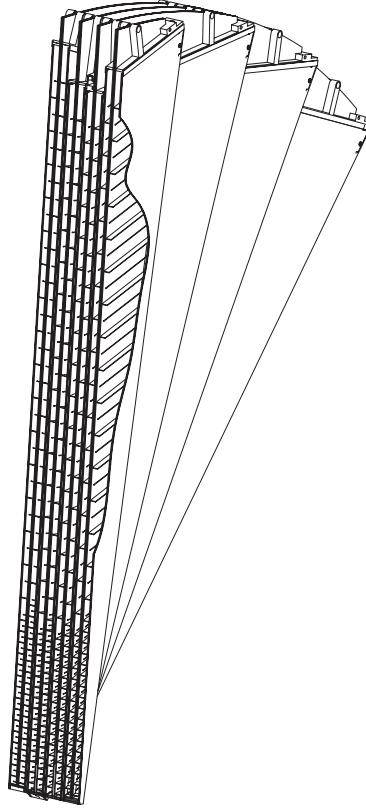


Figure 5: Three-dimensional view of a section of the BDC illustrating the layer structure and the drift cell geometry. The chamber has a radial coverage from 6 cm to 71 cm. At a radius of about 22 cm the segmentation is changed and a transition drift cell is introduced.

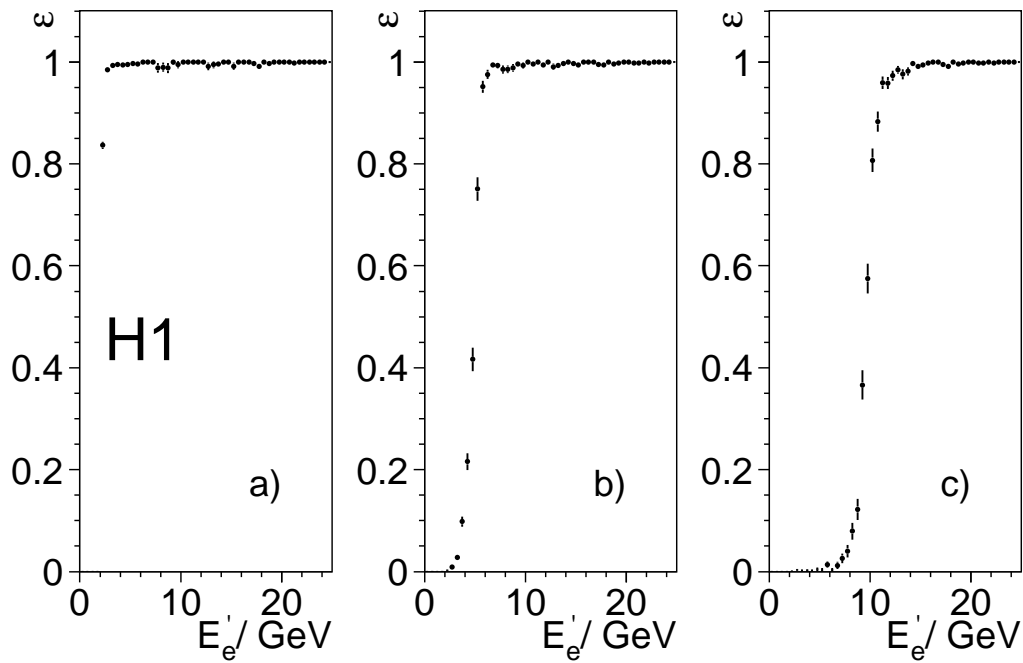


Figure 6: Efficiency of the SpaCal electron triggers, S9 a), S0 b), and S3 c), used in this analysis, as a function of E'_e .

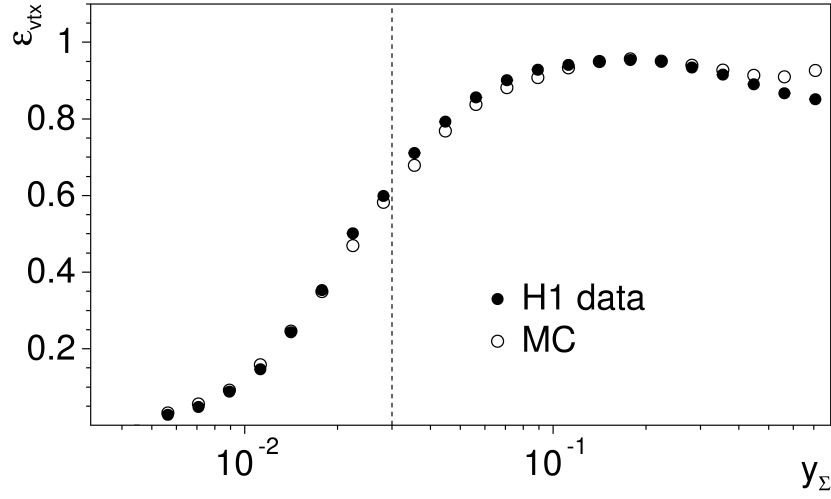


Figure 7: Central Tracker vertex reconstruction efficiency as a function of y_Σ . The dashed line corresponds to the applied selection criterion, $y_\Sigma > 0.03$. In the analysis the cross section at high y is measured with y_e instead of y_Σ .

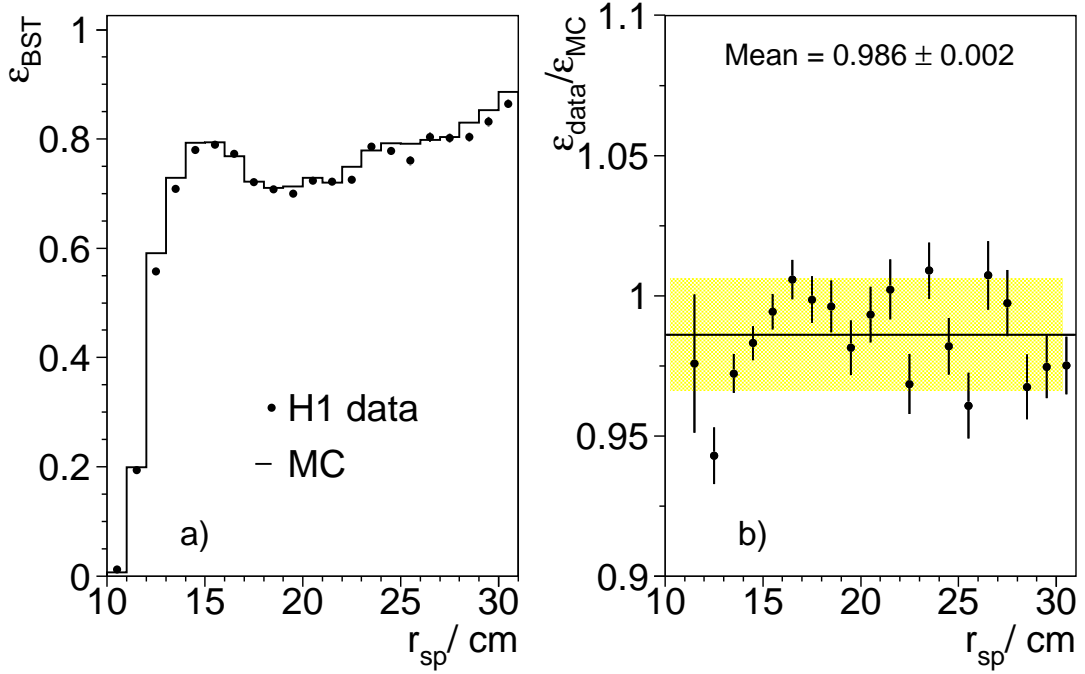


Figure 8: a) BST track segment finding efficiency as a function of the radial position of the electron candidate in the SpaCal, for the NVX data sample, b) ratio of data to MC efficiencies.

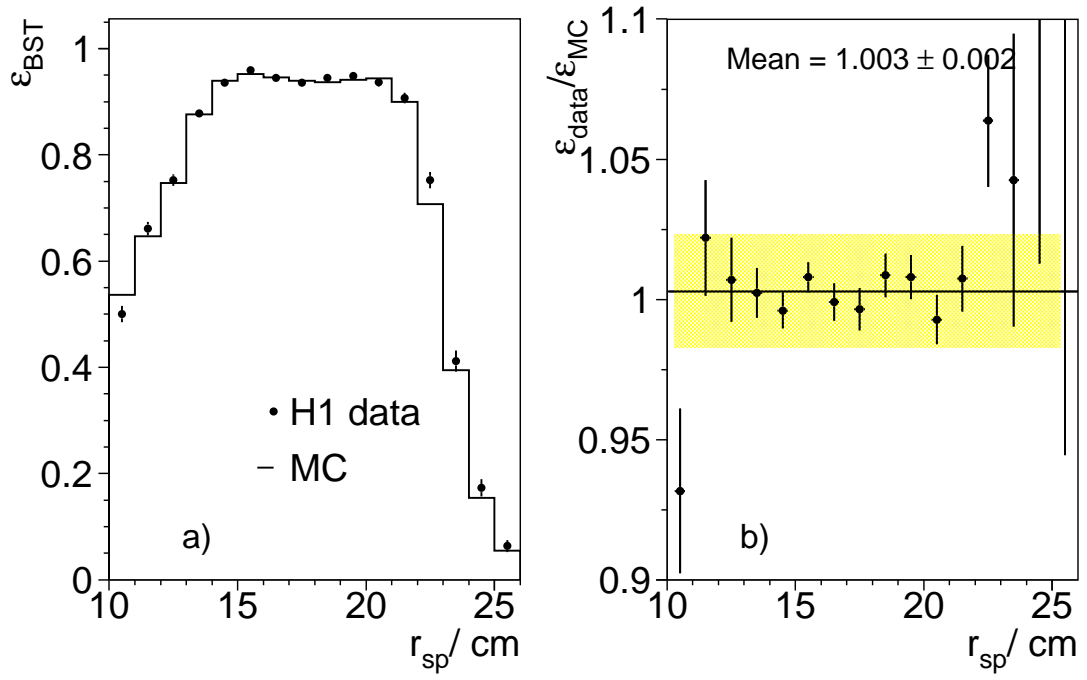


Figure 9: a) BST track segment finding efficiency as a function of the radial position of the electron candidate in the SpaCal, for the SVX sample, b) ratio of data to MC efficiencies.

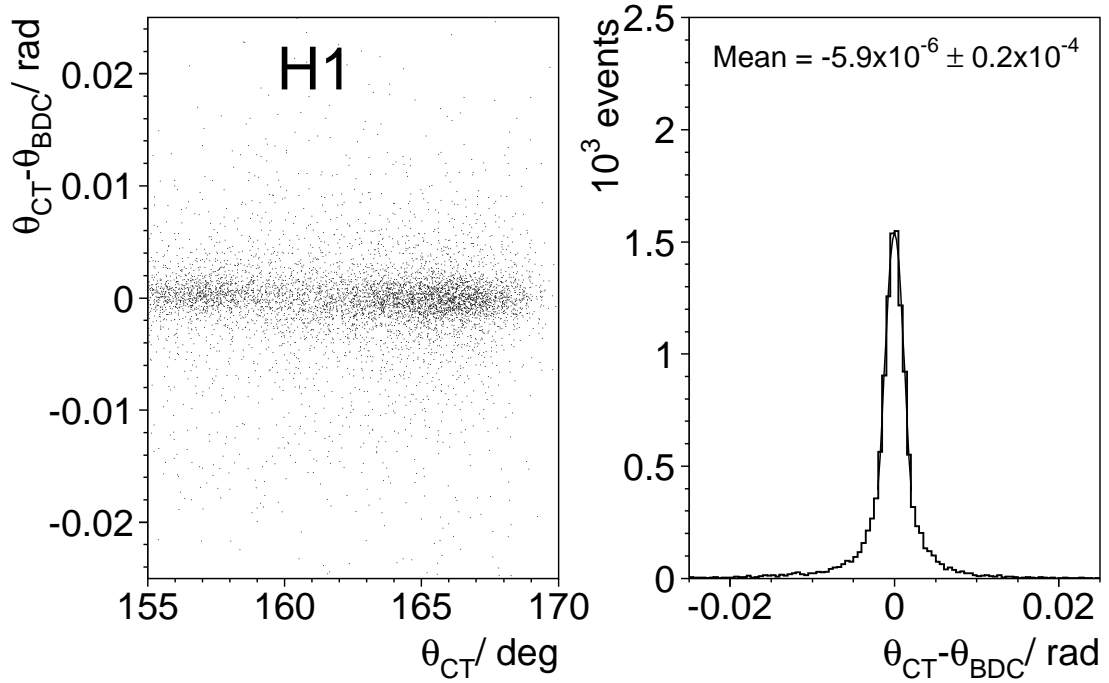


Figure 10: Relative alignment of the Central Tracker (CT) and BDC. Left: $\theta_{\text{CT}} - \theta_{\text{BDC}}$ versus θ_{CT} after alignment. Right: $\theta_{\text{CT}} - \theta_{\text{BDC}}$ after alignment.

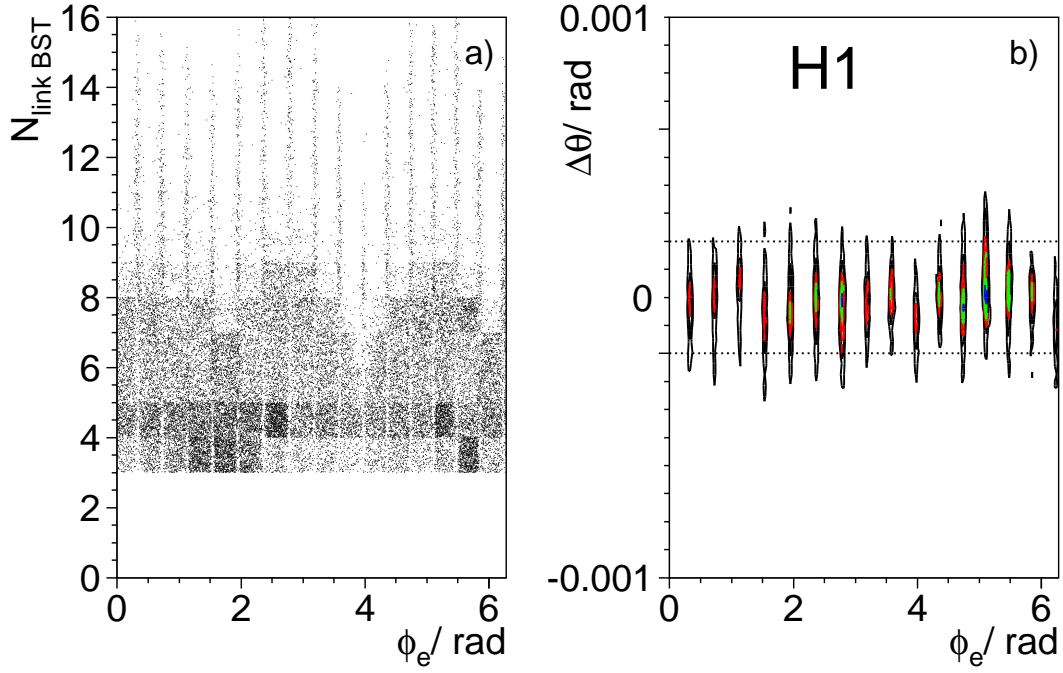


Figure 11: a) Scatter plot of the number of BST hits linked to the electron candidate BST track as a function of the azimuthal angle ϕ_e determined by the associated SpaCal cluster. At least three linked hits are required to define a track. A number of linked hits exceeding eight corresponds to a track passing the azimuthal BST wafer overlap region; b) Contours of equal density for the distribution of $\Delta\theta = \theta_1 - \theta_2$, where $\theta_{1,2}$ are the polar angles measured in the two overlapping BST sectors, as a function of ϕ_e . The horizontal dotted lines indicate ± 0.2 mrad as is used for the systematic uncertainty of the alignment.

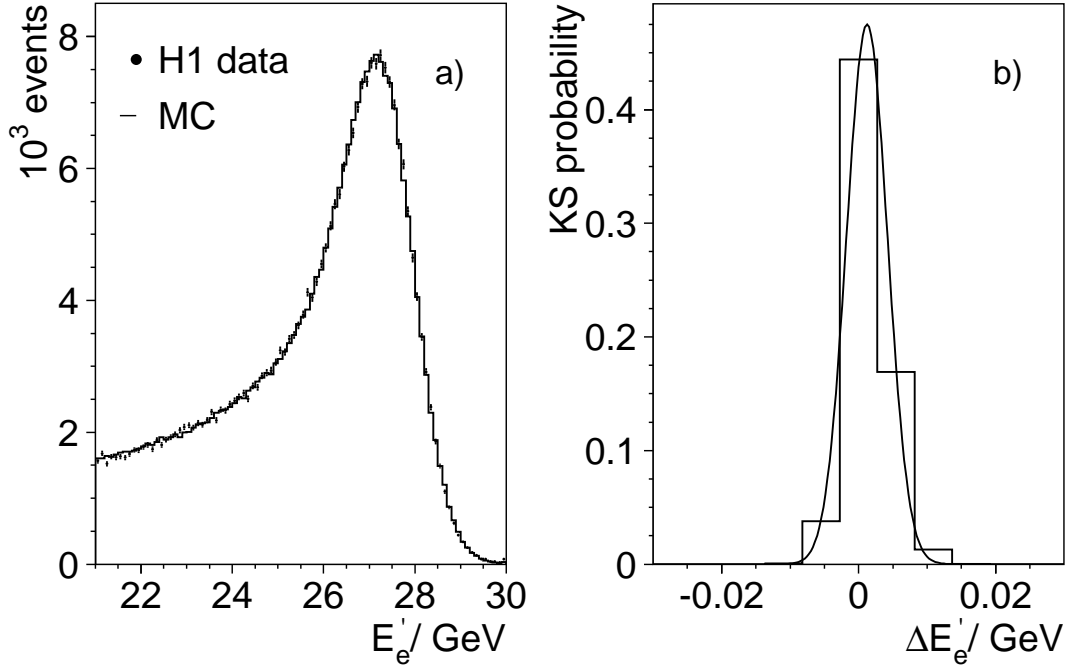


Figure 12: a) Distribution of the scattered electron energy E'_e for the NVX data sample; b) Kolmogorov-Smirnov test probability distribution as a function of the relative shift in the measured and simulated energy distributions.

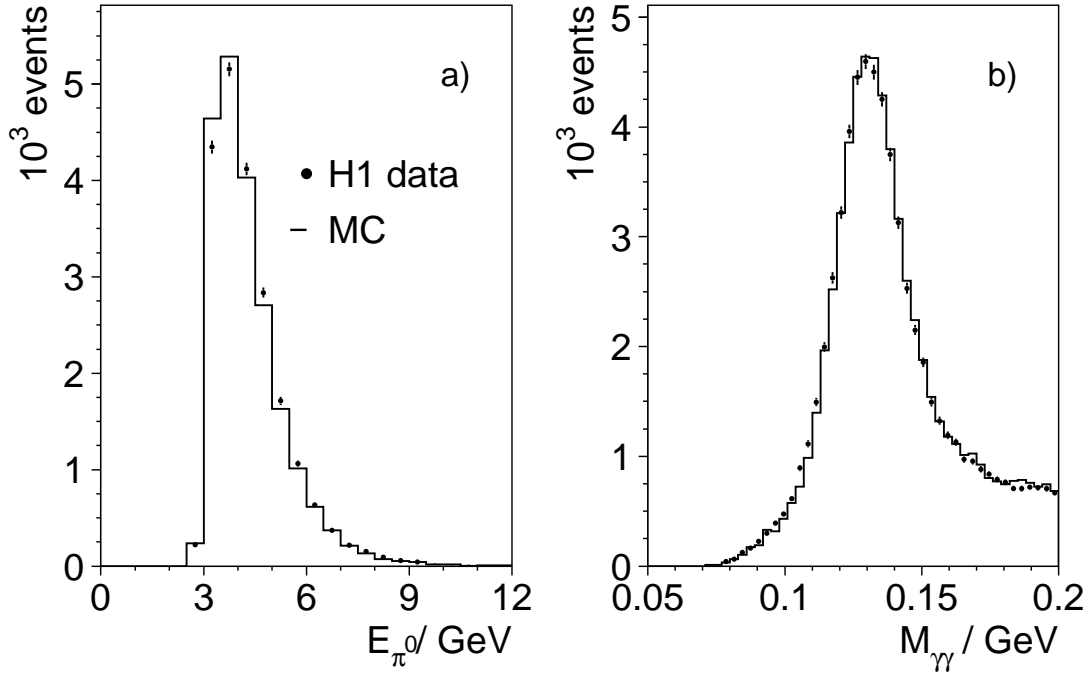


Figure 13: a) Energy distribution for π^0 candidates based on the NVX sample as triggered by the low energy trigger, S9; b) di-photon invariant mass distribution for π^0 candidates. The double angle calibration constants are applied to the data and MC simulation.

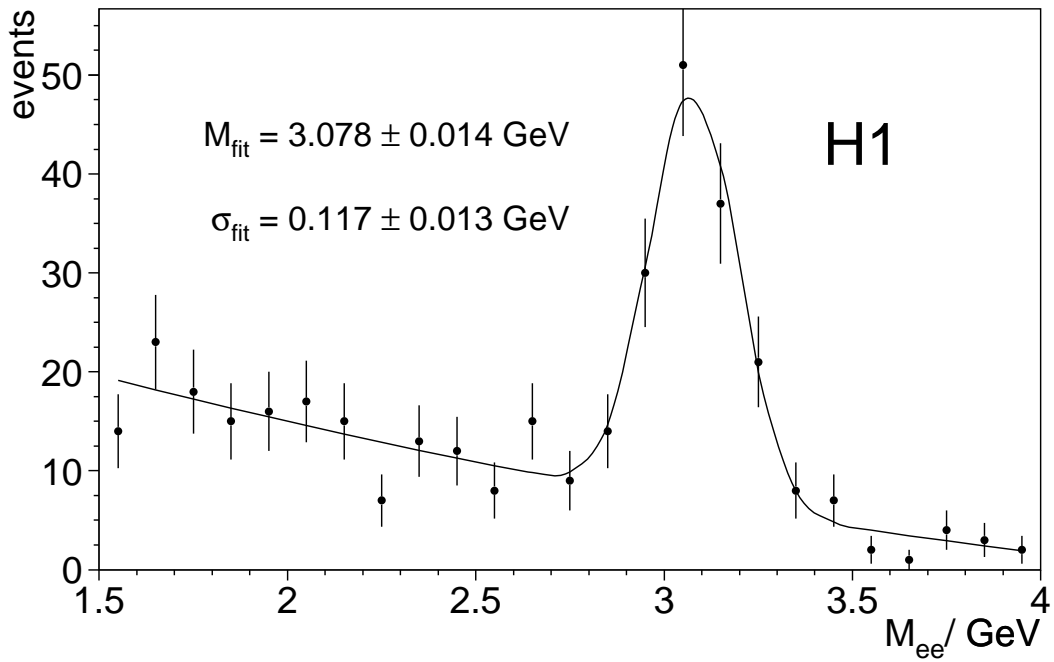


Figure 14: Invariant mass distribution of the two electron candidate tracks for a special J/ψ event selection. The line indicates a fit to the data. M_{fit} and σ_{fit} correspond to the Gaussian mean and width of the peak.

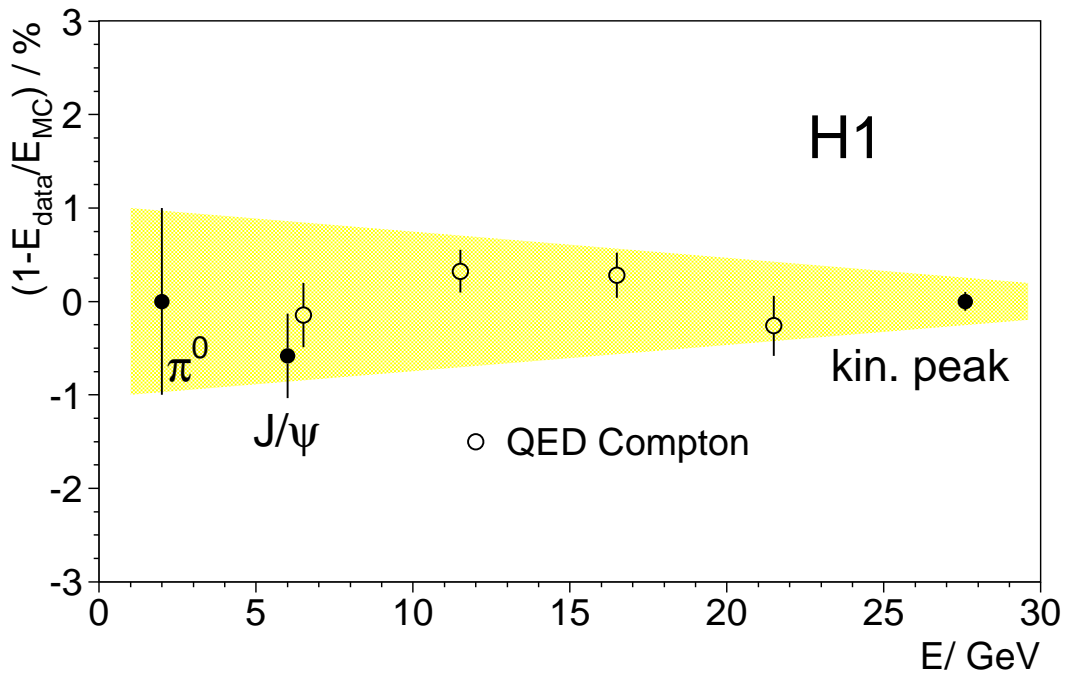


Figure 15: Summary of SpaCal energy scale determination. The band indicates the uncertainty due to the scale difference between the data and the simulation.

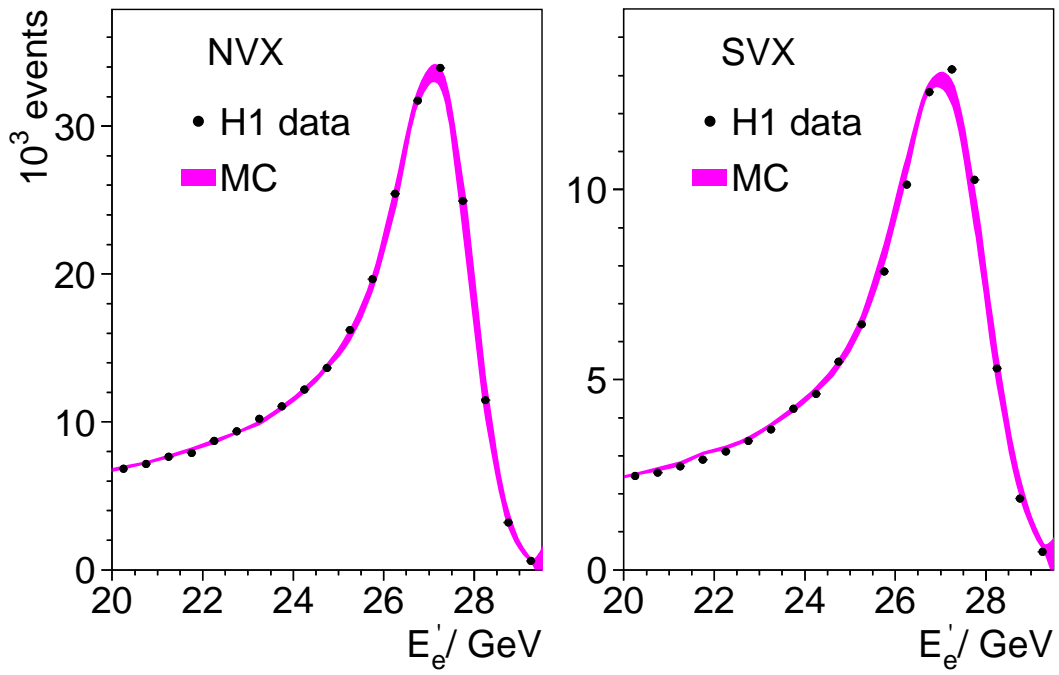


Figure 16: Distributions of the scattered electron energy E'_e for the data and the MC simulation in the NVX (left) and the SVX (right) analyses. The MC bands include the statistical uncertainty and the effect of a $\pm 0.2\%$ electromagnetic energy scale variation.

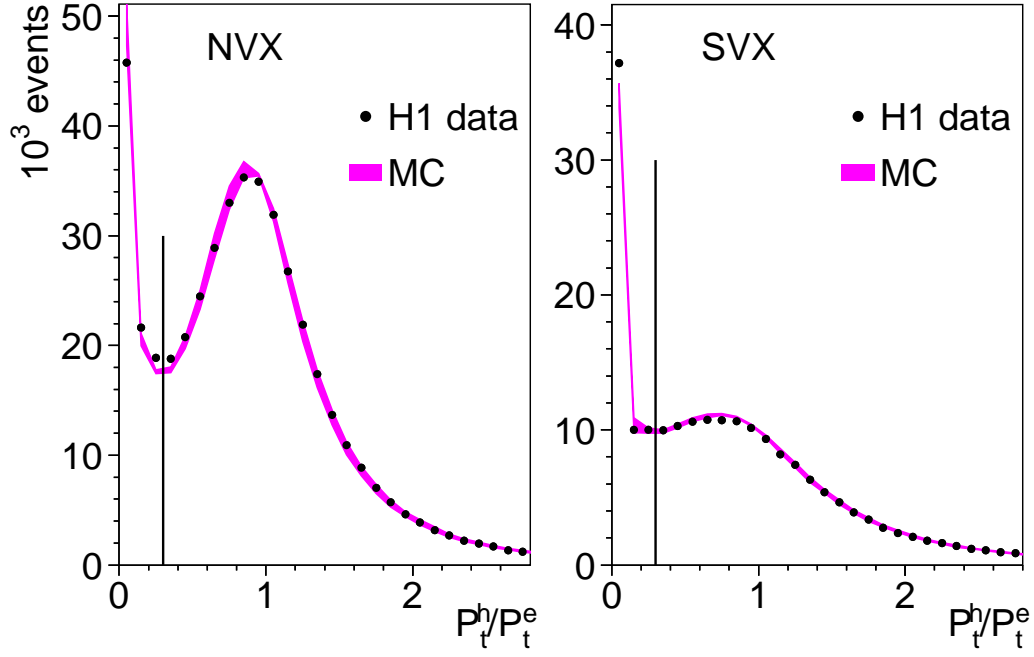


Figure 17: Transverse momentum balance P_T^h/P_T^e distribution for the data and the MC simulation in the NVX and the SVX analyses. The bands include the statistical uncertainty of the simulation and the effect of the LAr hadronic scale uncertainty, see description in the text. The vertical line indicates the analysis requirement $P_T^h/P_T^e > 0.3$.

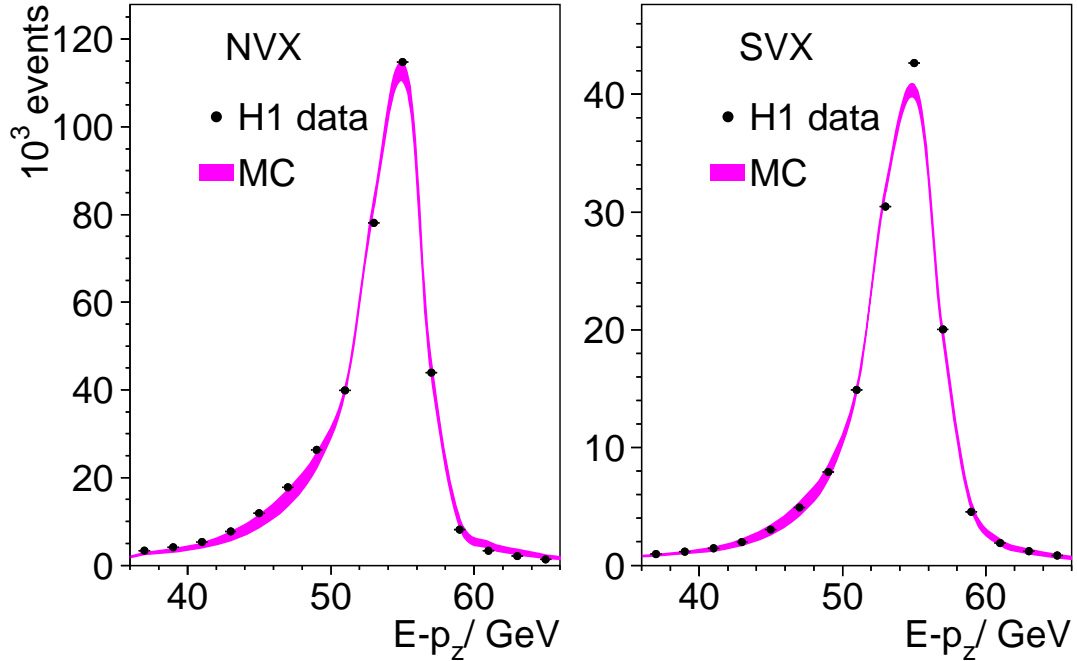


Figure 18: $E - P_z$ distribution for the data and the MC simulation in the NVX and the SVX analyses. The bands include the statistical uncertainty of the simulation and the effect of a ± 0.5 GeV variation of the SpaCal hadronic final state contribution.

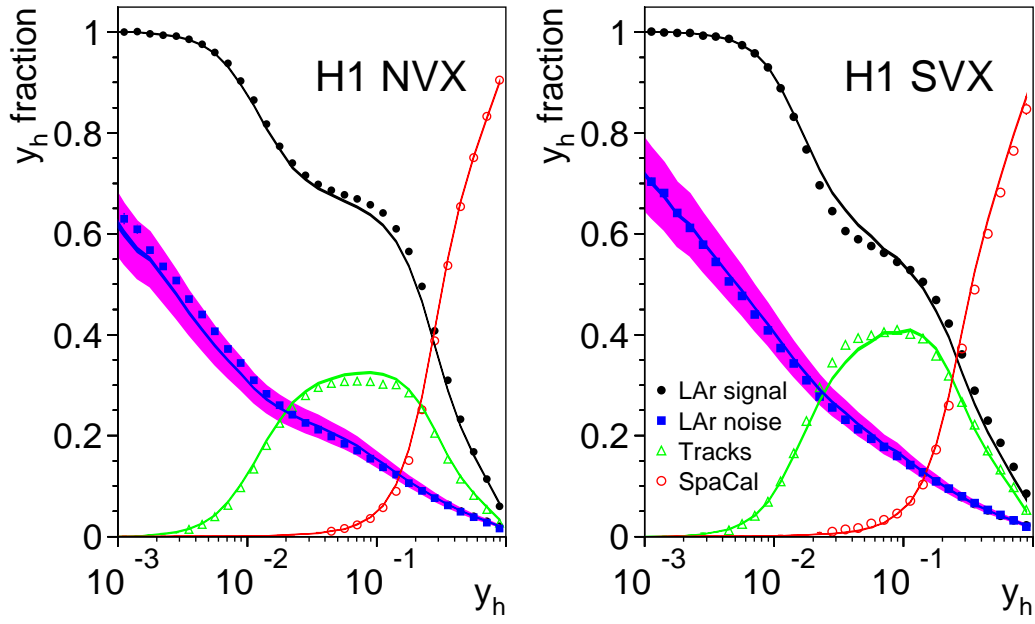


Figure 19: Relative contributions to the measured y_h from the LAr (closed circles), tracks (triangles) and SpaCal (open circles) together with the subtracted LAr noise fractions (squares) in the NVX (left) and SVX (right) analyses. The distributions of simulated events are shown as curves. The shaded areas correspond to a 10% systematic uncertainty on the LAr noise description.

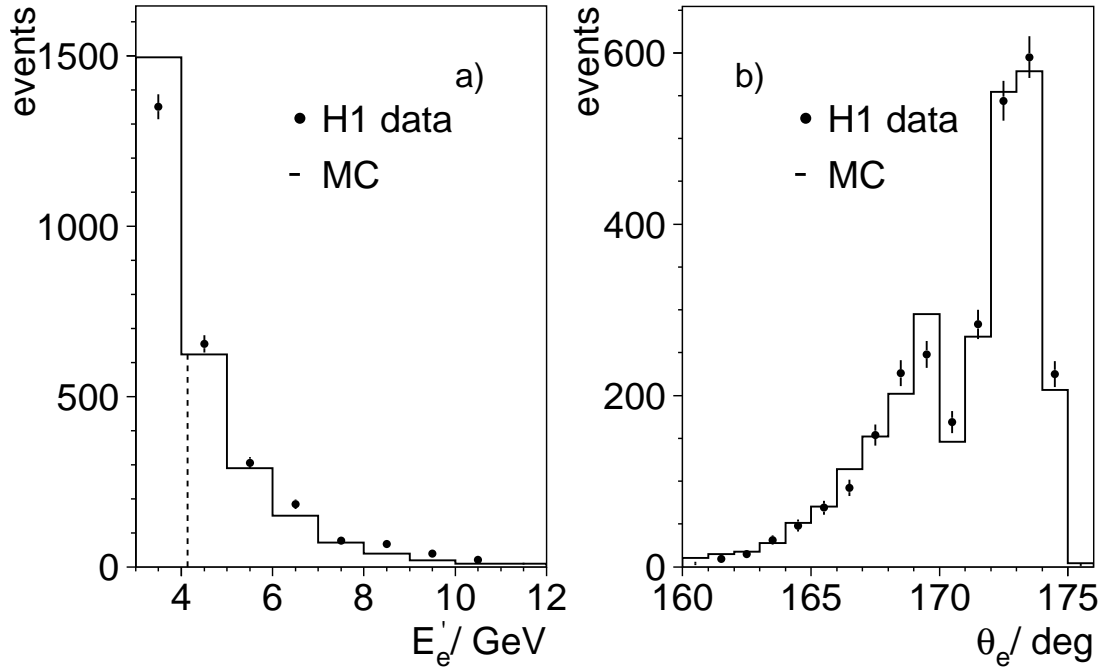


Figure 20: Distribution of E'_e a) and θ_e b) for photoproduction events detected in the electron tagger. The plots are based on the NVX-S9 analysis. The dashed line in a) corresponds to the minimum E'_e permitted by the analysis cut $y_e < 0.85$.

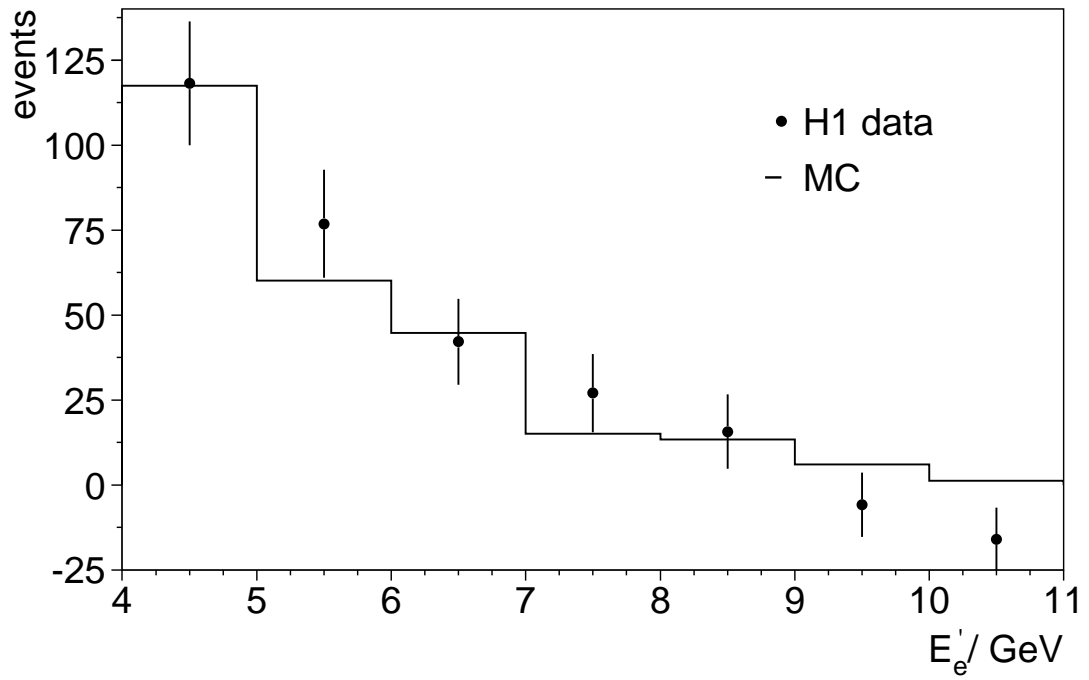


Figure 21: Distribution of E'_e for background events, estimated using wrong charge BST tracks (equation 25) for data and the PHOJET simulation. The simulated sample is normalised using photoproduction events with the scattered electron detected in the electron tagger.

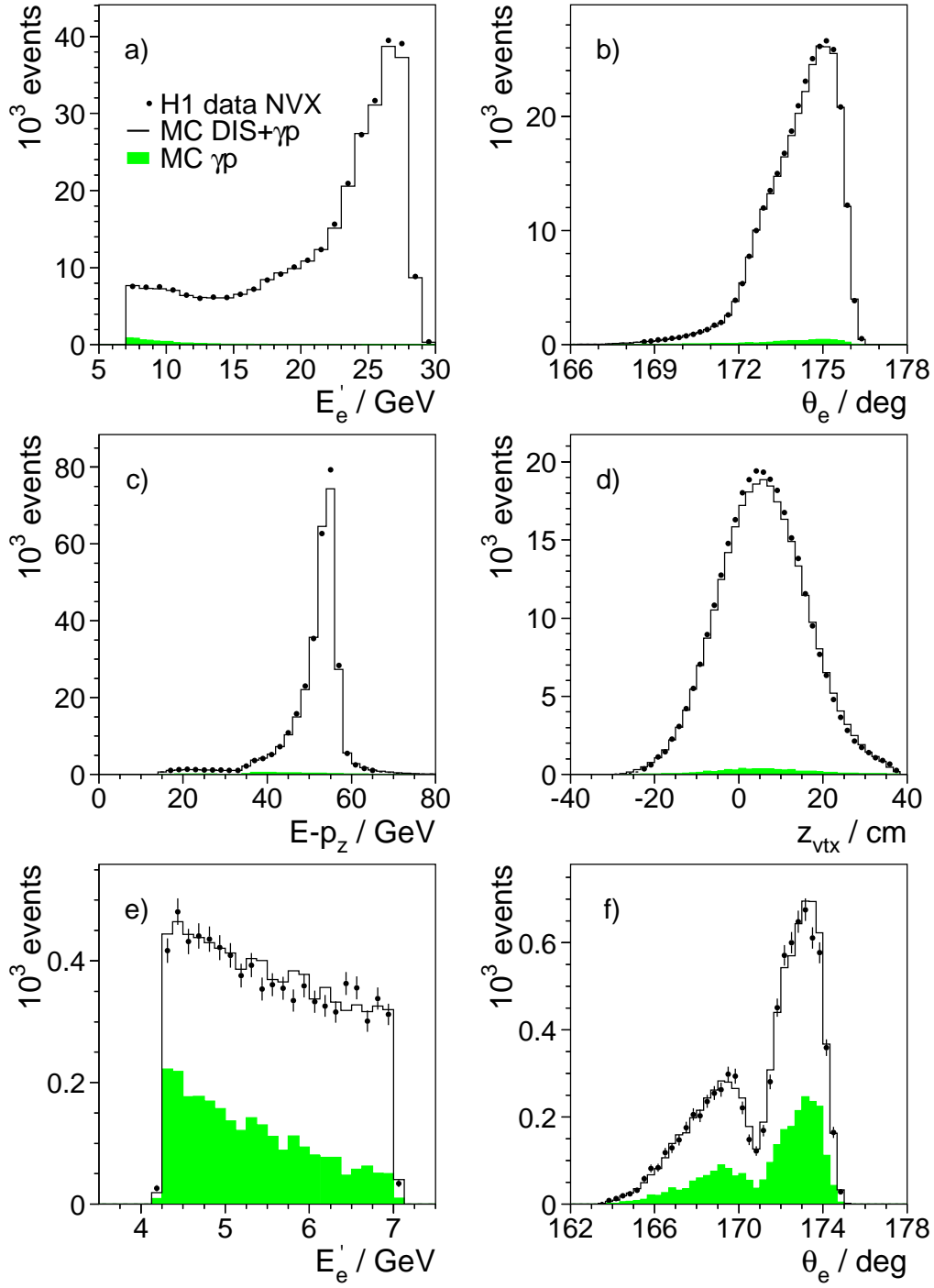


Figure 22: Distribution of events for the NVX-BST analysis: the energy a) and the polar angle b) of the scattered positron; $E-p_z$ c) and the z vertex position d). Control distributions for the NVX-S9 analysis: energy e) and polar angle f) of the scattered positron candidates. The histograms represent the simulation of DIS and the photoproduction background (shaded).

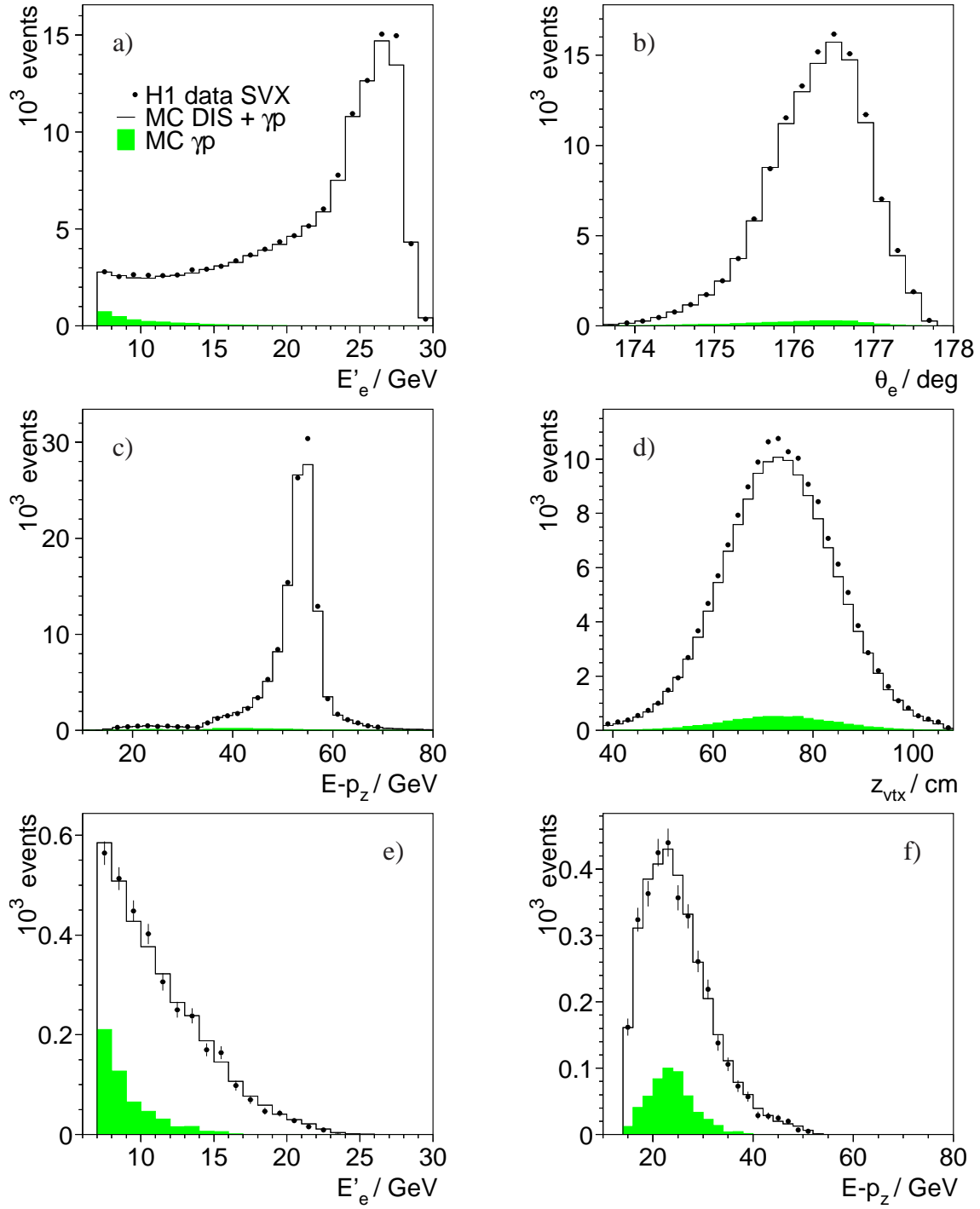


Figure 23: Distribution of events for the SVX-BST a-c,e,f) and SVX-BDC d) analyses: the energy a) and the polar angle b) of the scattered positron; $E-p_z$ c) and the z vertex position d); the energy e) and $E-p_z$ f) for the ISR bins. The histograms represent the simulation of DIS and the photoproduction background (shaded).

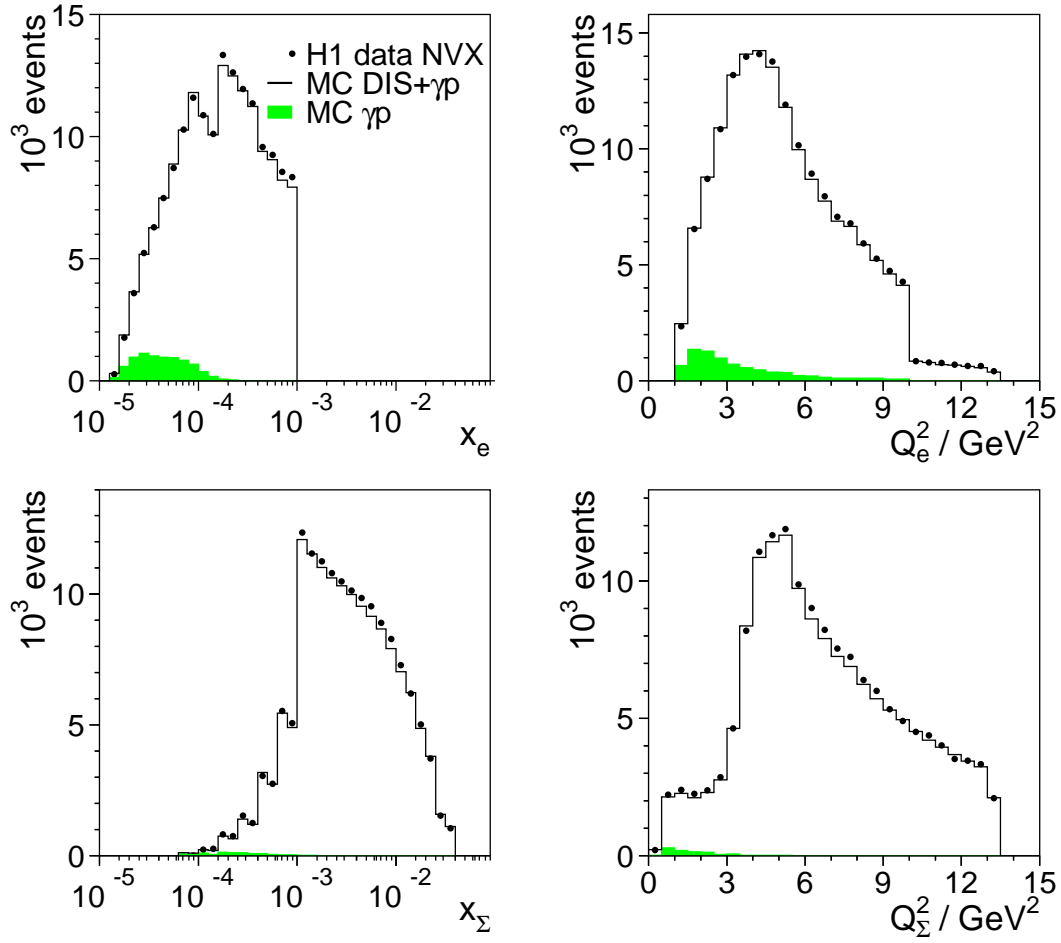


Figure 24: Distribution of Bjorken- x and Q^2 using the electron (top) and sigma (bottom) reconstruction methods for the NVX data. The histograms represent the simulation of DIS and the photoproduction background (shaded).

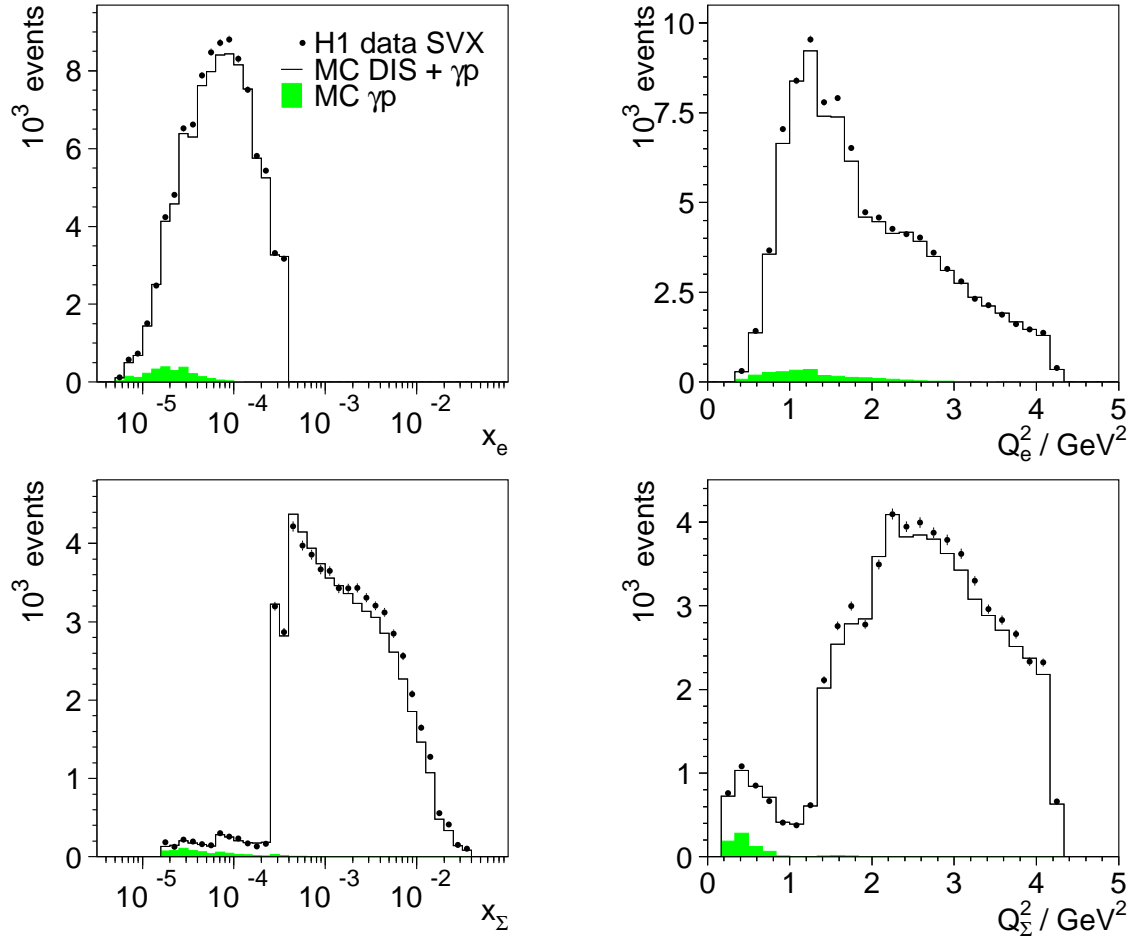


Figure 25: Distribution of Bjorken- x and Q^2 using the electron (top) and sigma (bottom) reconstruction methods for the SVX data. The histograms represent the simulation of DIS and the photoproduction background (shaded).

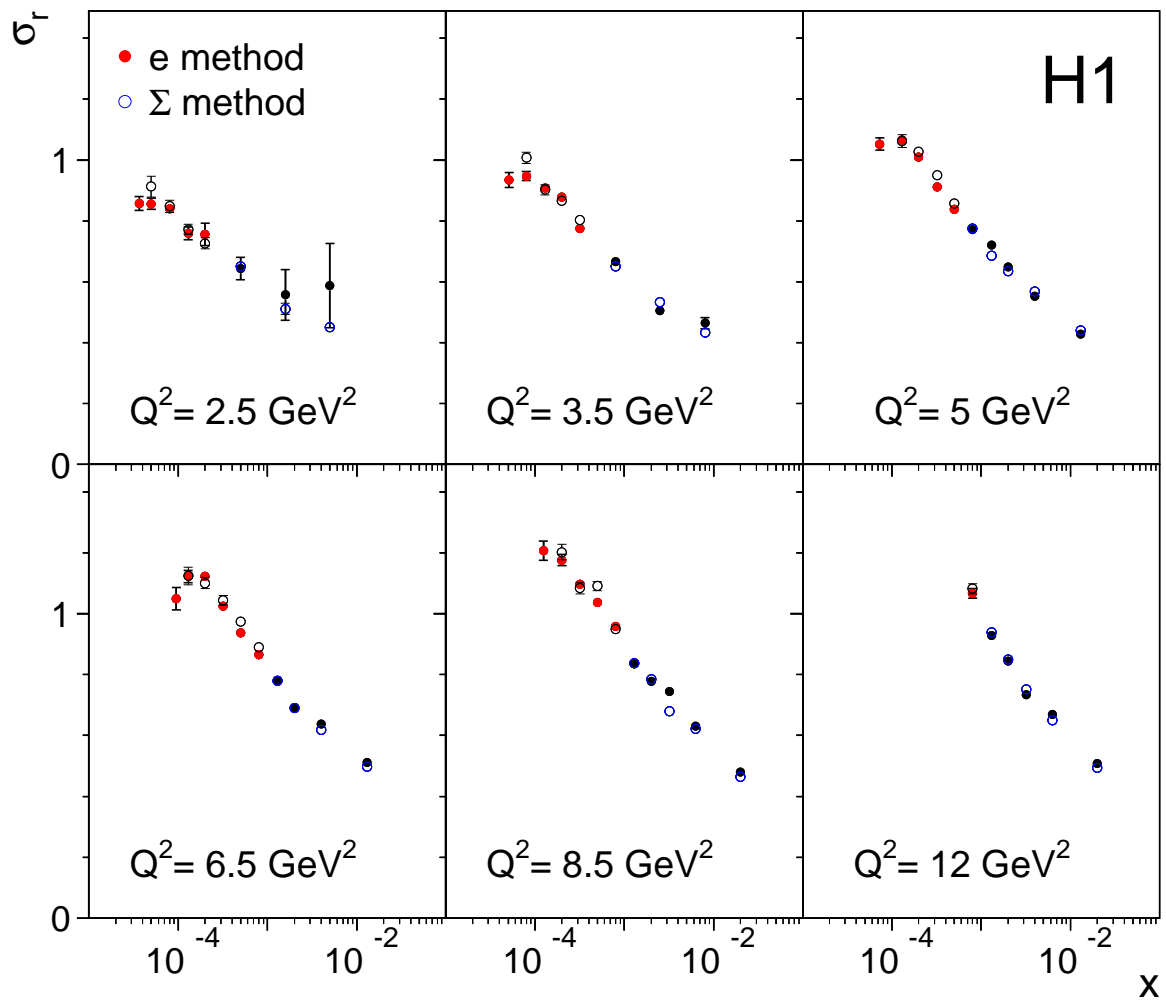


Figure 26: Comparison of reduced cross sections as obtained with the electron (closed circles) and Σ (open circles) reconstruction methods, for the NVX data sample. The errors represent statistical uncertainties only.

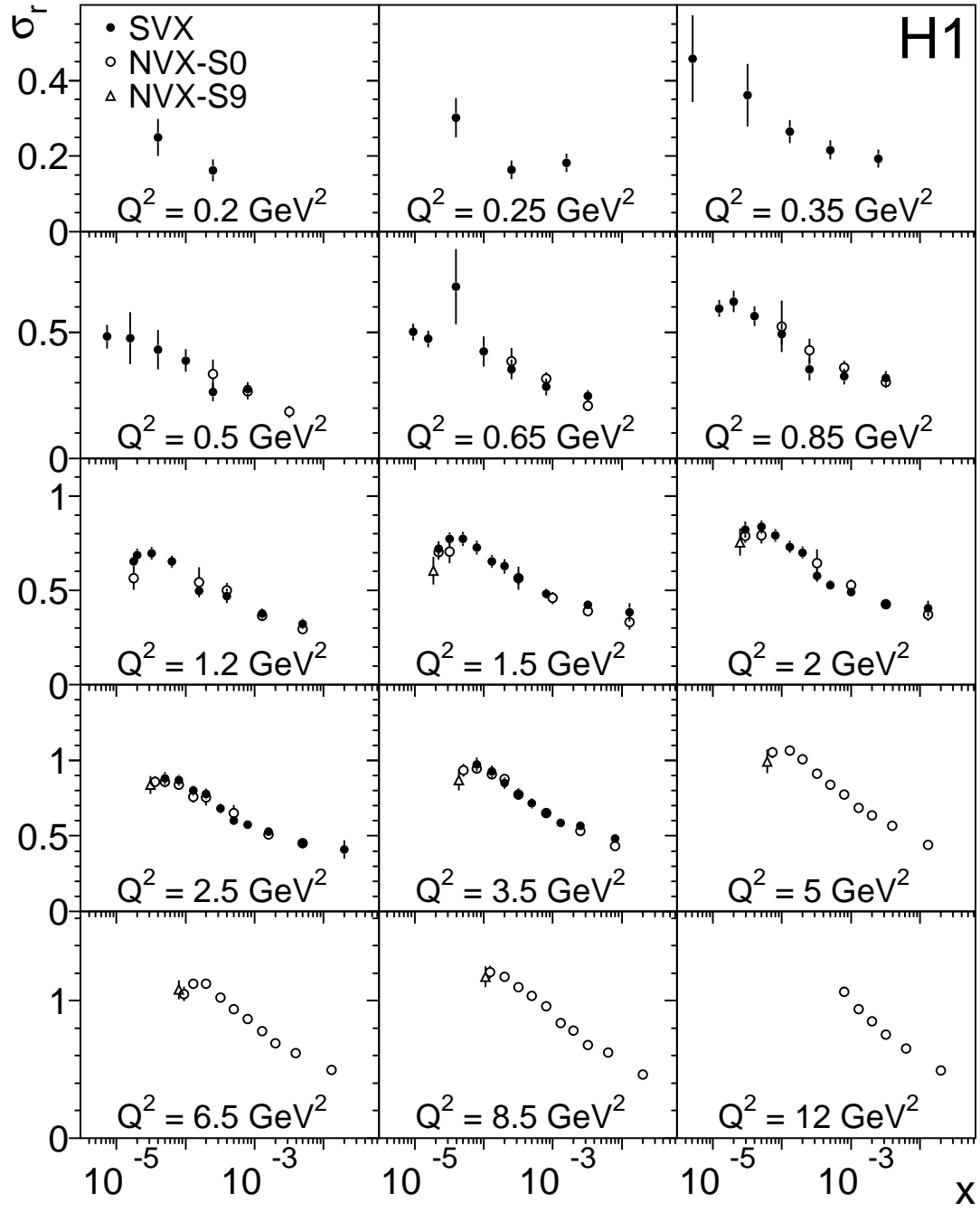


Figure 27: Reduced inclusive e^+p scattering cross section as measured in the NVX-BST (open circles), NVX-S9 (triangles) and SVX (closed circles) analyses of the 920 GeV data. The errors represent the statistical and systematic uncertainties added in quadrature.

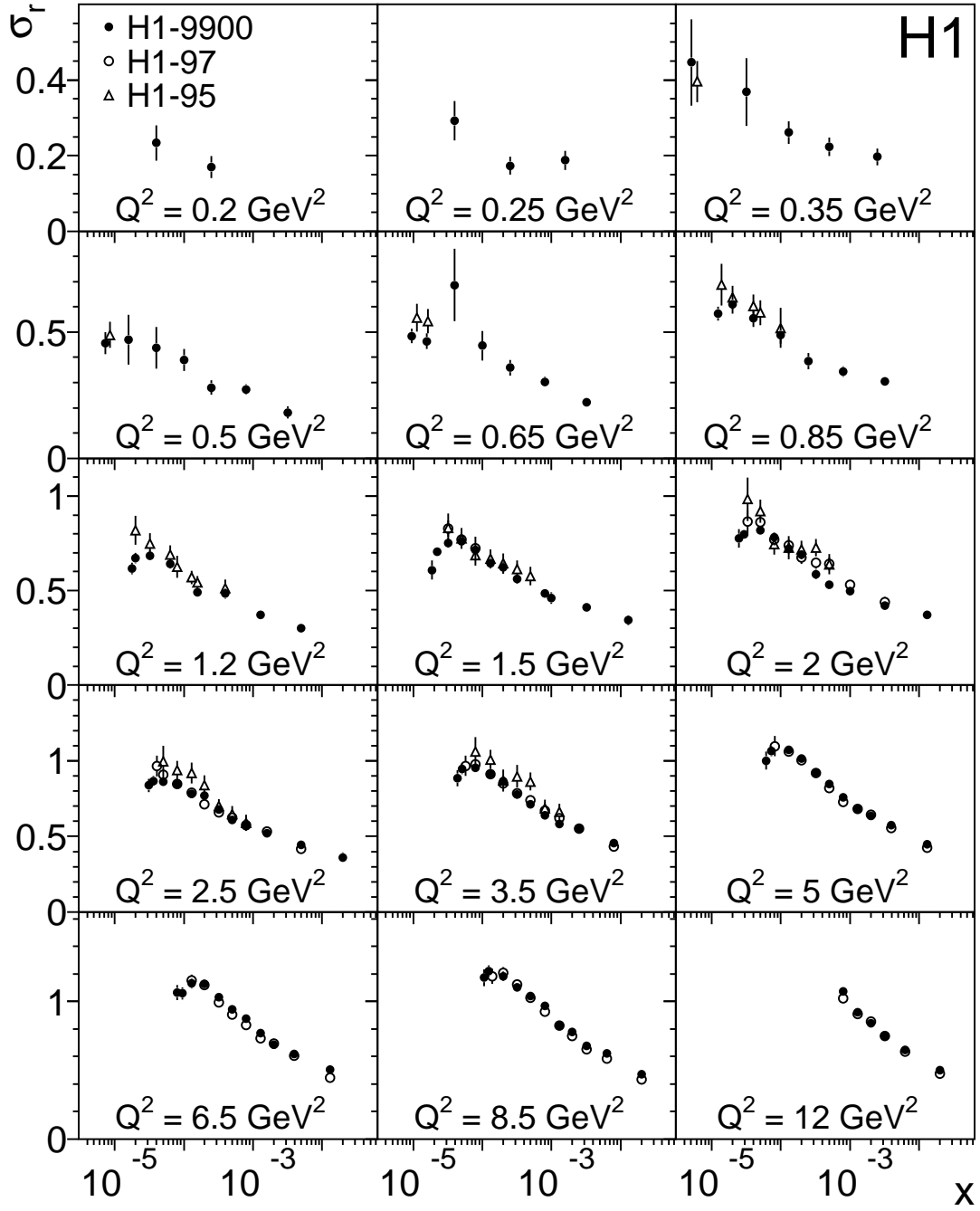


Figure 28: Reduced cross section σ_r . Closed circles: combined 1999-2000 data taken at $E_p = 920 \text{ GeV}$; Triangles: SVX data taken in 1995 [35]; Open circles: NVX data taken in 1997 [37]. The normalisation of the 1997 data has changed by +3.4%, see section 8.4. The 1995 and 1997 data were taken at $E_p = 820 \text{ GeV}$ but are corrected here for comparison to 920 GeV . The errors represent the statistical and systematic uncertainties added in quadrature.

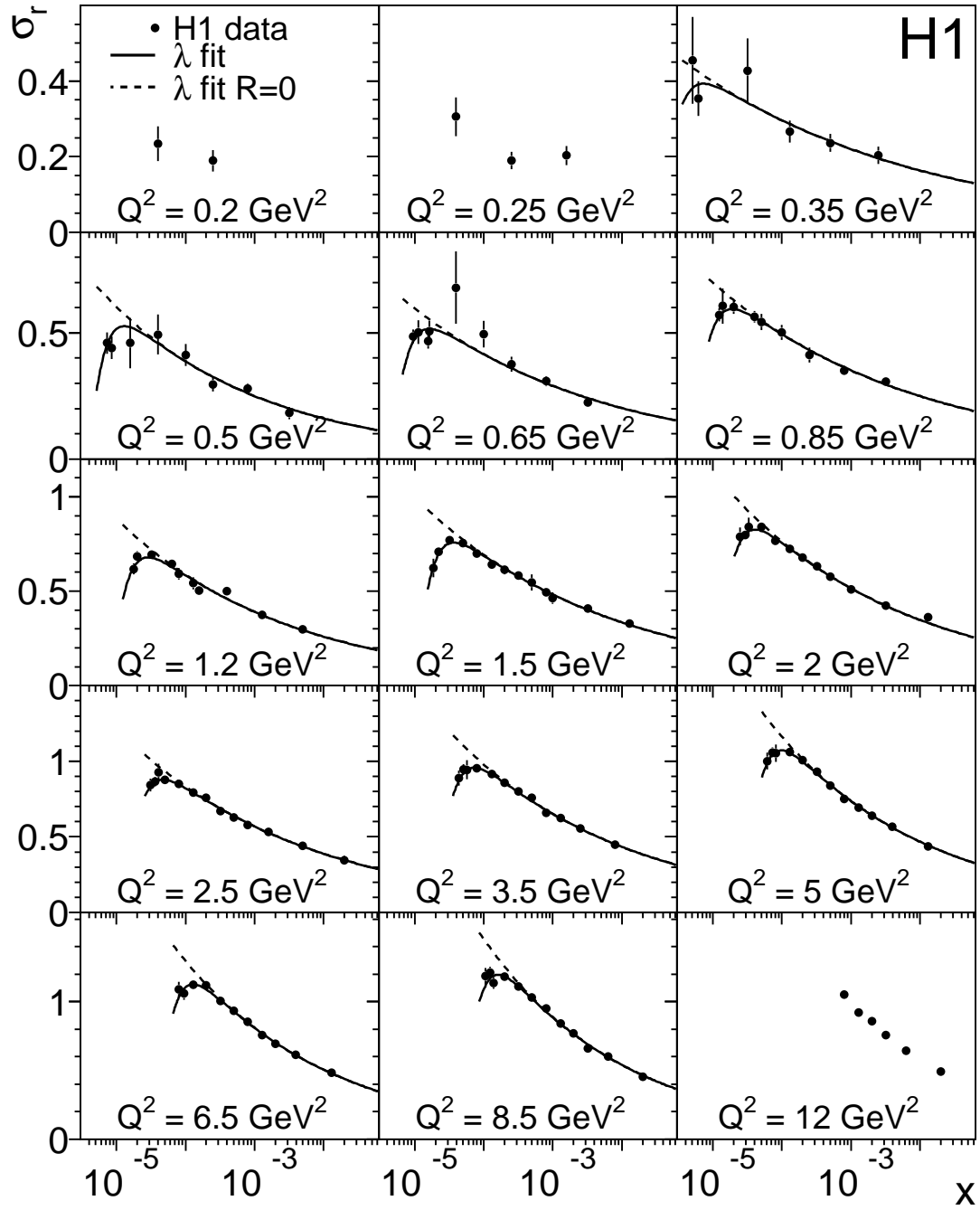


Figure 29: Reduced cross section σ_r , from the combined low Q^2 H1 data, as a function of x compared to the λ fit result (solid line) and to a λ parameterisation with the same values of $c(Q^2)$ and $\lambda(Q^2)$ but $R = 0$ (dashed line). The errors represent the statistical and systematic uncertainties added in quadrature.

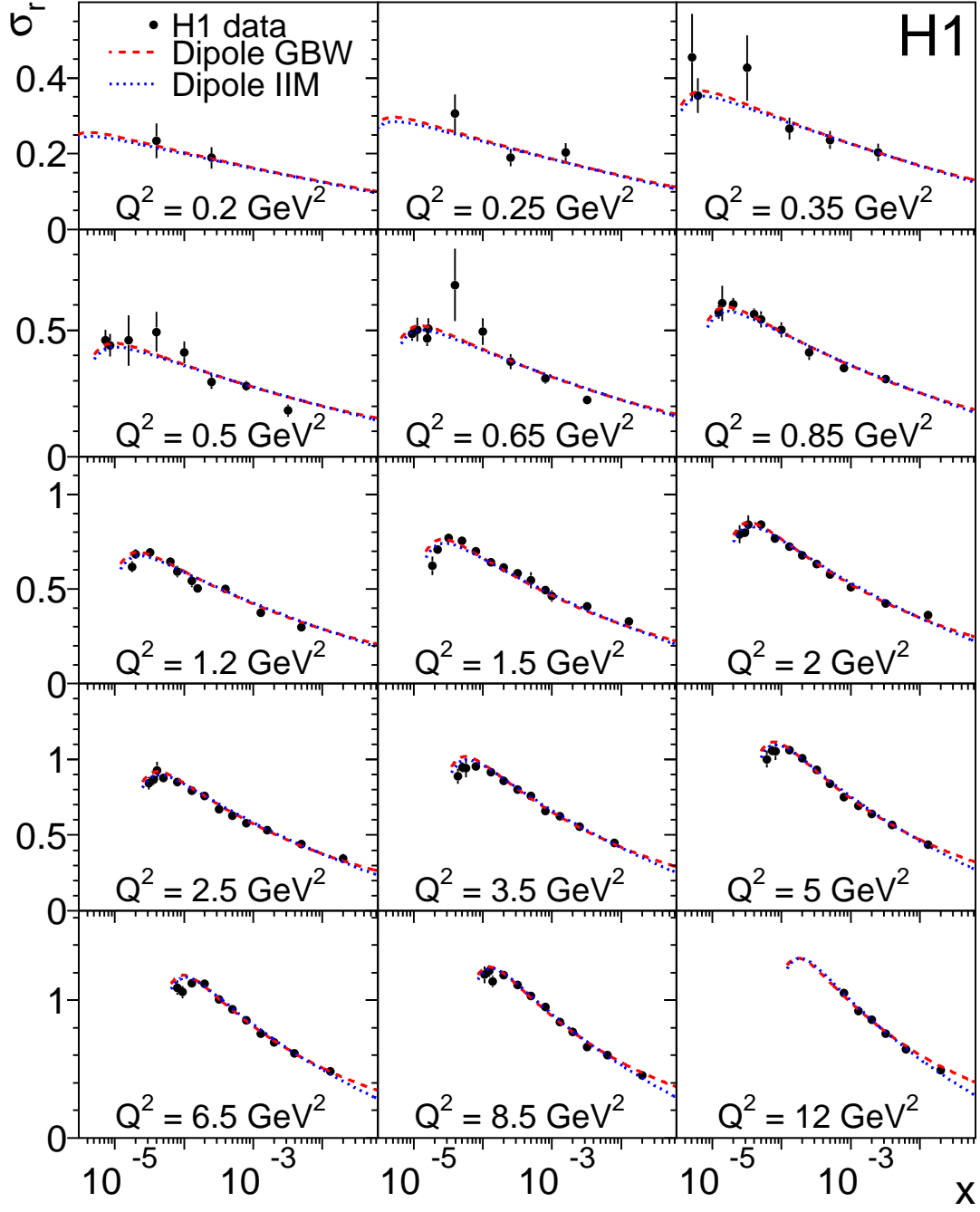


Figure 30: Reduced cross section σ_r , from the combined low Q^2 H1 data, as a function of x compared to the GBW and IIM models. The errors represent the statistical and systematic uncertainties added in quadrature.

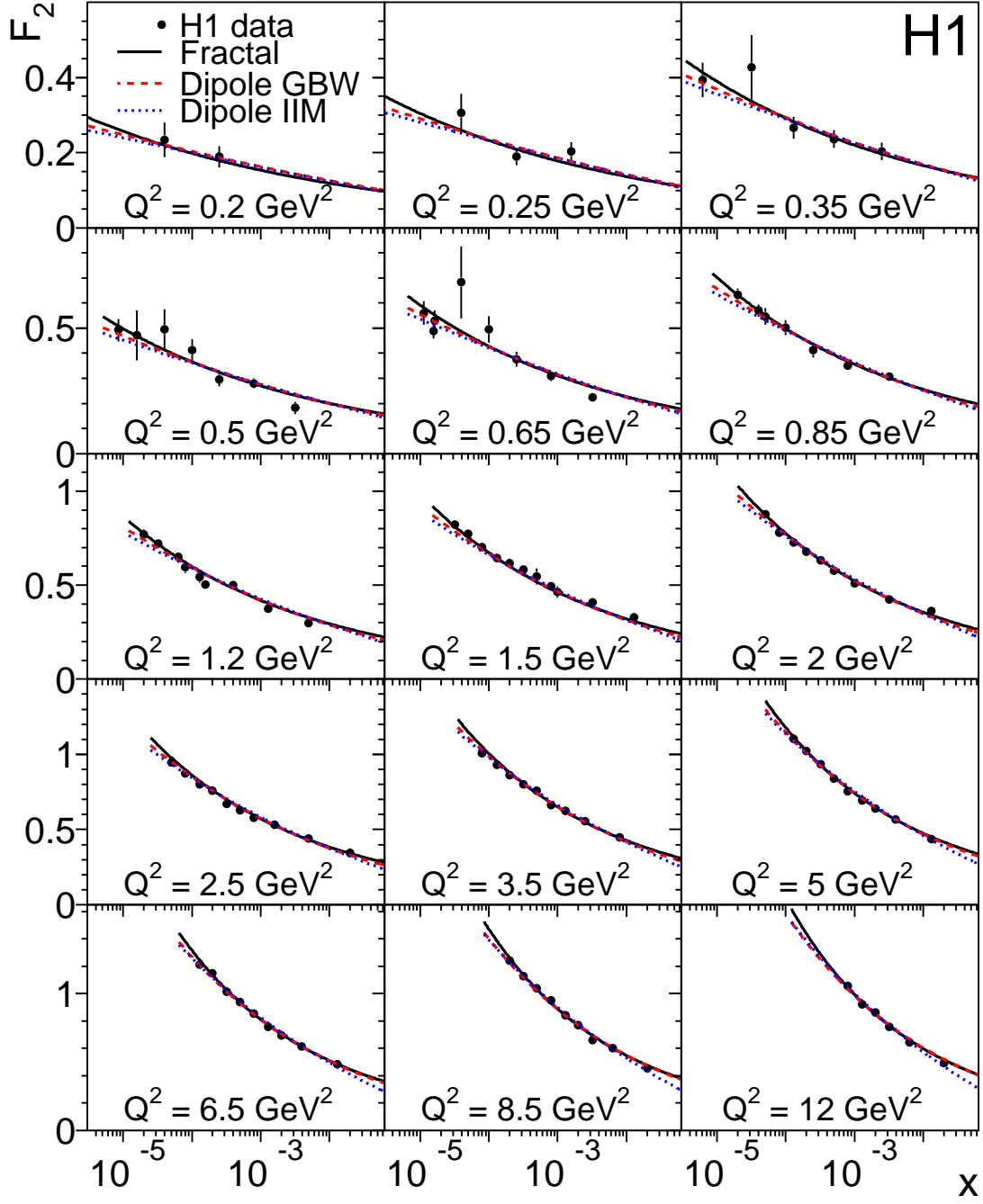


Figure 31: Structure function F_2 , from the combined low Q^2 H1 data for $y < 0.6$, as a function of x compared to the fractal, the dipole GBW and the dipole IIM fit results. The errors represent the statistical and systematic uncertainties added in quadrature.

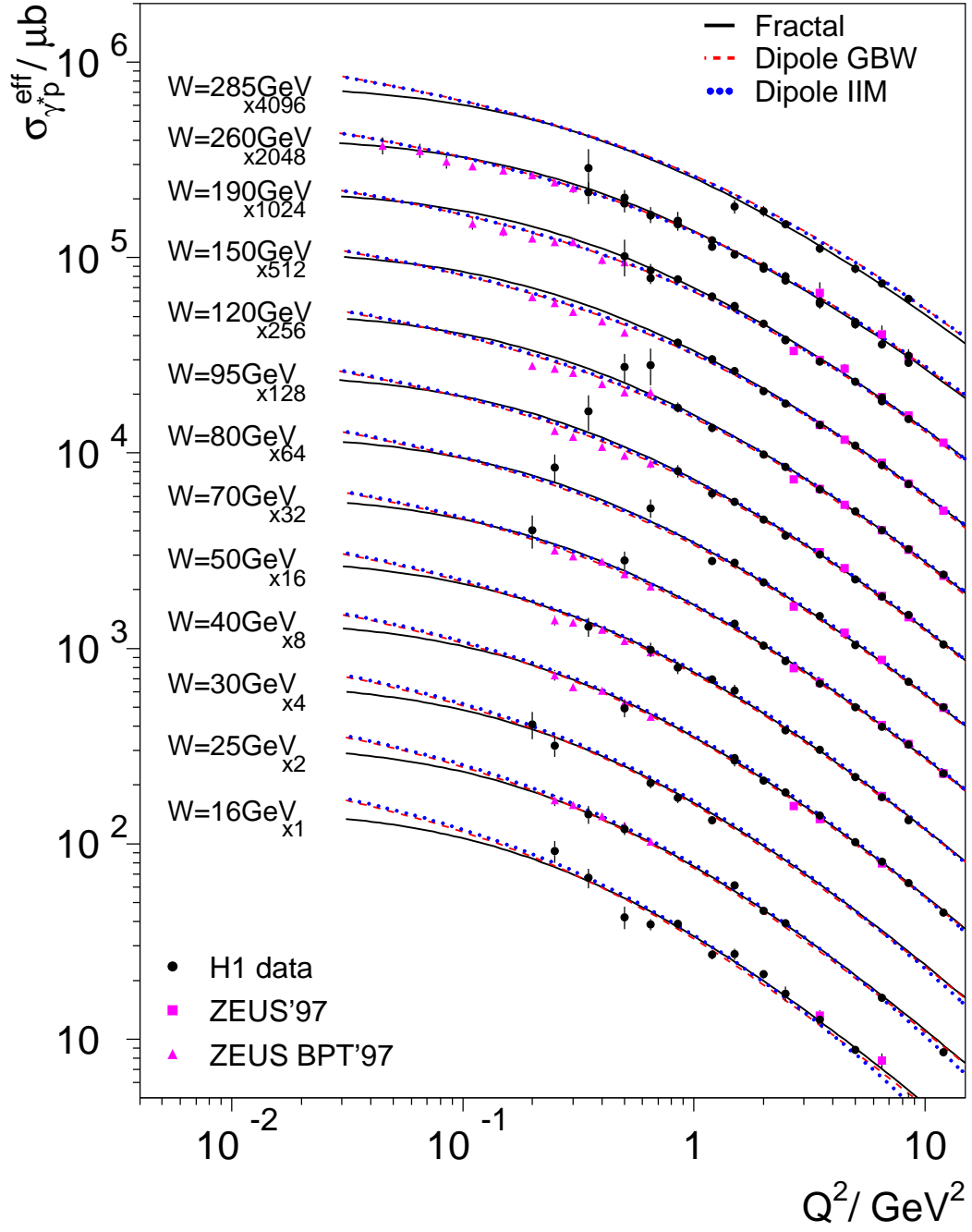


Figure 32: Measurement of the virtual photon-proton cross section $\sigma_{\gamma^*p}^{\text{eff}}$ as a function of Q^2 at various values of W . The cross sections for different W values are multiplied with the factors indicated in the figure. The errors represent the statistical and systematic errors added in quadrature. The averaged H1 results are compared to data obtained by the ZEUS experiment and to the fractal and dipole model fit results.

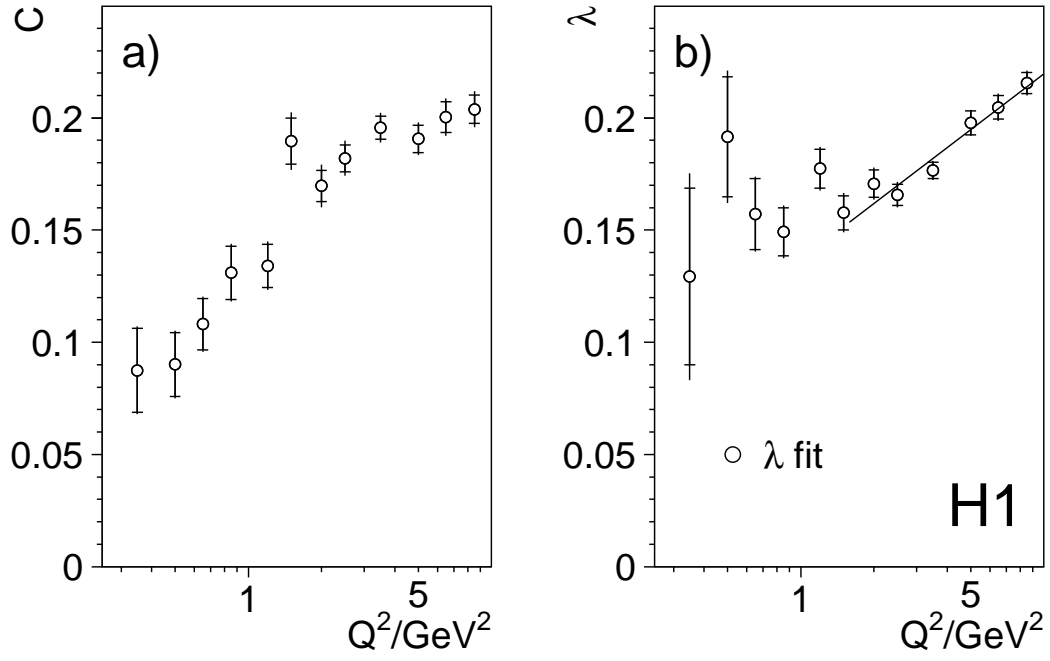


Figure 33: Coefficients c and λ , as defined in equation 34, determined from a fit to the H1 data as a function of Q^2 . The inner error bars represent uncorrelated systematic uncertainties. The outer error bars represent total uncertainties. The line in b) shows a straight line fit for $Q^2 \geq 2 \text{ GeV}^2$.

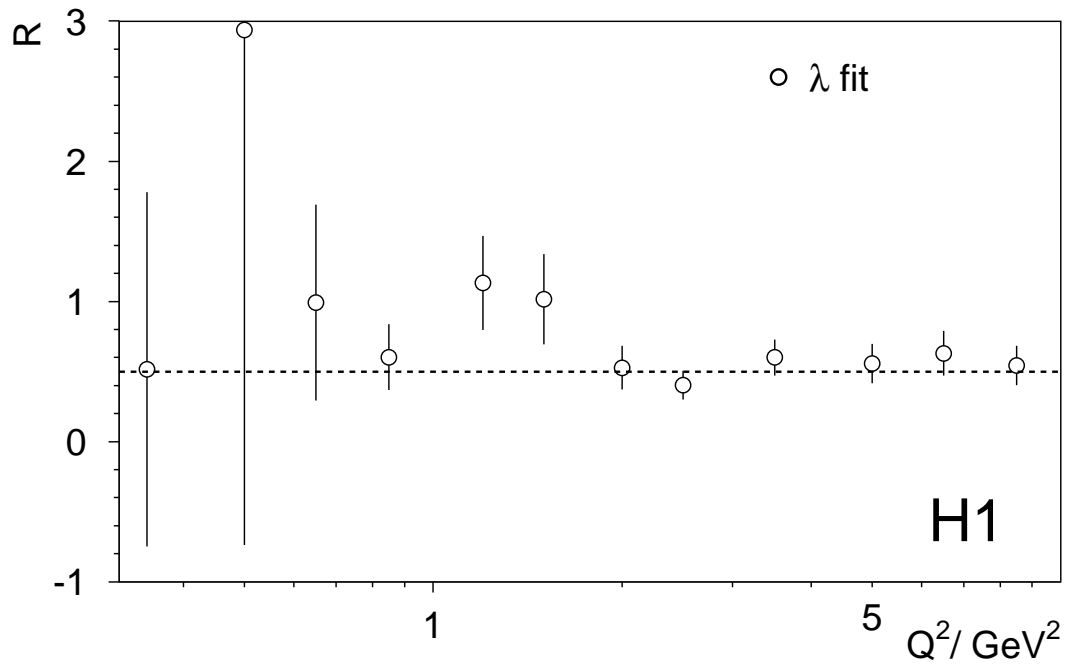


Figure 34: Coefficient R as a function of Q^2 from a simple parameterisation of the reduced cross section as defined in equation 34. The dashed line is drawn at $R = 0.5$. The errors represent the total uncertainties.

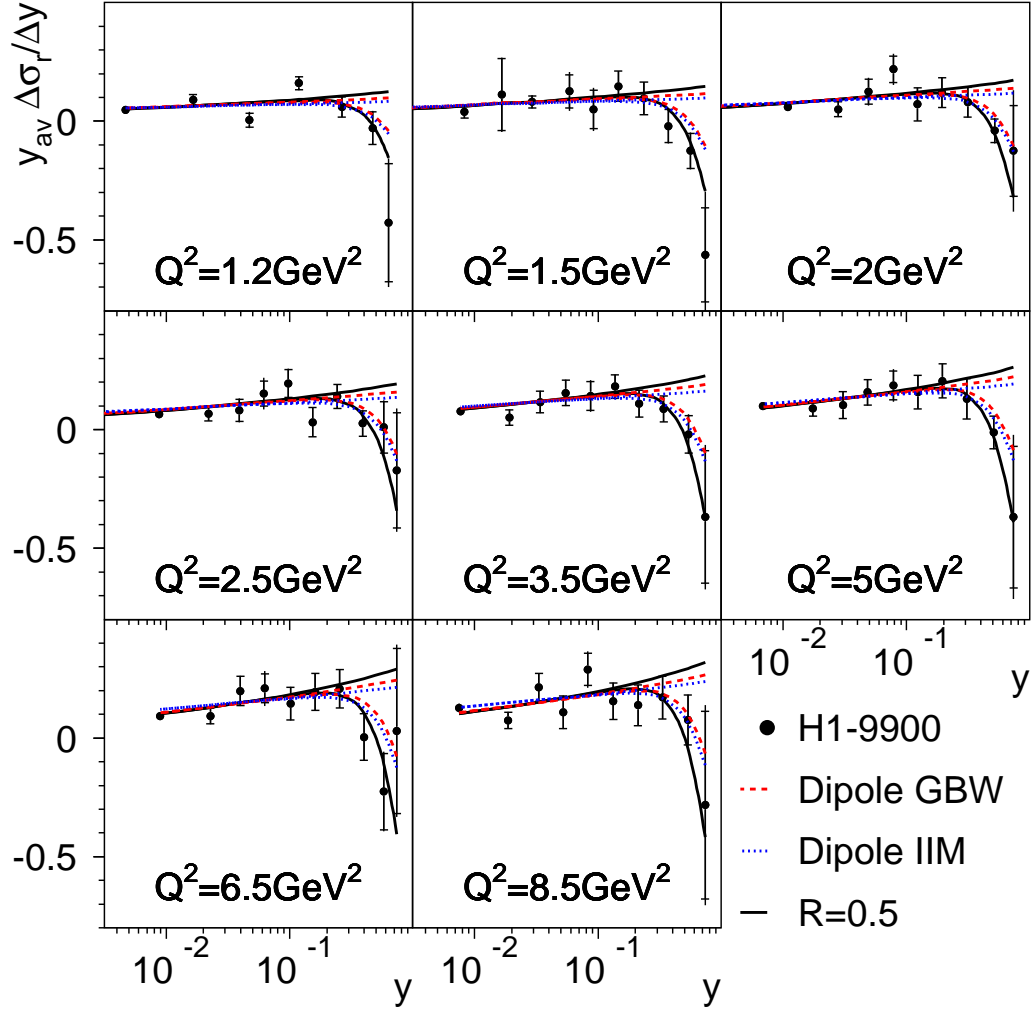


Figure 35: Derivative $y_{av} \Delta\sigma_r / \Delta y$ for the combined 1999-2000 H1 data compared to the predictions of the dipole models and the fractal model for F_2 with an assumption $R = 0.5$ to describe F_L , labeled $R = 0.5$. The lines increasing as a function of $\ln y$ correspond to $F_L = 0$ for these models. The lines turning over at high y correspond to the cross section predictions. The inner error bars represent statistical and uncorrelated uncertainties added in quadrature, the outer error bars represent the total uncertainties.

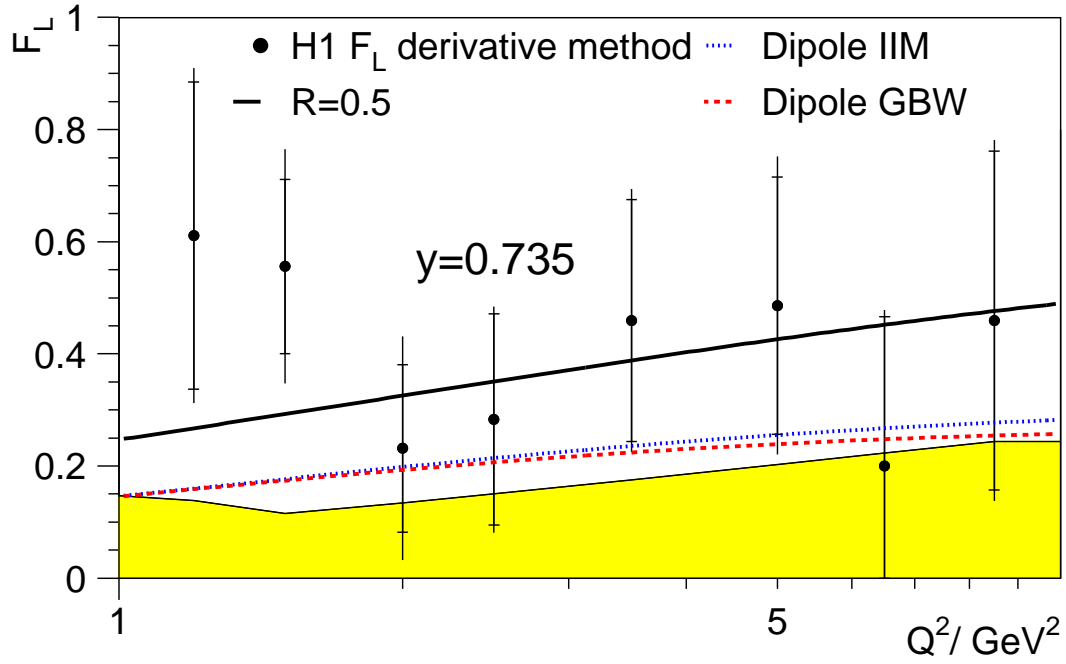


Figure 36: Structure function F_L extracted using the derivative method. The solid line is drawn for $R = 0.5$ assuming the fractal parameterisation for F_2 . The dashed (dotted) line corresponds to the dipole GBW (IIM) model. The inner error bars represent statistical and uncorrelated uncertainties added in quadrature, the outer error bars represent the total uncertainties. The solid (yellow) band indicates the model uncertainty, see text.

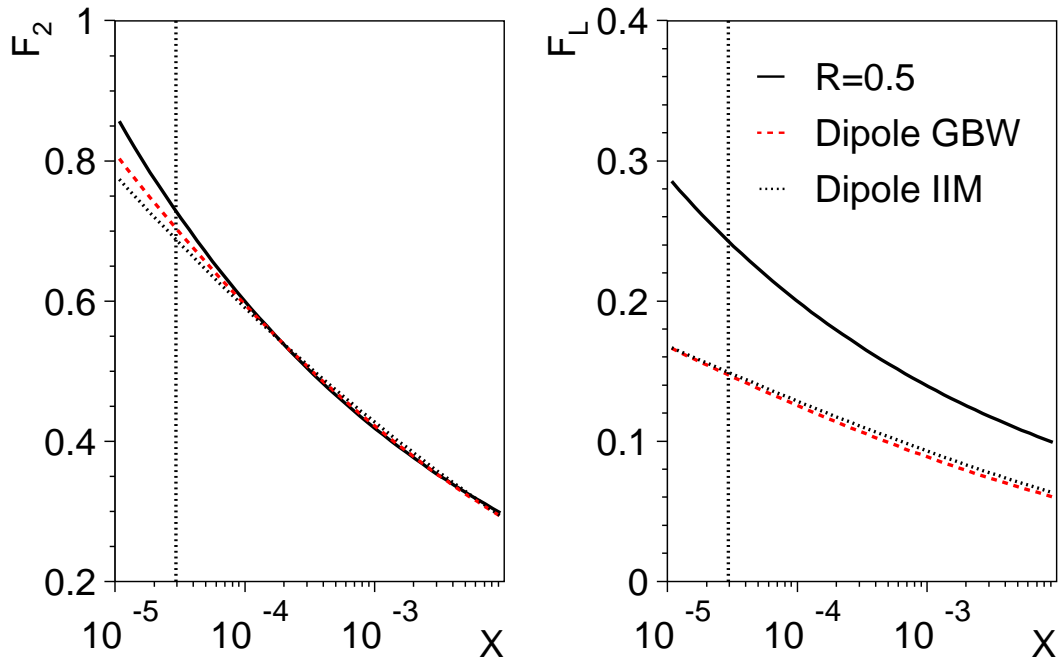


Figure 37: Comparison of the structure functions F_2 (left) and F_L (right) for $Q^2 = 1.2 \text{ GeV}^2$ as a function of Bjorken x , for the fractal fit with $R = 0.5$ (solid line), and the predictions of the dipole models, GBW (dashed line) and IIM (dotted line), resulting from the fits to the H1 cross section data. The vertical line indicates the value of $x = x_s$ for which the GBW dipole model saturation radius is reached.